Modelling of Gradients in Large Scale Bioreactors

Bach, Christian

Publication date:
2018

Document Version
Publisher's PDF, also known as Version of record

Modelling of gradients in large scale bioreactors

Christian Bach

PhD Thesis

April 2018

DTU Chemical Engineering
Department of Chemical and Biochemical Engineering

MODELLING OF GRADIENTS IN LARGE SCALE BIOREACTORS

Christian Bach

PhD Thesis

April 2018

DTU Chemical Engineering
Department of Chemical and Biochemical Engineering

Address: Process and Systems Engineering Center (PROSYS)

Department of Chemical and Biochemical Engineering

Technical University of Denmark

Building 229

Dk-2800 Kgs. Lyngby

Denmark

Phone: +45 4525 2800

Web: www.kt.dtu.dk/forskning/prosys

Print: STEP

DTU Chemical Engineering
Department of Chemical and Biochemical Engineering

Abstract

The heart of biotechnology and the bio-based economy is microbial conversion of substrates to desired products in fermentation processes. The physiological machinery within the microorganism is able to synthesise a range of valuable molecules spanning the product portfolio from bulk chemicals, such as alcohols and organic acids to fine chemicals, such as vitamins and finally to complex molecules such as industrial enzymes and monoclonal antibodies. Common for the processes developed to produce the desired products is the need for large production tanks that compensate for the low productivity of fermentation processes compared to conventional chemical processes. The scale of the production tanks is generally in the range of ten cubic meters to several hundred cubic meters.

Maintaining optimal production conditions in these large vessels is often achieved by a configuration of several agitators inside the vessel. The agitation is not only responsible for maintaining homogeneous conditions inside the production vessels but also for providing a sufficient distribution of air in aerobic fermentation processes. In order to understand the performance and troubleshoot problems of the large-scale fermenters fundamental understanding of the mixing and mass transfer capabilities of these reactors is required. Computational fluid dynamics and spatial measurements of process variables are the most common theoretical and empirical ways to investigate the process gradients in large-scale fermenters resulting from insufficient homogenisation. The improvement of computational capabilities over the past few years has enabled simulations of these complex phenomena at full scale, but the modelling choices and assumptions required are yet to be thoroughly analysed.

In this thesis, the role of mixing and mass transfer in relation to performance of large scale fermentation processes is outlined. The application of computational fluid dynamics in industrial fermentation processes is described at pilot and full scale for a *Trichoderma reesei* fermentation. A key input parameter in the numerical simulation of the aerobic fermentations is the size of air bubbles, which has been investigated at pilot scale using an endoscopic method. The oxygen concentration gradients of three impeller configurations of a full-scale fermenter have been characterised and compared with experimental data. Finally, a methodology for simplifying the complex mathematical models resulting from applying the finite element method to compartment models is described and applied to a pilot scale fermenter. The reduction of the model complexity enables a broader application

of mathematical models for process optimization and control, but also introduces the possibility of including the understanding of hydrodynamics in process research and development at an early stage.

Resumé

I hjertet af industriel bioteknologi og en økonomi baseret på biologiske produkter sidder mikroorganismer, som omdanner råvarer til ønskede produkter i fermenteringsprocesser. Fysiologien af mikroorganismerne gør dem i stand til at skabe en række af værdifulde molekyler, som spænder over en bred vifte af produkter fra bulk kemikalier som alkoholer og organiske syrer til vitaminer, og endda komplekse molekyler som industrielle enzymer og antistoffer. Alle disse processer har det til fælles, at de er afhængige af at foregå i store produktionstanke, der kan kompensere for den lave produktivitet i fermenteringsprocessor i forhold til konventionelle kemiske processer. Disse produktionstanke er generelt i størrelsesordenen fra ti kubikmeter til flere hunderede kubikmeter

For at sikre optimale procesbetingelser i de store produktionstanke er der ofte installeret op til flere omrører i tanken. Omrøringen er ikke kun ansvarlig for sikring af homogene betingelser i tanken, men også for at sikre det nødvendige fordeling af luft under de aerobe fermenteringsprocesser. Fundamental forståelse af opblanding og massetransport er nødvendig, hvis ydeevnen af fermentering på så stor skala skal forbedres og hvis årsagen til problemer skal identificeres. Computational Fluid Dynamics (CFD) og målinger forskellige steder i produktionstankene er de mest benyttede metoder til at undersøge gradienter i procesbetingelser, der opstår ved utilstrækkelig opblanding i fermenterer på stor skala. Forøgelsen af regnekraft over det seneste årti har muliggjort simulering af disse komplekse fænomener i industriel skala, men der er endnu ikke tydeligt redegjort for hvordan modelantagelser påvirker resultaterne.

I denne afhandling er effekten af opblanding og massetransport i forhold til ydeevnen af stor skala fermenterer undersøgt. CFD har været benyttet til at beskrive opblanding og massetransport i en industriel fermentering af *Trichoderma reesei* på både pilot og fuld skala. En nøgleparameter i numeriske simuleringer af aerobe fermenteringsprocesser er størrelsen af luftbobler, hvilket er blevet karakteriseret ved brug af et endoskop på pilot skala. Iltkoncentrationerne ved tre forskellige omrører konfigurationer under en fuld skala *Trichoderma reesei* fermentering er endvidere undersøgt og sammenlignet med eksperimentelle data. En procedure til simplificering af de numeriske simuleringer med CFD modellerne til et mindre antal kontrol voluminer er ligeledes beskrevet og anvendt på en pilot skala fermenter. Reduktionen af modelkompleksitet gør det muligt at benytte matematiske modeller til proceskontrol og optimering, men introducerer også muligheden for at benytte viden om hydrodynamikken som en del af forskning og procesudvikling.

Preface

This thesis was written at the Process and Systems Engineering Center (PROSYS), Department of Chemical and Biochemical Engineering, Technical University of Denmark (DTU). The work was carried out in the period from March 2015 to April 2018 under the supervision of Professor Krist V. Gernaey and Associate Professor Ulrich Krühne, both from the Technical University of Denmark, and Research Scientist Mads O. Kaiser-Albæk, Novozymes A/S. The study received funding from Novozymes A/S, the strategic research centre BIOPRO and the Department of Chemical and Biochemical Engineering at the Technical University of Denmark.

My deepest gratitude goes to my supervisors who have constantly challenged and encouraged the progress of this project. I would like to thank Krist, for his ability to create a work environment where creativity can thrive and no idea is too big to discuss. I owe thanks to Ulrich Krühne for his positive attitude and relentless believe in the benefits of CFD simulations in all aspects of chemical engineering. Lastly, I would like to thank Mads for his invaluable process insights throughout the project as well as his ability to keep the research on track and industrially relevant. Additionally, I would like to thank Sjef Cornelissen for his guidance and academic sparring during the project. I would also like to acknowledge the help of the workshop at the Technical University of Denmark and the operators and lab technicians at the fermentation pilot plan at Novozymes A/S for assisting with experimental implementation. Special thanks go to Professor Farhad Ein-Mozaffari at Ryerson University in Toronto for allowing me to test ideas in his laboratory, and for making me feel welcome and appreciated. And, I would like to thank Argang Kazemzadeh for fruitful academic discussions during my research stay in Toronto.

Thank you to all my colleagues that I have directly collaborated with during the past three years (Anders, Lisa, Daniela, Jifeng, Rayisa, Andreas, Gisela, Tannaz and Mafalda) it has been a great pleasure. I have appreciated the social companionship of our lunch club and its members over the past three years (Mafalda, Søren, Rolf, Leander, Ricardo, Franz, Morten and Asbjørn), thank you all.

Finally, I would like to thank my family and especially my wife, Xandra, for the relentless support and encouragement during this project.

Kgs. Lyngby 12th of April 2018

Christian Bach

Contents

Chapter 1

Introduction

1.1 Background

The list of products produced industrially from fermentation processes is vast and diverse, covering small molecules such as alcohols and organic acids to large complex molecules such as industrial enzymes and insulin [1]. Additionally certain processes are geared towards the production of cellular biomass, which is the case for lactic acid bacteria and single cell protein [2]. The products derived from fermentation processes play a key role in many industrial sectors and economic markets from bulk chemicals and commodities to polymers and complex fine chemicals. This diversification is even more pronounced if processes and products that are made up partly or fully by compounds derived from fermentation processes are included in the list. A few examples worth mentioning in this context are butane-diol produced as a building block for plastics, recombinant therapeutic proteins as active pharmaceutical ingredient in medicine and industrial enzymes used as catalysts in a range of industries from household care to food and second generation ethanol among others [3–5]. These few examples support the statement that industrial fermentation processes and products derived from them play a key role in the global economy, and this role is projected to grow with the further development of biorefineries [6,7].

1.1.1 The development from discovery to production

At the center of all industrial fermentation processes sits the microbial host that is responsible for the desired conversion of substrate to product. The efficiency and productivity of the microorganisms have improved through strain development and optimization where high throughput screening methods assist in determining the optimal conditions for the microorganisms [8]. The operational optimum is generally very specific and determines the optimal temperature, pH, carbon source, nitrogen source and possibly also requirements for oxygen transfer and carbon dioxide removal. Automated parallel

single-use bioreactors, such as the AmbR 15™ and Ambr 250™ from Sartorius AG, are a common platform for the screening of optimal conditions for the fermentation process. The parallel platform combined with design of experimental methods enables a fast and thorough development phase of new fermentation processes. With the operational optimum identified the process is moved to pilot scale testing, where a thorough operational procedure is developed. This step in the development identifies the specific operational configuration in terms of feeding profiles of carbon source, process set-points and control strategies. The expected productivity and process yield is confirmed in pilot scale and compared with the results from the screening to ensure that the process metrics are met. After successful pilot testing, the process is introduced to the production facility, which concludes the testing and iterative phase of the process development and where focus is moved towards risk mitigation and quality control. Common for all steps in the development process is a substantial increase in fermenter volume, from 15- 250 mL in the screening phase to hundreds of liters in the pilot phase and finally potentially hundreds of cubic meters in the production facility. The increase in scale is inversely proportional to the number of tests that are conducted and the number of potential failures accepted for each step in the process. The challenges arise when the optimal operating conditions identified in the experimental screening cannot be maintained in the large production facility because of certain process phenomena being sensitive to the size of the equipment. A classic example of such phenomena is convectional transport of components in the liquid phase of fermenters, which generally is neglected in small and pilot scale, but in production scale it plays a substantial role [9]. The efficacy of the convectional flow of liquid, also referred to as liquid mixing, is dependent on the width of the fermentation vessel to the power of 2/3 [10]. This means that the liquid mixing is dependent on the volume of the fermentation vessel to the power of 2/9, which at first glance is a relative weak dependency, but the increase in fermentation volume during the scale-up of production processes from 250 mL to 100 m^3 makes it significant. Following this relationship, a geometrically identical fermenter at production scale will encounter a mixing efficacy that is approximately 18 times worse than at the screening stage. This decrease in mixing efficacy during scale-up makes it difficult to ensure optimal process conditions in the fermentation vessel at production scale.

Understanding the liquid convection at production scale is essential in order to avoid problems during scale-up, but detailed understanding of the hydrodynamics at this scale is not well understood. Mathematical modeling can be a useful tool in order to realize this fundamental understanding by comparing a hypothesis with experimental findings [11]. In this thesis, Computational fluid dynamics

is assessed as a tool to facilitate reaching a more fundamental understanding of the hydrodynamics in aerated fermentation vessels at pilot and large scale.

1.2 Scope

The overall research objective of this project has been to address the challenges of modeling the process gradients in large scale bioreactors using computational fluid dynamics. The research focus has been on addressing the challenges in modeling industrial fermentation processes and test whether the models are applicable to these systems. A large part of this thesis has been focused on investigating the mixing and mass transfer in a *Trichoderma reesei* fermentation process as a case study. The applicability of CFD for industrial fermentations was illustrated at pilot scale, where the bubble size of the gas phase was identified as a crucial parameter. This finding lead to an empirical investigation of the bubble size distributions in these processes. The lessons learned from these findings were applied to an industrial scale investigation of a *Trichoderma reesei* fermentation process. Finally, methods for simplifying the complex mathematical models of the hydrodynamics were developed and tested at pilot scale.

1.3 Thesis structure

The general structure of the thesis is presented below as a brief overview:

Chapter 1 serves as an introduction to industrial fermentation and the challenges of scale-up. Furthermore, the chapter introduces the scope of the thesis.

Chapter 2 illustrates the role of mixing and mass transfer in industrial scale fermentation vessels, and how mathematical models are an essential tool in understanding the hydrodynamics.

Chapter 3 describes an application of computational fluid dynamics to a *Trichoderma reesei* fermentation at pilot scale. The mixing and mass transfer capabilities has been simulated and compared with empirical data.

Chapter 4 highlights the use of a custom-made equipment able to determine the bubble size distribution in industrial pilot scale aerated fermenters. The technology is applied to the *Trichoderma reesei* process investigated in Chapter 3.

Chapter 5 illustrates the prediction of oxygen gradients using computational fluid dynamics in an industrial scale *Trichoderma reesei* fermentation. The predictions are compared with measured values from the industrial process.

Chapter 6 describes a hypothesis driven method of downscaling the numerical simulations based on computation fluid dynamics. The method was applied to an industrial pilot scale fermenter.

Chapter 7 provides the major conclusions of the thesis and suggests perspectives for future work.

Each chapter documenting the research work performed (i.e. chapters 2-6) serves as an individual research piece with description of nomenclature, a discussion and conclusion. The thesis should therefore be seen as a collection of research manuscripts and not a monograph.

1.4 References

[1] M.J. Waites, N.L. Morgan, J.S. Rockey, G. Higton, Industrial Microbiology : An Introduction, John Wiley & Sons, Incorporated, Hoboken, UNITED KINGDOM, 1999. http://ebookcentral.proquest.com/lib/dtudk/detail.action?docID=428028.

[2] J.G. Zeikus, Chemical and fuel production by anaerobic bacteria, Annu. Rev. Microbiol. 34 (1980) 423–464. doi:10.1146/annurev.mi.34.100180.002231.

[3] H. Yim, R. Haselbeck, W. Niu, C. Pujol-Baxley, A. Burgard, J. Boldt, J. Khandurina, J.D. Trawick, R.E. Osterhout, R. Stephen, J. Estadilla, S. Teisan, H.B. Schreyer, S. Andrae, T.H. Yang, S.Y. Lee, M.J. Burk, S. Van Dien, Metabolic engineering of Escherichia coli for direct production of 1,4-butanediol, Nat. Chem. Biol. 7 (2011) 445–452. doi:10.1038/nchembio.580.

[4] C.-J. Huang, H. Lin, X. Yang, Industrial production of recombinant therapeutics in Escherichia coli and its recent advancements, J. Ind. Microbiol. Biotechnol. 39 (2012) 383–399. doi:10.1007/s10295-011-1082-9.

[5] S.M. Stocks, Industrial enzyme production for the food and beverage industries : process scale up and scale down, in: Microb. Prod. Food Ingredients, Enzym. Nutraceuticals, 2013: p. 656. doi:10.1533/9780857093547.1.144.

[6] B.E. Dale, S. Kim, Biomass Refining Global Impact–The Biobased Economy of the 21st Century, in: Biorefineries-Industrial Process. Prod., Wiley-VCH Verlag GmbH, Weinheim, Germany, n.d.: pp. 41–66. doi:10.1002/9783527619849.ch2.

[7] A.J.J. Straathof, Transformation of biomass into commodity chemicals using enzymes or cells, Chem. Rev. 114 (2014) 1871–1908. doi:10.1021/cr400309c.

[8] J. Villadsen, J. Nielsen, G. Lidén, Bioreaction Engineering Principles, 3rd ed., Springer, 2011.

doi:10.1007/978-1-4419-9688-6.

[9] A.P.J. Sweere, K.C.A.M. Luyben, N.W.F. Kossen, Regime analysis and scale-down: Tools to investigate the performance of bioreactors, Enzyme Microb. Technol. 9 (1987) 386–398. doi:10.1016/0141-0229(87)90133-5.

[10] A.W. Nienow, Hydrodynamics of Stirred Bioreactors, Appl. Mech. Rev. 51 (1998) 3. doi:10.1115/1.3098990.

[11] K. Sanford, G. Chotani, N. Danielson, J.A. Zahn, Scaling up of renewable chemicals, Curr. Opin. Biotechnol. 38 (2016) 112–122. doi:10.1016/J.COPBIO.2016.01.008.

Chapter 2

The influence of mixing and mass transfer in aerated bioreactors

In this chapter, the effect of hydrodynamics and mixing in fermentation processes at industrial scale is highlighted and certain counter intuitive dynamics are explained in case studies.

2.1 Abstract

The majority of biobased-derived products are fully or partially dependent on fermentation processes that can convert a given substrate to the target product. Fermentation processes are either aerobic or anaerobic referring to the requirement of oxygen as part of the conversion of substrate. Industrial aerobic fermentation processes, which is the focus of this work, occur on a massive scale with two dominant vessel configurations the stirred tank and the bubble column. Optimal process conditions can be difficult to maintain at this scale and in particular carbon source feeding in fed-batch fermentations is challenging, which is highly dependent on the mixing characteristic of the fermenter at scale. Mathematical models can assist in understanding the relationship between liquid mixing and process performance, and highlight some of the counter intuitive dynamics occurring in large scale fermenters. This is illustrated in two case studies where the effect of oxygen concentration controlled substrate feeding on glucose gradients is investigated for a 100 m^3 stirred tank fermenter and a bubble column. Simple correlations of the hydrodynamics enables insight into why the process gradients increase when the agitation intensity is increased during oxygen controlled substrate feeding. The case studies highlight the importance of mathematical modelling in the context of large scale fermentation processes, but also illustrates the need for more advance hydrodynamics models such as Computational Fluid Dynamic methods.

2.2 Nomenclature

Roman	Description	Unit
C_{O_2}	Dissolved oxygen concentration	[g/L]
$C^*_{O_2}$	Dissolved oxygen concentration at saturation	[g/L]
C_S	Concentration of carbon source	[g/L]
$C_{gluc,i}$	Concentration of glucose in compartment i in the stirred tank	[g/L]
$C_{gluc,feed}$	Glucose concentration in feed zone	[g/L]
D	Impeller diameter	[m]
F	Feed flow rate	[g/h]
F_l	Impeller flow number	[-]
g	Gravity constant	[m/s^2]
H	Tank height	[m]
$\frac{H}{T}$	Tank aspect ratio	[-]
K	Constant in k_La correlation	[h^{-1}]
K_S	Half saturation concentration of limiting substrate	[g/L]
K_H	Henry's constant for oxygen	[g/L/bar]
k_La	Volumetric mass transfer coefficient	[h^{-1}]
l_{BC}	Circulation loop length in bubble column	[m]
N	Impeller rotational speed	[min^{-1}]
N_i	Number of impellers	[#]
OTR	Oxygen transfer rate	[g/L/h]
OUR	Oxygen uptake rate	[g/L/h]
P	Pressure	[bar]
P_o	Impeller power number	[-]
$\frac{P}{V}$	Power input per volume	[kW/m^3]
Q	Volumetric flow rate discharged by the impeller	[L/h]
V	Tank volume	[m^3]
VVM	Volumetric air flowrate per tank volume	[m^3/m^3/min]
v	Liquid velocity vector	[m/s]
v_L	Liquid circulation velocity	[m/s]

v_S	Superficial gas velocity	[m/s]
v_x	Velocity in x direction	[m/s]
v_y	Velocity in y direction	[m/s]
v_z	Velocity in z direction	[m/s]
X	Biomass concentration	[g/L]
Y_{sx}	Yield of biomass on substrate	[g/g]
Y_{xo}	Yield of oxygen on biomass	[g/g]
y_{O_2}	Mole fraction of oxygen in gas phase	[-]

Greek	**Description**	**Unit**
α	Exponent in $k_L a$ correlation	[-]
β	Exponent in $k_L a$ correlation	[-]
μ	Microbial growth rate	[h^{-1}]
μ_{max}	Maximum microbial growth rate	[h^{-1}]
τ_{BC}	Residence time of the substrate in bubble column	[s]
τ_{mix}	Mixing time	[s]
τ_{res}	Residence time in recirculation loop in stirred tank	[s]

2.3 Introduction

Fermentation processes can be divided into two fundamental categories: aerobic and anaerobic processes, indicating the need for oxygen in order to perform the bioconversion at the desired rate. Whether a process is aerobic or anaerobic depends on the desired product, the productivity and the microbial host used to facilitate the bioconversion. The oxygen demand in a microorganism comes from respiration in the cell, which allows for full oxidation of the carbon source to carbon dioxide. Complete oxidation of one glucose molecule in for instance *S. cerevisiae* results in a total production of 12 ATP molecules to be used as energy for growth of cells, maintenance and product formation [1]. This amount of energy produced per glucose molecule under aerobic conditions is in sharp contrast with anaerobic catabolism, which only yields two ATP molecules per glucose molecule [2]. Anaerobic catabolism is unable to oxidise the produced NADH from the glycolysis, which limits the energy utilization of glucose. Ethanol or lactate ends up as the cellular product of the anaerobic catabolism due to the shortage of oxidation potential.

Anaerobic processes can theoretically utilize the carbon source more efficiently and result in process yields close to the fundamental limit if the product is a metabolite in glycolysis. A classic example of an industrial anaerobic fermentation is the conversion of glucose to ethanol. Ethanol production is carried out on a massive scale from sugar cane particularly in Brazil without the need of oxygen as co-substrate. The ethanol produced by fermentations accounts for 80 % of the total production of ethanol in the world [3]. Another anaerobic process that is frequently mentioned is the lactic acid bacteria fermentation, which is used in the food and ingredient industry in particular as starter cultures for fermented foods [4].

Aerobic fermentation processes require the presence of oxygen because of the energy needed to perform a conversion of the given substrate to the desired product. The need of additional ATP arises mainly from the metabolic pathway used for the synthesis of the product or biomass. The availability of oxygen is crucial for successful operation of aerobic processes, and is also challenging because of the low solubility of oxygen in water. Production of industrial enzymes is mainly carried out aerobically because the energy requirement in producing large amounts of amino acids at high productivity makes it unfeasible to produce the enzymes anaerobically. The possibility of producing enzymes anaerobically has been suggested in the 80's, but has not been realized to this day [5]. Aerobic fermentation processes are carried out on an industrial scale in fermentation vessels that vary considerably in size, all depending on the product formed in the process. In Table 2.1, a partial list of known industrial scale aerobic fermentation vessels is shown.

Table 2.1 - List of industrial aerobic fermentation vessels above 180 m^3 [6]

Company	Location	Reactor type	Volume [m^3]
Fermic	Mexico	Stirred tank	190
Novozymes	Canada	Bubble column	220
Tate & Lyle	USA	Bubble column	227
ADM	USA	Stirred tank	500
Cargill	USA	Bubble column	500
Nutrasweet	Brazil	Bubble column	520
Dupont-Tate & Lyle	USA	Bubble column	600
Solazyme	Brazil	Stirred tank	600
Evonik	Brazil	Stirred tank	700
Jungbunzlauer	Canada	Bubble column	750
ADM	USA	Bubble column	1000

Table 2.1 illustrates the typical size range of industrial aerobic fermentations vessels, and the two common types of reactors utilized. The scale of the industrial production vessels gives rise to challenges in controlling the process and maintaining the optimal conditions to perform the bioconversion of interest. The addition of nutrients to the fermenter becomes particularly challenging at these production volumes. Besides the need for oxygen, anaerobic and aerobic fermentations have similar characteristics, e.g., the need for a source of carbon, nitrogen and other nutrients. These nutrients are usually either fed to the fermenter during the process or available in the beginning of the process, or a combination of both. The addition of nutrients depends on the operational mode of the fermentation process, whether it is batch, fed-batch or continuous. The operational mode of industrial fermentation processes is generally continuous or fed-batch because of the increased productivity compared to standard batch operation. The choice between fed-batch or continuous process is dependent on the productivity requirements and the expression systems employed to facilitate the bioconversion. A stable host without risk of mutating or losing its plasmid(s) is necessary to leverage the increased productivity of a continuous process [7]. Such guarantees can be difficult to provide for a highly mutated organism which is why the common practice for industrial fermentations, where the cost is not only associated with carbon yield, is to operate the process as a fed-batch fermentation. Fed-batch fermentations rely on a continuous feeding of carbon source throughout the process, which results in an increasing liquid volume inside the fermenter as illustrated in Figure 2.1.

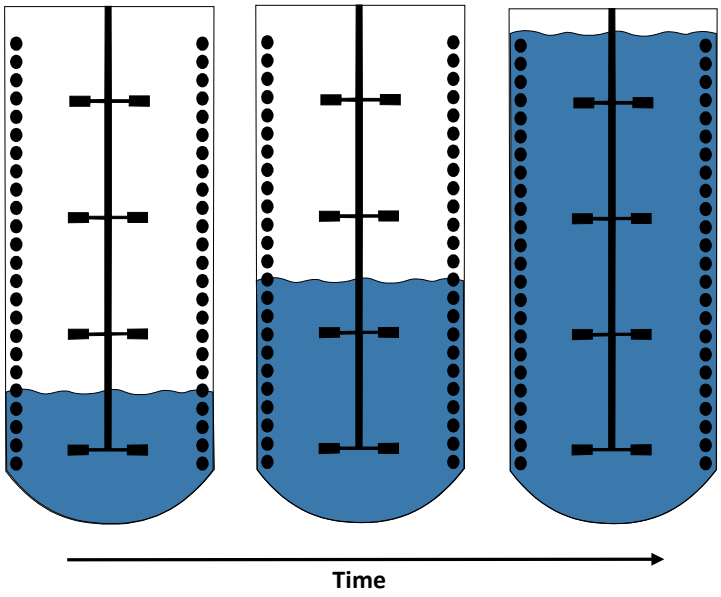

Figure 2.1 - Schematic illustration of a fed batch fermentation process from start fill to harvest.

The prolonged fermentation process caused by the continuous feeding in a fed-batch enables an optimal use of the formed biomass in the initial batch phase. In particular for industrial enzyme secretion and other processes where product formation is induced as a starvation response, fed-batch operation is ideal [2,8]. The depletion of the carbon source in the initial batch phase induces the secretion of enzymes and with meticulous carbon source addition, this can be continued throughout the course of the fed-batch thus yielding high product titer and avoiding substrate inhibition related phenomena.

2.4 The effect of mixing on fermentation performance

Industrial fed-batch processes rely upon constant addition of nutrients that need to be available for the microorganism to allow uptake and utilization. The availability of nutrients in large bioreactors, in the order of 100 m^3 in production volume, depends on the convectional motion of the liquid in the fermentation vessel. The convectional motion inside the reactor vessel is caused by physical motion of an impeller for a stirred tank reactor or by buoyancy differences between gas and liquid phase in bubble columns. Depending on the efficacy of these phenomena, the nutrients and gas phase inside

the fermenter will be dispersed homogeneously or heterogeneously. In this context, the fermentation performance is defined as the carbon and oxygen utilization by the microorganism in homogeneous conditions.

2.4.1 Gradients in carbon source in large scale fermenters

The hypothesis of insufficient mixing in bioreactors has been the research topic for numerous researchers over the last three decades [9–14]. Classic examples of the effect of insufficient mixing on aerobic fermentation are the Crabtree and Pasteur effects in yeast [15]. The Crabtree effect is a sensitivity to high glucose concentration in the yeast, which causes a production of ethanol in order to maintain a suitable ATP concentration in the cell under aerobic conditions. Under oxygen-depleted conditions, the yeast produces ethanol to scavenge energy to be used in anabolic reactions in the cell. These phenomena and other ones that are closely related (e.g. acetate production in *E. coli* due to the presence of excess glucose in the media) can be triggered by insufficient convectional flow in large scale fermenters.

The inhomogeneity of glucose concentrations in a large scale fermenter has been reported for a 22 m^3 fermentation process utilizing *S. cerevisiae* [11]. Glucose levels in the reactor were measured using several sampling ports during glucose addition to either the top or bottom of the reactor. The reported differences in glucose concentrations when comparing the feeding point to the bottom of the vessels were between 4 mg/L and 40 mg/L. Another example of glucose gradients in large scale bioreactors was reported for a 215 m^3 bubble column cultivating baker's yeast [16]. The industrial bubble column was equipped with two sample ports at different levels of the reactor, which enables an assessment of the axial glucose gradients during the fermentation. Molasses was used as carbon source for the fermentation, and was fed one meter above the bottom of the bioreactor. The resulting fructose concentration was 115 mg/L at 2.1 meters above the bottom and 150 mg/L at 6.3 meters above the bottom during the fermentation. The fructose gradient increases during the fed-batch fermentation indicating that the gradient could be caused by insufficient convectional flow for increased filling of the fermenter. A 7 % reduction in biomass yield was observed when comparing the production scale fermentation and a small well-mixed stirred tank operating under the same conditions and applying the same feeding profile. The adverse effect on biomass yield due to carbon source gradients is not limited to *S. cerevisiae*. A 12 m^3 fermentation process cultivating *E. coli* was reported to suffer a 20 % reduction in biomass yield compared with an identical bench scale fermentation [17]. Furthermore, the production of by-products was more severe at large scale, which was materialized in an accumulation of acetate during the process. Interestingly, the reduced biomass yield and increased by-

product formation due to the spatial heterogeneity of the carbon source did not affect product formation, which was indeed demonstrated not to be affected during scale up [17].

2.5 Oxygen gradients in large scale fermentation processes

The occurrence and understanding of oxygen gradients is more complex than carbon source and other nutrients because of the interdependency of gas and liquid phase behaviour. From first principles, the oxygen concentration in a given region of a bioreactor is a result of the equilibrium between liquid convection, oxygen transfer from the gas phase to the liquid phase and the oxygen uptake by the microorganisms. This can be represented mathematically as the following mass balance:

$$\frac{dC_{O_2}}{dt} = \nabla \cdot \boldsymbol{v}\, C_{O_2} + OTR - OUR \tag{2.1}$$

where C_{O_2} is the oxygen concentration in the liquid phase, $\nabla \cdot \boldsymbol{v}\, C_{O_2}$ is the convectional flow leaving and entering the region, OTR is the oxygen transfer rate from gas phase to liquid phase and OUR represents the microbial uptake rate of oxygen. The complexity of understanding the oxygen concentration behaviour in an aerated bioreactor can be explained because each of the three phenomena is dependent on multiple system states. The convectional flow, for example, is highly dependent on the energy dissipated by the impeller in the given region in the reactor.

$$\nabla \cdot \mathbf{v}\, C_{O_2} = v_x \frac{dC_{O_2}}{dx} + v_y \frac{dC_{O_2}}{dy} + \frac{v_z dC_{O_2}}{dz} \tag{2.2}$$

where v_i is the velocity component of the i coordinate. The oxygen transfer from gas to liquid phase depends on the interfacial area and liquid film resistance, as well as the driving force for mass transfer between the two phases [18]. The driving force is dependent on the solubility of oxygen, which is related to the partial pressure of oxygen in the gas phase.

$$OTR = k_L a \cdot \left(C^*_{O2} - C_{O_2}\right), \qquad C^*_{O_2} = K_H \cdot\, y_{O_2} \cdot P \tag{2.3}$$

where $k_L a$ is the volumetric mass transfer coefficient, $C^*_{O_2}$ is the oxygen solubility in the liquid, K_H is Henry's constant for oxygen in the liquid phase, y_{O_2} is the mole fraction of oxygen in the gas phase and P is the pressure at the given position in the reactor. The different factors affecting the rate of oxygen transfer are also not constant throughout a large scale fermenter, which further complicates the task of gaining a proper understanding of the occurrence of gradients in a large scale fermenter. Due to the action of the impellers in a stirred tank, the volumetric mass transfer coefficient is generally larger close to the impeller blades and smaller in between the impellers. The molar fraction of oxygen in the gas phase will decrease towards the top of the fermenter because of the consumption of oxygen by

the microorganisms, assuming that air sparging is done in the bottom of the fermenter. Additionally, the pressure is dependent on the liquid level resulting in higher pressure at the bottom of the fermenter compared to the top. The local pressure will also change due to changes in the liquid level that result from a fed batch operation. The pressure differences caused by the hydrostatic pressure in large scale fermenters are in the order of 1-3 bars depending on the height and the degree of filling of the fermenter.

The consumption of oxygen by the microorganisms depends on the local environment surrounding the organisms. The simplest and most common representation of the oxygen uptake rate is the growth associated Monod kinetic expression [19].

$$OUR = Y_{XO} \cdot \mu \cdot X, \qquad \mu = \frac{\mu_{max} \cdot C_s}{C_s + K_s} \tag{2.4}$$

where Y_{XO} is the yield of oxygen on biomass, μ is the microbial growth rate, X is the biomass concentration, μ_{max} is the maximum growth rate, C_s is the substrate concentration and K_s is the half saturation concentration of the given substrate. Assuming that the oxygen uptake rate follows the dependency described above, it is apparent that the spatial heterogeneity of the carbon source will dictate the local oxygen uptake rate. The evidence of glucose gradients in large scale bioreactors illustrated above would then infer proportional gradients in the uptake rate of oxygen if the glucose concentration is below the saturation concentration of the microorganism.

The dependency on different local conditions of the three governing phenomena responsible for changes in the oxygen concentration in the fermenter makes it nearly impossible to understand the fundamental causes for oxygen gradients. Evidence of the occurrence of oxygen gradients in large scale bioreactors has been available since the 80's, where the oxygen concentration was measured during aerobic fermentation by moving a sensor vertically [20,21]. The oxygen concentration differences were measured in a 112 m^3 fermenter cultivating *Streptomyces aureofaciens* equipped with four Rushton turbines resulting in a power input of 2.5 kW/m^3 [21]. A top to bottom gradient was identified at various conditions and viscosities with decreasing oxygen concentration towards the top of the reactor. The oxygen concentration was independent on radial position. Assuming that the mixing was sufficient to avoid spatial differences in carbon source concentrations, the reported oxygen concentration profiles can be explained by an increase in the solubility of oxygen at the bottom of the fermenter. Alternatively, the oxygen profile could be caused by a vertical gradient in carbon source due to feeding in the top of the fermenter, and limited axial convection that would suggest the observed gradient. Oosterhuis et al. (1984) [20] reported a severe change in oxygen concentration –

from 5 % to 25 % air saturation – around the impeller in a 19 m^3 fermenter equipped with two Rushton turbines. Contrary to the findings of Manfredini et al. (1983) [21], the vertical oxygen gradient was not dominant compared to the effect of the impeller action. Even though both fermenters had similar impeller configuration the measured oxygen gradient is fundamentally different in the two cases, which exemplifies the complexity of understanding the equilibria between convection, oxygen transfer and oxygen uptake rate.

2.6 The bottleneck of industrial aerobic fermentation processes

Mass transfer of oxygen from the gas phase to the liquid phase is for most aerobic fermentation processes the rate-limiting step [22]. The oxygen supply rate is thermodynamically limited due to the low oxygen solubility in water compared to the other substrates. In order to overcome this solubility bottleneck a large interfacial surface area between the phases inside the fermenter is achieved by sparging gas in the bottom of the fermenter. Process conditions, such as power draw from the agitator and aeration rate, and bioreactor configuration are known to affect the available surface area and mass transfer resistance. The understanding of how fermentation conditions affect this interfacial area and the mass transfer resistance, $k_L a$, have therefore been the subject of numerous research projects during the last four decades [23–26]. The mass transfer capabilities of bioreactors at lab scale, pilot scale and industrial scale have been investigated empirically and theoretically. Measuring the mass transfer capabilities of bioreactors is in itself a challenging task, but essentially relies upon measuring the rate of oxygen transfer at a known concentration of oxygen inside the bioreactor. A multitude of methods exist which facilitates the determination of the oxygen transfer rate, and it is considered beyond the scope of this work to illustrate the benefits and drawback of each approach. A comparison of the different empirical methods is available in in reviews such as [24,27–29]. The fundamentally different approaches to determine the correlation between $k_L a$ and fermentation conditions always converge to the following empirical correlation:

$$k_L a = K \cdot \left(\frac{P}{V}\right)^{\alpha} \cdot v_s^{\beta} \tag{2.5}$$

where K, α, β are constants, $\frac{P}{V}$ is the power draw per volume, v_s is the superficial gas velocity. Garcia-Ochoa et al. (2004) derived a theoretical correlation between power draw by the impeller, the gas flow rate and the mass transfer coefficient based on Kolmogorov's theory of isotropic turbulence [30], which proved to be comparable with the empirical findings. Similar for all studies and subsequent developed correlations is that they consider the power draw as the most important parameter

influencing the mass transfer coefficient. Increasing the power input to the fermenter will increase the oxygen transfer rate and subsequently the productivity of the fermentation process. The improved productivity per kWh is because the exponent α in Equation (2.5) is not linear, which results in a trade-off between productivity and cost of power input to the fermenter. Furthermore, the trade-off between energy efficiency of oxygen transfer and the rate of oxygen mass transfer is important to consider in particular at large scale [31].

2.7 Relationship between OTR and substrate gradients with oxygen controlled substrate feeding

Oxygen depletion in aerobic fermentation processes is a possible cause for by-product formation, and can lead to other suboptimal process scenarios. In order to avoid oxygen depletion in the fermenter the rate of substrate feeding can be manipulated. The substrate feeding can prevent oxygen depletion since it is directly coupled to the oxygen uptake rate as shown in Equation (2.4). If the oxygen concentration goes below the set-point the substrate feeding can be reduced whereas the feed rate is increased if the oxygen concentration exceeds the set-point. Employing oxygen dependent substrate feeding results in a direct coupling between the oxygen transfer capabilities and the oxygen uptake rate, and has been employed in bioreactors at different scale [32,33]. The manipulation of the feed rate in order to maintain the oxygen concentration can be achieved by different control strategies and methods, such as standard PID control, feedforward control or model predictive control. The efficacy of the different methods and their complexity is considered outside the scope of this work. The oxygen controlled substrate feeding does however also pose certain challenges in relation to controlling process heterogeneities. Due to the direct coupling between substrate addition and oxygen concentration, an increase in oxygen transfer rates will consequently increase the substrate feed rate. The increase in oxygen transfer can be justified by a need of achieving increased productivity, or even in order to mitigate concentration gradients by increasing mixing. The increase in substrate addition rate, due to the OTR increase, is not proportional to the increase in mixing efficiency at large scale, which can lead to further process heterogeneity.

2.7.1 Case study: 100 m^3 aerobic *E. coli* fermentation with oxygen dependent substrate addition

In order to illustrate the interdependency of oxygen transfer capacity and substrate feeding in aerobic fermentation processes a 100 m^3 *E. coli* fermentation is analyzed. The bioreactor configuration and culture conditions are summarized in Table 2.2.

Table 2.2 - Summary of geometrical parameters of the investigated fermenter, as well as microbial and thermodynamic conditions.

Fermenter conditions	Variable	Value	Unit
Filling volume	V	100	m^3
Aspect ratio	H/T	2.5	-
Width	T	3.49	m
Height	H	10.46	m
Impeller diameter	D	1.16	m
Number of impellers	N_I	4	-
Power number	Po	5.5	-
Flow number	F_l	0.74	-
Superficial gas velocity	v_s	0.174	m/s
Volumetric flow rate	VVM	1	$m^3/m^3/min$
Fermentation conditions			
Biomass concentration (*E. coli*)	X	40	g/L
Maximum growth rate	μ_{max}	0.6	h^{-1}
Saturation concentration	K_s	0.05	g/L
Yield of biomass on substrate	Y_{SX}	1.89	g/g
Yield of oxygen on biomass	Y_{OX}	1	g/g
Thermodynamics			
Pressure	P	1.01	bar
Oxygen set point	C_{O_2}	40	$\%\ saturation$[1]
Inlet molar fraction of oxygen in the gas phase	$y_{O_2,i}$	0.21	-
Outlet molar fraction of oxygen in the gas phase	$y_{O_2,o}$	0.15	-
Henry's constant for oxygen	K_H	0.04	$g/L/bar$

[1] **The saturation concentration is based upon ambient conditions at 25 $^\circ C$**

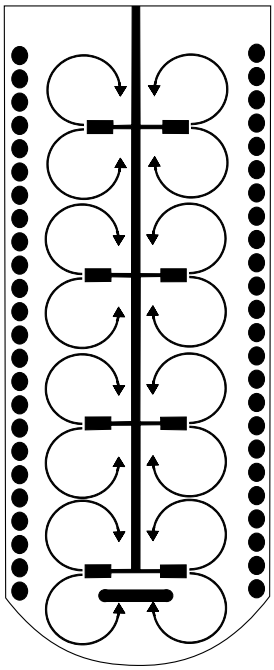

Figure 2.2 - Expected overall liquid flow profile in the stirred bioreactor with four Rushton turbines.

As explained above the mass transfer capacity of a bioreactor is generally the rate limiting step in aerobic fermentation processes, which means that an increase in mass transfer capacity will increase the productivity of the bioreactor. Achieving the desired increase in productivity is possible by increasing the agitation speed of the impeller and hence the overall mass transfer coefficient. The substrate feed rate and average glucose concentration as a function of the power input to the bioreactor can be determined from the mass balance of oxygen and glucose. This relationship is depicted in Figure 2.3.

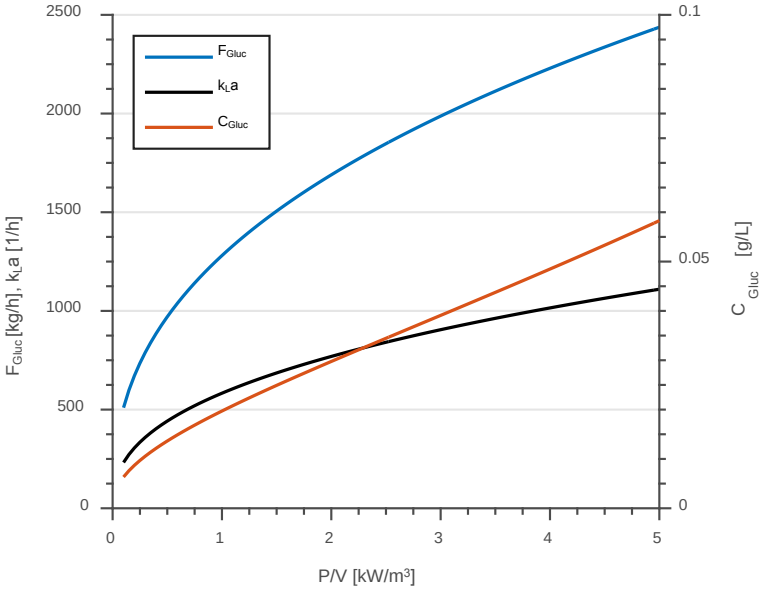

Figure 2.3 - Substrate feed rate, k_La and average glucose concentration as function of power input during oxygen dependent substrate feed in a 100 m³ stirred bioreactor.

Figure 2.3 shows how an increase in productivity directly affects the feed rate and subsequently the average glucose concentration, when operating at a constant oxygen concentration. Figure 2.3 clearly indicates the direct correlation between glucose feed rate and $k_L a$.

In order to estimate the substrate concentration in the bottom of the reactor, some assumptions about the hydrodynamics inside the fermenter are necessary. In the configuration studied, in this case employing four Rushton turbines, an assumption of four stirred tanks in series would be reasonable, and has been showed valid in tracer experiments in stirred reactors with multiple Rushton turbines. The substrate concentrations in the reactor as a function of power input can then be determined from the mass balance in each of the compartments. The mass balance of each compartment becomes:

$$0 = \frac{1}{\tau_{res}}\left(C_{Gluc,Feed} - C_{Gluc,1}\right) - \mu_{max} \cdot \frac{X}{Y_{sx}}\left(\frac{C_{Gluc,1}}{K_s + C_{Gluc,1}}\right) \tag{2.6}$$

$$0 = \frac{1}{\tau_{res}}\left(C_{Gluc,1} - C_{Gluc,2}\right) - \mu_{max} \cdot \frac{X}{Y_{sx}}\left(\frac{C_{Gluc,2}}{K_s + C_{Gluc,2}}\right) \tag{2.7}$$

$$0 = \frac{1}{\tau_{res}}\left(C_{Gluc,2} - C_{Gluc,3}\right) - \mu_{max} \cdot \frac{X}{Y_{sx}}\left(\frac{C_{Gluc,3}}{K_s + C_{Gluc,3}}\right) \tag{2.8}$$

$$0 = \frac{1}{\tau_{res}}\left(C_{Gluc,3} - C_{Gluc,4}\right) - \mu_{max} \cdot \frac{X}{Y_{sx}}\left(\frac{C_{Gluc,4}}{K_s + C_{Gluc,4}}\right) \quad (2.9)$$

where the indexes 1,2,3 and 4 refer to the compartments from top to bottom of the fermenter, $C_{Gluc,Feed}$ is the approximate feed concentration and τ_{res} is the residence time in each recirculation loop. The increase in power input to the fermenter results in increased fluid convection asserted by the impeller. The fluid convection, as mentioned previously, dictates the homogeneity of the substrates and can be quantified using a dimensionless group, the flow number.

$$Fl = \frac{Q}{D^3 \cdot N} \quad (2.10)$$

where Q is the volumetric flow rate discharged by the impeller, D is the width of the impeller and N is the agitation speed. The flow number has been studied for a number of different impellers and for a standard 6 blade Rushton turbine it is found to be 0.74 [34]. The discharge flow from the impeller combined with the feed rate can approximate the feed concentration by:

$$C_{Gluc,Feed} = \frac{F}{\frac{1}{2} \cdot Q} \quad (2.11)$$

The discharge flow is divided by two since only half the flow moves towards the top of the fermenter and influences the feed concentration as shown in **Figure 2.2**. The residence time in each stirred tank was assumed to be a fourth of the circulation time ($\tau_{res} = \frac{1}{4} \cdot \tau_{circ}$), which is defined as the average time a molecule spend being transported from the top of the vessel to the bottom and back again. The circulation time in industrial bioreactors has been showed to be approximately a fourth of the mixing time [33], which means that the residence time in each stirred tank becomes: $\tau_{res} = \frac{1}{16}\tau_{mix}$. The mixing time in stirred reactors with multiple Rushton turbines can be correlated to the impeller speed and geometrical features [34].

$$\tau_{mix} = 3.3 \cdot \frac{1}{N} \cdot \left(\frac{1}{P_o}\right)^{\frac{1}{3}} \cdot \left(\frac{D}{H}\right)^{-2.43} \quad (2.12)$$

where $P_o$is the power number of the impeller configuration. As shown in Figure 2.3 an increase in power input results in a higher feed rate in order to maintain the desired oxygen concentration in the fermenter. Increasing the power input also decreases the residence time in each of the compartments generated by the Rushton turbines, which affects the gradients observed in the reactor. The combined effect of these consequences is depicted in Figure 2.4 and compared with constant glucose feeding.

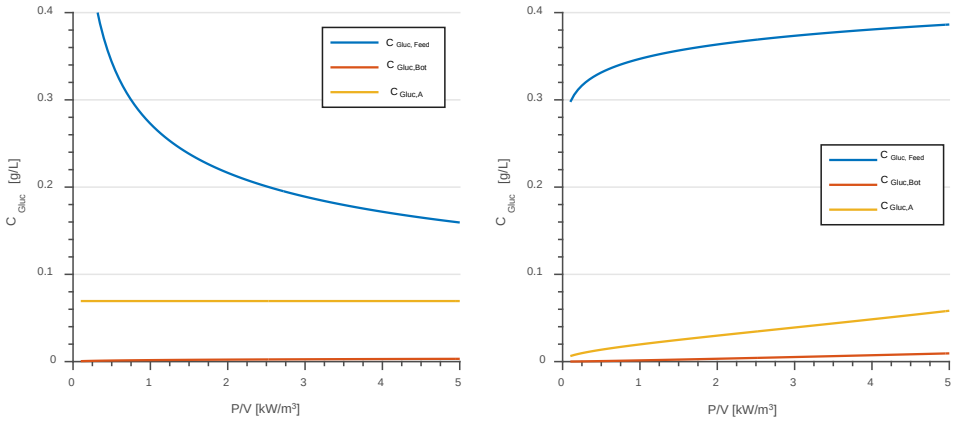

Figure 2.4 - Feed, average and bottom concentration of glucose in a 100 m³ fermenter equipped with four Rushton turbines cultivating *E. coli* at 40 g/L of biomass as a function of power input generated by the impeller. (a) shows the predicted gradients at constant feed rate and (b) shows the gradients when substrate addition is coupled to oxygen concentration.

The concentration difference between the feeding point and the bottom of the fermenter decreases as a function of dissipated power at constant feed rate as shown in Figure 2.4 (a). The improved mixing (higher P/V) lowers the residence time in the compartments formed by the impellers, which results in more homogeneous conditions. The correlation between concentration gradients and power input shown in Figure 2.4 (a) is intuitive and in agreement with what would be expected in a stirred bioreactor. If the substrate addition is coupled to the oxygen concentration, however, the correlation changes dramatically. Counterintuitively, the increase in agitation speed and thus power input does not result in increased homogenization inside the fermenter as shown by the constant concentration difference from top to bottom shown in Figure 2.4 (b). The increase in power draw of the impellers in the industrial size fermenter results in a substantial increase in the feed rate which scales with $k_L a$, but the mixing time scales with the inverse cubic root of the power. The case study examined shows that an increase in power input to the fermenter from one to four kw/m³ does not change the concentration gradient from top to bottom. Figure 2.4 clearly indicates that process control can affect the heterogeneities observed in an industrial scale stirred fermenter, which is an effect that is difficult to determine without the application of hydrodynamic models. The understanding of the hydrodynamics inside the fermenter and how it is affected by process manipulation should therefore be included when evaluating different control strategies of a fermentation process.

2.7.2 Gradients in bubble column fermenters

The relationship between process conditions and operational choices in aerobic bioreactors is not limited to stirred tanks, but also applies to bubble columns, airlift reactors etc. The analysis carried out for the industrial size stirred bioreactor in the previous section would be similar for a bubble column where only the relationship between k_La, mixing time and power input would change. The hydrodynamics inside a bubble column is generally defined as heterogeneous or homogeneous, which refers to the gas dispersion and behaviour [35]. For industrially relevant process conditions, which mainly refer to the oxygen transfer rate, the heterogeneous flow regime is dominant. The flow behaviour in the bubble column fermenter operating in the heterogeneous regime is characterized by a series of connected recirculation loops as seen in Figure 2.5. The process conditions of the investigated bubble column similar to the stirred fermenter described above are summarized in Table 2.3.

Table 2.3 - Summary of process parameters of the investigated bubble column fermenter.

Fermenter conditions	Variable	Value	Unit
Filling volume	V	100	m^3
Aspect ratio	H/T	5	-
Width	T	2.9	m
Height	H	14.7	m
Fermentation conditions			
Biomass concentration (*E. coli*)	X	40	g/L
Maximum growth rate	μ_{max}	0.6	h^{-1}
Saturation concentration	K_s	0.05	g/L
Yield of substrate on biomass	Y_{SX}	1.89	g/g
Yield of oxygen on biomass	Y_{OX}	1	g/g
Thermodynamics			
Pressure	P	1.01	bar
Oxygen set point	C_{O_2}	40	$\%\ saturation^1$
Inlet molar fraction of oxygen in gas phase	$y_{O_{2,i}}$	0.21	-
Outlet molar fraction of oxygen in gas phase	$y_{O_2,o}$	0.15	-
Henry's constant of oxygen	K_H	0.04	$g/L/bar$

[1] The saturation concentration is based upon ambient conditions at 25 °C

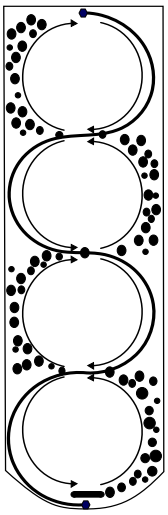

Figure 2.5 - Schematic drawing of the governing flow pattern in heterogeneous bubble columns. The arrows indicate the liquid flow recirculation and the solid line is the projected trajectory of substrate fed in the top of the fermenter.

In terms of fluid convection, the hydrodynamic behaviour in a bubble column fermenter similar to the one shown in Figure 2.5 is fundamentally different compared to a stirred tank. Since the convection in the bubble column is only generated from a density difference between gas and liquid, the convection becomes more unidirectional with larger recirculation loops. This orderly sequence of recirculation loops inside the heterogeneous bubble column has suggested that an assumption of plug flow behaviour could be a viable hydrodynamic model [36].

$$\frac{dC_{Gluc}}{dt} = -\mu_{max} \cdot \frac{X}{Y_{sx}} \cdot \left(\frac{C_{Gluc}}{C_{Cluc} + K_s}\right) \tag{2.13}$$

The plug flow assumption is a simplification of the flow pattern, since bubble induced turbulence and micromixing are ignored, but is useful for qualitative reasoning [37]. Determination of the concentration at the bottom of the bubble column fermenter is possible if the transport time from top to bottom is known. From the flow pattern sketched in Figure 2.5 it is apparent that the number of

consecutive recirculation loops is correlated with the aspect ratio. The distance that the added substrate will travel before reaching the bottom of the fermenter is approximately equal to:

$$L_{BC} = \frac{1}{2} \cdot \pi \cdot T \cdot \left(\frac{H}{T}\right) \tag{2.14}$$

The transport time from top to bottom of the bubble column depends on the fluid velocity and the transport distance explained in Equation (2.14). Heijnen et al. (1984) [35] showed that the liquid velocity, v_L can be correlated to the superficial gas velocity and column diameter.

$$v_L = 0.9 \cdot (g \cdot T \cdot v_s)^{\frac{1}{3}} \tag{2.15}$$

where g is the gravitational acceleration constant. The residence time of the substrate is determined by combining Equation (2.14) and (2.15):

$$\tau_{BC} = \frac{L_{BC}}{v_L} = \frac{\pi \cdot H}{1.8 \cdot (g \cdot T \cdot v_s)^{\frac{1}{3}}} \tag{2.16}$$

The residence time, τ_{BC}, depends on the geometrical features, and the operating conditions in the bubble column. Compared with the multi-impeller stirred tank, it is interesting that in spite of the difference between the two bioreactors the residence time scales with the inverse cubic root of the dissipated power. This relationship has previously been referred to as the universal mixing relation [36].

Applying the correlation of the residence time as boundary conditions to Equation (2.13) it is possible to investigate the relationship between glucose concentration and dissipated power in the bubble column. The concentration at the feed point, in the bottom and the average concentration over the column are shown as a function of dissipated power in Figure 2.6.

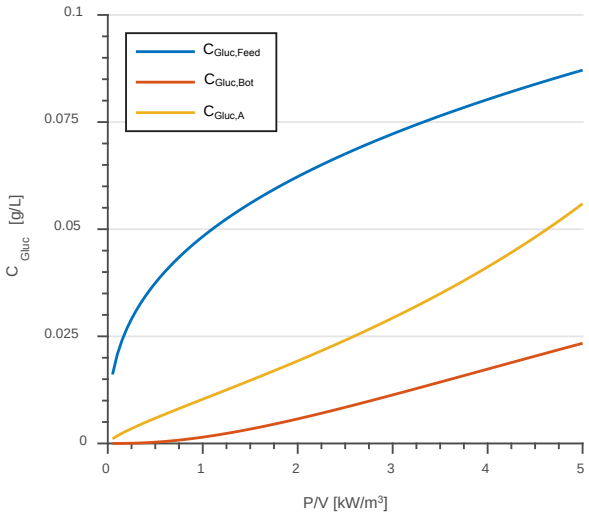

Figure 2.6 - Concentration profiles as a function of dispersed power input in a 100 m³ industrial bubble column reactor cultivating *E. coli*. The bubble column was fed in the top and is summarized in detail in Table 2.3.

The concentration profiles shown in Figure 2.6 indicate that as the power input to the bubble column is increased the concentration in the feed point and in the bottom of the column increase. The concentration gradient in the bubble column is increasing as the superficial gas velocity increases. This is due to the different proportionalities of the feed rate and the mixing time, respectively, to the power input. The feed rate scales with power input to the power of 0.7, whereas the residence time scales with power input to the power of -1/3, which means that the mixing cannot keep up with the feeding as the power input increases.

2.8 Strategies for identifying and mitigating potential gradients at large scale

The investigated cases show that concentration differences in the primary carbon source concentration are to be expected for an aerobic fermentation at high cell density. Furthermore, the desired control strategy has a direct influence on how the heterogeneities develop with increasing productivity. The simple correlations applied to both the agitated fermenter and the bubble column both indicate that faster processes do not lead to less process heterogeneities, if the substrate feeding is used as manipulated variable in order to maintain a certain oxygen concentration in the fermenter. The assumptions associated with the case studies presented here introduce some uncertainty about the quantitative results, but the conclusions are considered valid qualitatively.

Alternatively, to a correlation based model experimental methods can be used to illustrate possible scale-up issues in fermentation processes. Pilot scale testing as an intermediary step between development and production is a standard procedure in most biotechnological companies. In order to reduce cost and resources required in pilot scale testing a lot of research focus has been directed towards developing high throughput scale down systems with a working volume a thousand times smaller than pilot scale. Strategies for how the scaled down experiments can recollect large scale conditions have been illustrated with feeding strategies or connection of multiple reactors [38]. The challenge in designing the conditions and configurations of the scale down systems is that it implies detailed knowledge of large scale spatial distribution of process variables. This information is difficult to measure, and as illustrated above the measurements can be challenging to interpret with certainty. Advanced modeling approaches such as computational fluid dynamics (CFD) could be an alternative source of this detailed information, and CFD has proven to be a valuable tool to assess the hydrodynamics in stirred vessels at different scales [13,39–41]. The finite volume approach employed by commercial CFD software enables an assessment of the convectional flow in a fine spatial resolution in a fermentation vessel. This detailed information can be coupled with models of microbial kinetics and the spatial heterogeneities can be assessed in geometries identical to the production facility. The information obtained from the numerical simulation can then be used a guideline for scaled down operation and configuration [13]. Beside the potential assist in scale down simulator design CFD is a viable tool for improved process understanding and trouble shooting. The possibility to visualize large complex problems with high spatial resolution is a very useful tool in communications between laboratory development and production professionals.

2.9 Conclusion

Aerobic fed-batch fermentation is a widely applied process for manufacturing a number of biochemical intermediates, fine chemicals and pharmaceuticals. Industrial aerobic processes occur on a massive scale and in large fermentation vessels easily reaching several hundred cubic meters. The large size of the production vessels is beneficial for productivity since it reduces the number of batches per year and hence the time spent on cleaning between batches. The massive scale of the production fermenters poses a challenge in terms of process homogeneity and stability. This is particularly the case when carbon source feeding is used to maintain a certain concentration of oxygen in the fermenter, which ensures aerobic conditions. The coupling of substrate addition and oxygen concentration introduces a complex, and at certain conditions counterintuitive, correlation between power draw of the agitator on the one hand and top to bottom substrate gradients on the other hand.

As shown in the case study of a 100 m^3 stirred fermenter, an increase in the dissipated power results in the same concentration gradient from top to bottom. In a similar size bubble column the increase in dissipated power leads to an increase in the concentration difference. The two examples display how hydrodynamics play a key role in fermentation performance, and that understanding the relationship between hydrodynamics and microbial kinetics is essential in order to avoid unwanted process heterogeneities.

If process knowledge and understanding should be leveraged to improve the process performance of large scale aerobic fermentations, mathematical modelling has to be applied. Mathematical models of the microbial kinetics are available in the literature for numerous host organisms and mutants. Coupling the microbial kinetics to the hydrodynamics requires advanced models of the fluid mechanical behaviour inside large scale fermenters. CFD is a viable tool for the characterization of the fluid behaviour at large scale since it is able to account for geometrical features and fluid properties at scale. The combination of CFD and microbial kinetics has massive potential in both optimization of current processes and introduction of new processes with challenging traits.

2.10 References

[1] W.M. van Gulik, J.J. Heijnen, A metabolic network stoichiometry analysis of microbial growth and product formation, Biotechnol. Bioeng. 48 (1995) 681–698. doi:10.1002/bit.260480617.

[2] J. Villadsen, J. Nielsen, G. Lidén, Bioreaction Engineering Principles, 3rd ed., Springer, 2011. doi:10.1007/978-1-4419-9688-6.

[3] Y. Lin, S. Tanaka, Ethanol fermentation from biomass resources: Current state and prospects, Appl. Microbiol. Biotechnol. 69 (2006) 627–642. doi:10.1007/s00253-005-0229-x.

[4] F. Leroy, L. De Vuyst, Lactic acid bacteria as functional starter cultures for the food fermentation industry, Trends Food Sci. Technol. 15 (2004) 67–78. doi:10.1016/J.TIFS.2003.09.004.

[5] J.G. Zeikus, Chemical and fuel production by anaerobic bacteria, Annu. Rev. Microbiol. 34 (1980) 423–464. doi:10.1146/annurev.mi.34.100180.002231.

[6] J. Crater, C. Galleher, J. Lievense, J. Crater, C. Galleher, J. Lievense, Consultancy on Large-Scale Submerged Aerobic Cultivation Process Design – Final Technical Report, 2017.

[7] M.S. Croughan, K.B. Konstantinov, C. Cooney, The future of industrial bioprocessing: Batch or continuous?, Biotechnol. Bioeng. 112 (2015) 648–651. doi:10.1002/bit.25529.

[8] T. Dodge, Production of Industrial Enzymes, in: Enzym. Food Technol., Wiley-Blackwell, 2009: pp. 44–58. doi:10.1002/9781444309935.ch3.

[9] A.W. Nienow, W.H. Scott, C.J. Hewitt, C.R. Thomas, G. Lewis, A. Amanullah, R. Kiss, S.J. Meier, Scale-down studies for assessing the impact of different stress parameters on growth and product quality during animal cell culture, Chem. Eng. Res. Des. 91 (2013) 2265–2274. doi:10.1016/j.cherd.2013.04.002.

[10] S.O. Enfors, M. Jahic, a. Rozkov, B. Xu, M. Hecker, B. Jürgen, E. Krüger, T. Schweder, G. Hamer, D. O'Beirne, N. Noisommit-Rizzi, M. Reuss, L. Boone, C. Hewitt, C. McFarlane, A. Nienow, T. Kovacs, C. Trägårdh, L. Fuchs, J. Revstedt, P.C. Friberg, B. Hjertager, G. Blomsten, H. Skogman, S. Hjort, F. Hoeks, H.Y. Lin, P. Neubauer, R. Van der Lans, K. Luyben, P. Vrabel, Å. Manelius, Physiological responses to mixing in large scale bioreactors, J. Biotechnol. 85 (2001) 175–185. doi:10.1016/S0168-1656(00)00365-5.

[11] G. Larsson, M. Törnkvist, E. Ståhl Wernersson, C. Trägårdh, H. Noorman, S.O. Enfors, Substrate

gradients in bioreactors: Origin and consequences, Bioprocess Eng. 14 (1996) 281–289. doi:10.1007/s004490050218.

[12] M. Reuss, Oxygen Transfer and Mixing: Scale-Up Implications, Biotechnol. Set. (2001) 185–217. doi:10.1002/9783527620999.ch10b.

[13] C. Haringa, A.T. Deshmukh, R.F. Mudde, H.J. Noorman, Euler-Lagrange analysis towards representative down-scaling of a 22 m^3 aerobic S. cerevisiae fermentation, Chem. Eng. Sci. (2017). doi:10.1016/j.ces.2017.01.014.

[14] A.R. Lara, E. Galindo, O.T. Ramírez, L.A. Palomares, Living with heterogeneities in bioreactors, Mol. Biotechnol. 34 (2006) 355–381. doi:10.1385/MB:34:3:355.

[15] A.P.J. Sweere, K.C.A.M. Luyben, N.W.F. Kossen, Regime analysis and scale-down: Tools to investigate the performance of bioreactors, Enzyme Microb. Technol. 9 (1987) 386–398. doi:10.1016/0141-0229(87)90133-5.

[16] S. George, G. Larsson, K. Olsson, S.-O. Enfors, Comparison of the Baker's yeast process performance in laboratory and production scale, Bioprocess Eng. 18 (1998) 135–142. doi:10.1007/PL00008979.

[17] F. Bylund, E. Collet, S.-O. Enfors, G. Larsson, Substrate gradient formation in the large-scale bioreactor lowers cell yield and increases by-product formation, Bioprocess Eng. 18 (1998) 171–180. doi:10.1007/s004490050427.

[18] W.G. Whitman, The two film theory of gas absorption, Int. J. Heat Mass Transf. 5 (1962) 429–433. doi:10.1016/0017-9310(62)90032-7.

[19] J. Monod, The Growth of Bacterial Cultures, Annu. Rev. Microbiol. 3 (1949) 371–394. doi:10.1146/annurev.mi.03.100149.002103.

[20] N.M. Oosterhuis, N.W. Kossen, Dissolved oxygen concentration profiles in a production-scale bioreactor., Biotechnol. Bioeng. 26 (1984) 546–550. doi:10.1002/bit.260260522.

[21] R. Manfredini, V. Cavallera, L. Marini, G. Donati, Mixing and oxygen-transfer in conventional stirred fermenters, Biotechnol. Bioeng. 25 (1983) 3115–3131. doi:10.1002/bit.260251224.

[22] S.M. Stocks, Industrial enzyme production for the food and beverage industries : process scale up and scale down, in: Microb. Prod. Food Ingredients, Enzym. Nutraceuticals, 2013: p. 656.

doi:10.1533/9780857093547.1.144.

[23] V. Linek, T. Moucha, J. Sinkule, Gas-liquid mass transfer in vessels stirred with multiple impellers—II. Modelling of gas-liquid mass transfer, Chem. Eng. Sci. 51 (1996) 3875–3879. doi:10.1016/0009-2509(96)00015-2.

[24] K. Van't Riet, Review of Measuring Methods and Results in Nonviscous Gas-Liquid Mass Transfer in Stirred Vessels, Ind. Eng. Chem. Process Des. Dev. 18 (1979) 357–364. doi:10.1021/i260071a001.

[25] D. Hari-Prajitno, V.P. Mishra, K. Takenaka, W. Bujalski, A.W. Nienow, J. Mckemmie, Gas-liquid mixing studies with multiple up- and down-pumping hydrofoil impellers: Power characteristics and mixing time, Can. J. Chem. Eng. 76 (1998) 1056–1068. doi:10.1002/cjce.5450760612.

[26] C. Bandaiphet, P. Prasertsan, Effect of aeration and agitation rates and scale-up on oxygen transfer coefficient, kLa in exopolysaccharide production from Enterobacter cloacae WD7, Carbohydr. Polym. 66 (2006) 216–228. doi:10.1016/j.carbpol.2006.03.004.

[27] F. Garcia-Ochoa, E. Gomez, Bioreactor scale-up and oxygen transfer rate in microbial processes: An overview, Biotechnol. Adv. 27 (2009) 153–176. doi:10.1016/j.biotechadv.2008.10.006.

[28] V. Linek, P. Beneš, V. Vacek, F. Hovorka, Analysis of differences in kℓa values determined by steady-state and dynamic methods in stirred tanks, Chem. Eng. J. 25 (1982) 77–88. doi:10.1016/0300-9467(82)85024-7.

[29] M. Nordkvist, J. Villadsen, Mixing and mass transfer by rotating jets: Fundamentals and applications, 2006.

[30] A.N. Kolmogorov, The local structure of turbulence in incompressible viscous fluid for very large Reynolds numbers, Proc. R. Soc. 434 (1991) 9–13. doi:10.1098/rspa.1991.0075.

[31] M.O. Albaek, K. V. Gernaey, M.S. Hansen, S.M. Stocks, Evaluation of the energy efficiency of enzyme fermentation by mechanistic modeling, Biotechnol. Bioeng. 109 (2012) 950–961. doi:10.1002/bit.24364.

[32] L. Mears, S.M. Stocks, G. Sin, K. V. Gernaey, A review of control strategies for manipulating the feed rate in fed-batch fermentation processes, J. Biotechnol. 245 (2017) 34–46. doi:10.1016/J.JBIOTEC.2017.01.008.

[33] H. Noorman, An industrial perspective on bioreactor scale-down: What we can learn from combined large-scale bioprocess and model fluid studies, Biotechnol. J. 6 (2011) 934–943. doi:10.1002/biot.201000406.

[34] A.W. Nienow, Hydrodynamics of Stirred Bioreactors, Appl. Mech. Rev. 51 (1998) 3. doi:10.1115/1.3098990.

[35] J.J. Heijnen, K. Van't Riet, Mass transfer, mixing and heat transfer phenomena in low viscosity bubble column reactors, Chem. Eng. J. 28 (1984) B21–B42. doi:10.1016/0300-9467(84)85025-X.

[36] A. Groen, Macromixing in Bioreactors, Delft University of Technology, 1994.

[37] P.M. Raimundo, A. Cartellier, D. Beneventi, A. Forret, F. Augier, A new technique for in-situ measurements of bubble characteristics in bubble columns operated in the heterogeneous regime, Chem. Eng. Sci. 155 (2016) 504–523. doi:10.1016/j.ces.2016.08.041.

[38] S. Junne, Scale-down simulators for metabolic analysis of large-scale bioprocesses, Curr. Opin. Biotechnol. 21 (2010) 114–121. doi:10.1016/J.COPBIO.2010.02.001.

[39] D.D. McClure, N. Aboudha, J.M. Kavanagh, D.F. Fletcher, G.W. Barton, Mixing in bubble column reactors: Experimental study and CFD modeling, Chem. Eng. J. 264 (2015) 291–301. doi:10.1016/J.CEJ.2014.11.090.

[40] A. Liné, J.C. Gabelle, J. Morchain, D. Anne-Archard, F. Augier, On POD analysis of PIV measurements applied to mixing in a stirred vessel with a shear thinning fluid, Chem. Eng. Res. Des. 91 (2013) 2073–2083. doi:10.1016/j.cherd.2013.05.002.

[41] C. Bach, J. Yang, H. Larsson, S.M. Stocks, K. V Gernaey, M.O. Albaek, U. Krühne, Evaluation of mixing and mass transfer in a stirred pilot scale bioreactor utilizing CFD, Chem. Eng. Sci. 171 (2017) 19–26. doi:10.1016/j.ces.2017.05.001.

Chapter 3

Mixing and mass transfer in pilot scale fermentation vessel

The application of computational fluid dynamic models in fermentation systems is rarely based on industrially relevant conditions. This chapter showcases how CFD can be used to understand mixing and mass transfer in a pilot scale *Trichoderma reesei* fermentation at industrial relevant conditions. The chapter is based on the following published article:

Evaluation of mixing and mass transfer in a stirred pilot scale bioreactor utilizing CFD

Christian Bach, Jifeng Yang, Hilde Larsson, Stuart M. Stocks, Krist V. Gernaey, Mads O. Albaek & Ulrich Krühne

Chemical engineering science 171, 19-26, 2017

The following chapter is an exact reproduction of the article, but the formatting is adapted to that of the thesis.

3.1 Abstract

Knowledge and prediction of mixing and mass transfer in agitated bioreactors is fundamental for process development and scale up. In particular key process parameters such as mixing time and volumetric mass transfer coefficient are essential for bioprocess development. In this work the mixing and mass transfer performance of a high power agitated pilot scale bioreactor has been characterised using a novel combination of computational fluid dynamics (CFD) and experimental investigations. The effect of turbulence inside the vessel was predicted using a standard RANS k-ε model. Mixing time was investigated by carrying out sodium chloride tracer experiments for both Newtonian and non-Newtonian fluids at various viscosities and agitation speeds, while tracking the conductivity. The mixing performance was simulated with CFD and the results showed good agreement with the experimental data. The mass transfer coefficients were determined from six *Trichoderma reesei* fermentations at different well-defined process conditions. Similarly the mass transfer was predicted by Higbie's penetration model from two-phase CFD simulations using a correlation of bubble size and power input, and the overall mass transfer coefficients were in accordance with the experimental data. This work illustrates the possibility of predicting the two phase fluid dynamic performance of an agitated pilot scale bioreactor using validated CFD models. These models can be applied to illustrate the effect of changing the physical process conditions.

3.2 Nomenclature

Roman	Description	Unit
a	Specific surface area	$[m^{-1}]$
C	Impeller clearance	$[m]$
C_{O_2}	Liquid oxygen concentration	$[\mathrm{mol\ m^{-3}}]$
$C^*_{O_2}$	Saturation concentration of oxygen	$[\mathrm{mol\ m^{-3}}]$
d_b	Bubble size	$[m]$
D	Diameter of the impeller	$[m]$
H	Height of the bioreactor	$[m]$
k_L	Mass transfer resistance	$[m\ s^{-1}]$
K	Consistency index	$[Pa \cdot s^n]$
n	Flow index	[-]
P	Power input	$[kW]$
P_g	Gassed power input	$[kW]$
SMP	Sensitivity measure	[-]
T	Diameter of the bioreactor	$[m]$
OTR	Oxygen transfer rate	$[mol\ m^{-3}s^{-1}]$
v_g	Gas superficial velocity	$[m\ s^{-1}]$
V	Tank volume	$[m^3]$
$\mathcal{D}$	Diffusion coefficient	$[m^2s^{-1}]$
i	Inlet index	[-]
o	Outlet index	[-]
Greek	**Description**	**Unit**
α	Gas volume fraction	[-]
$\dot{\gamma}$	Shear rate	$[s^{-1}]$
ε	Eddy dissipation rate	$[W\ kg^{-1}]$
θ_{95}	Mixing time	$[s]$
μ_L	Liquid dynamic viscosity	$[kg\ m^{-1}s^{-1}]$
ρ_L	Liquid density	$[\mathrm{kg\ m^{-3}}]$
σ_M	The change for model output	[-]
σ_P	The change in parameter value	[-]
τ	Shear stress	$[Pa]$

3.3 Introduction

Production of cellulases for lignocellulose degradation can be carried out in submerged fermentations in stirred bioreactors [1]. *Trichoderma reesei* is known to use a highly efficient protein secretion mechanism, and is hence an excellent host for the production of cellulases and hemicelullases [2]. The growth of this filamentous fungus increases the viscosity of the medium, which can hinder the mixing and mass transfer capabilities of the fermenter. Mixing and mass transfer govern the spatial conditions in stirred fermenters, which emphasises the need for reliable models to predict these phenomena. Empirical models have successfully been used to facilitate this task, where process parameters have been correlated with process variables under certain conditions [3]. In particular the volumetric oxygen transfer coefficient and mixing time have received most attention in these studies as they are measures of the bioreactor performance [4–6]. In spite of the usefulness of empirical correlations, they often rely on certain geometrical constraints, and extrapolation of such models is often uncertain. In particular, the evolving conditions during fed-batch fermentations are difficult to capture in empirical correlations that are restricted by geometrical constants.

Models based on computational fluid dynamics (CFD) offer a route to become independent of empirical correlations, at the cost of computational effort. Compared to correlations based on global conditions CFD has the advantage of offering local conditions in the fermenter, which can be used to understand fluid flows and identify possible causes of insufficient mixing or mass transfer [7]. The mixing of Newtonian and non-Newtonian fluids has been successfully modelled using CFD for numerous geometries and bioreactor configurations [8–10]. Mass transfer predictions in gas-liquid systems using CFD have been reported previously for systems in which bubble size is a key parameter [11,12]. A few investigations have focused on aerobic fermentation systems in terms of mass transfer and mixing [7,13]. These studies revolve around a single operating point with regards to power input and in particular a fixed filling of the reactor which for fed-batch processes is known to have an impact on process performance [5]. Furthermore the continuous feeding can result in partly covered or just submerged impellers, which is difficult to investigate without CFD.

This work shows the applicability of CFD tools to represent one phase mixing at high power input in pilot scale fermenters. Furthermore a method to use a two phase CFD model to determine the mass transfer coefficient in high power agitated fermentation processes is described, which is validated with pilot process data.

3.4 Material and Methods

3.4.1 Tank geometry

The agitated bioreactor consisted of a baffled, torispherical-bottomed cylindrical vessel with a liquid height range of H=0.7-1.65T, leading to a loading volume range of 150-350 liters. A single impeller was employed in an up-pumping configuration. The geometry is similar to previous studies [14].

3.4.2 Mixing time experiments

The one phase mixing time was determined experimentally for both water (Newtonian) and Xanthan solutions (non-Newtonian) with varying concentrations. The Xanthan gum (Ziboxan®F80-Food grade, Deosen Biochemical Ltd.) solutions were prepared containing 0.125 and 0.25 % w/w along with 0.21 % w/w potassium hydrogen phosphate, which showed similar rheological behaviour as commonly used fermentation broth [15,16]. The agitation speeds applied during experiments were 150 RPM, 320 RPM and 400 RPM.

The mixing time was measured by injecting 300 mL of a 25 % w/w sodium chloride solution at the top of the reactor. The injection was achieved using three 100 mL syringes containing the tracer solution, and it was injected above the liquid level resulting in an even distribution of tracer at the top of the liquid. A conductivity sensor (Conducell 4 USF ARC 425 probe, Hamilton, Bonaduz, Switzerland) was mounted close to the bottom of the vessel. The response time of the conductivity sensor, fitted directly to a True RMS Digital Multimeter (Fluke, Everett, USA), was found to be less than 0.5 seconds. This enabled sufficiently fast signal response to capture the dynamics of the tracer injection. The mixing time in this work is defined as the time required to reach 95 % of the steady state conductivity, θ_{95}.

3.4.3 Rheological measurements

The rheology of Xanthan solutions and fermentation broths was characterized at 25 $^{\circ}C$ using a controlled strain and stress rheometer (ARG2, TA Instrument, DE) with a 1° gap angle cone-and-plate of 30 mm radius. The shear stress was evaluated at shear rates ranging from 1 s^{-1} to 500 s^{-1}.

3.4.4 Fermentation conditions

The *Trichoderma reesei* fermentations investigated in this work were previously described by Albaek et al. (2012). Feeding was employed with a controller to keep the oxygen concentration inside the tank at a given profile throughout the course of the fermentation. The fermentations were carried out at an impeller speed of 400 rpm and gas flow rates of 96 NL/min, 200 NL/min and 400 NL/min.

3.4.5 Measuring kLa

The direct method for k_La measurements was adopted by using a mass spectrometer (VG Prima dB, Thermo, Waltham, MA), and a flowmeter (Thermal mass flow meter, Endress & Hauser) to determine the overall mass transfer rate in the fermenter [6]. The mass transfer coefficient, k_La, is estimated by:

$$OTR = k_L a \left(\frac{\left(C^*_{O_2,i} - C_{O_2}\right) - \left(C^*_{O_2,o} - C_{O_2}\right)}{\ln\left(C^*_{O_2,i} - C_{O_2}\right) - \ln\left(C^*_{O_2,o} - C_{O_2}\right)} \right) \quad (3.1)$$

The saturation concentration of oxygen was calculated with help of Henry's law and was assumed to be constant throughout the fermentation. The liquid concentration of oxygen was measured using a commercial electrode mounted in the bottom of the vessel. The mass transfer coefficients were obtained by evaluating process data as the average over one hour time periods in order to eliminate fluctuations.

3.4.6 Model setup

One half volume of the reactor with 180° revolution was simulated by introducing symmetry, in order to reduce the number of mesh elements and computational time. Two computational domains were allocated for the rotational impeller and the stationary tank, respectively [17]. The simulated geometry is shown in Figure 3.1

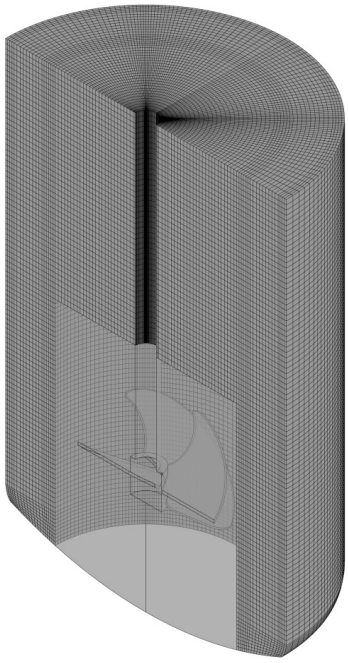

Figure 3.1 - Three dimensional drawing of half of the investigated geometry. The structured hexahedral mesh is shown for the tank region and the transparent region is the impeller zone. The cut plane in the geometry is used as a symmetrical boundary condition.

A structured hexahedral mesh for the stationary domain and an unstructured tetrahedral mesh for the rotary domain were separately established using ANSYS ICEM CFD 16. The interface of the two domains was designed to have matching element size in order to avoid numerical instability over the interface. In order to account for the changing volume caused by the continuous feeding in the fed batch fermentation a total number of six meshes were designed consisting of 2000 to 2500 elements per litre. The mesh density was comparable to other similar research [10]. A mesh sensitivity study was carried out to ensure mesh independent results. The details of this study can be found in the supplementary material of this manuscript.

The CFD simulations were performed using an average Navier-Stokes Euler-Euler approach in ANSYS CFX 16. The standard RANS k$-\varepsilon$ model was employed with a multiple reference frame interface approach for steady state runs and the Transient Rotor-Stator interface approach for unsteady state runs. A complete description of the boundary conditions can be found in the supplementary material section.

The non-Newtonian behaviour of the investigated fluids was simulated using the Ostwald de Waele correlation to determine the shear stress τ:

$$\tau = K\dot{\gamma}^n \tag{3.2}$$

where $\dot{\gamma}$ is the shear rate, K is the consistency index and n is the flow index.

The interaction of gas and liquid was accounted for using the Grace drag model [18] and a constant average bubble size was assumed. Experimental measurements were not available for the bubble size in the investigated system, and it was decided to adjust the bubble size according to the experimental mass transfer data. For this purpose a bubble size correlation considering the agitation speed was developed, which will be explained in a later section.

3.4.7 Mixing simulations

Transient simulations were carried out for the determination of the tracer distribution in the agitation vessel representing the mixing time experiments. This approach has been successfully applied in similar agitated vessels [9]. The tracer was simulated as an additional scalar variable without impact on the flow in the vessel with a diffusion coefficient of $2 \cdot 10^{-9}$ $m^2 s^{-1}$. Dosing of the tracer was carried out using a source point just below the surface of the liquid to represent the surface dosing applied in the experimental investigation.

3.4.8 Mass transfer simulations

The mass transfer resistance, k_L, multiplied with the specific surface area of the gas phase, a, yields the mass transfer coefficient, k_La. Higbie's penetration theory [19] was used to describe the mass transfer resistance throughout the vessel as

$$k_L = \frac{2\sqrt{\mathcal{D}}}{\sqrt{\pi}} \left(\frac{\rho_L \varepsilon}{\mu_L}\right)^{0.25} \tag{3.3}$$

where $\mathcal{D}$ is the diffusion coefficient of oxygen in water, ρ_L is the liquid density, μ_L is the viscosity of the liquid and ε is the eddy dissipation rate. The specific surface area of the air is, assuming spherical bubbles, determined as

$$a = \frac{6\alpha}{d_b} \tag{3.4}$$

where α is the volume fraction of air and d_b is the bubble size in the vessel. The spatial determination of mass transfer is therewith available from CFD simulations using these correlations as shown by [20,21].

3.5 Results and discussion

3.5.1 Rheology

The rheological behaviour of the investigated model fluids and the samples from the 23 fermentation conditions, shown in Figure 3.2, indicate the wide range of fluid properties encountered in fermentation processes.

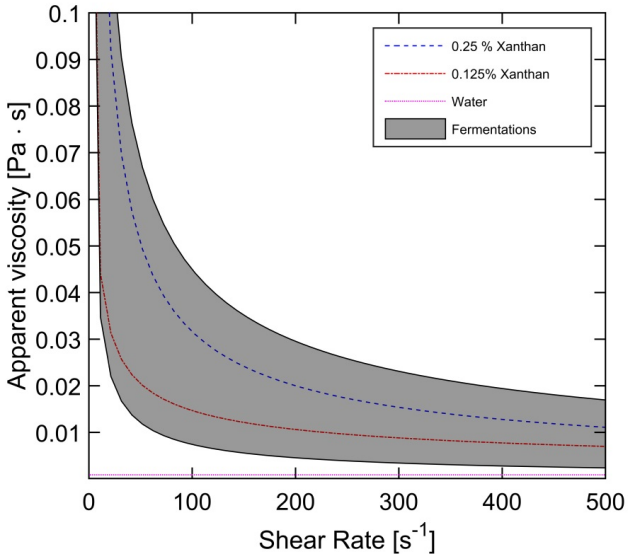

Figure 3.2 - Rheological behaviour of the investigated model fluids and fermentation broth samples approximated with the Ostwald de Waele model. The grey area indicates the ranges from the least to the most viscous samples of fermentation broth

The reasoning that Xanthan gum solutions are a viable model fluid for fungal fermentation broths is apparent in Figure 3.2, and the obtained rheological behaviour is comparable to previously reported findings [15,22]. Xanthan gum solutions are shear thinning, as the viscosity decreases with increasing shear rate. Correlated by the Ostwald de Waele model in Equation (3.2), the consistency and flow index for all investigated fluids are summarized in Table 3.1.

Table 3.1 - Consistency and flow index of the investigated model fluids and fermentation broths.

	0.125% Xanthan	0.25 % Xanthan	Fermentation broths
K [Pa s^n]	0.10	0.39	0.1-1.1
n [-]	0.56	0.41	0.28-6.3

3.5.2 Mixing

The effect of power input or agitation speed on the mixing time in a stirred tank has been shown to follow a hyperbolic trend for multiple stirrer configurations [3,5]. The experimentally determined mixing time of water and the xanthan solutions for the investigated power inputs is shown in Figure 3.3. The figure shows a decrease of the mixing time from 13 s to approximately 8 s when varying the power input from 0.5 to 9.4 kW m^{-3}, which follows the reported hyperbolic dependence of mixing time on power input. Power inputs above 2 kW m^{-3} result in a limited decrease of mixing time in the investigated range.

The accuracy of the mixing time prediction is shown in Figure 3.3, where it is apparent that the overall mixing dynamics are readily captured using the CFD model developed in this work. Multiple interesting traits of the hydrodynamics are apparent from Figure 3.3 such as the diminishing reduction in mixing time as the power input is increased. This indicates that the effect of increasing the power input in high power stirred tanks, with regards to the mixing time, is very dependent on the existing power input [5,23].

Another significant result is the effect of the working fluid on the mixing time, which generally shows little impact on the mixing time for all investigated conditions [5]. This effect is captured both in experimental and simulated results, which show the potential of using CFD as a tool to determine mixing performance in high power input agitated tanks.

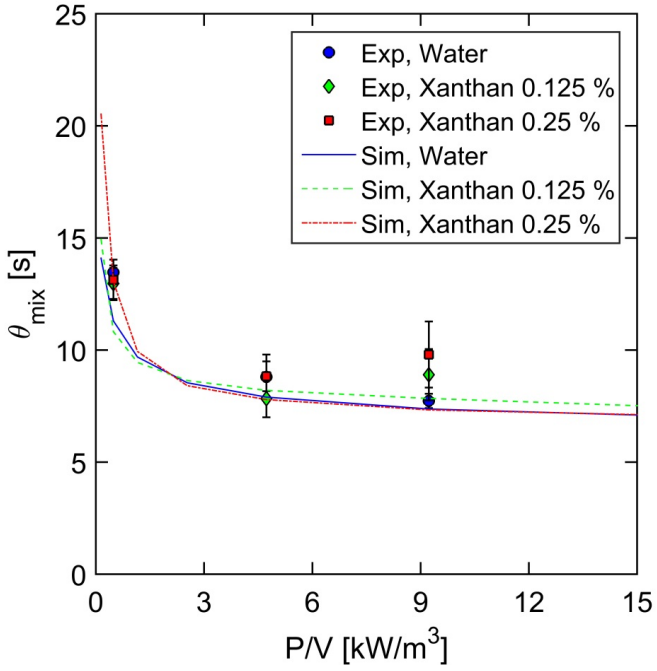

Figure 3.3 - Comparison of experimental and simulated mixing time for water, 0.125 % Xanthan and 0.25 % Xanthan. The error bars indicate one standard deviation obtained from triplicates.

3.5.3 Tracer experiments

Additionally to mixing time, the dynamic profile of tracer addition is an interesting characteristic of a bioreactor. A dynamic response of a tracer pulse indicates the dynamic characteristics of substrate or nutrient dispersion in the bioreactor, which is important to capture. The tracer profiles for water and 0.125 % xanthan at varying power input and the three model fluids at constant power input are shown in Figure 3.4.

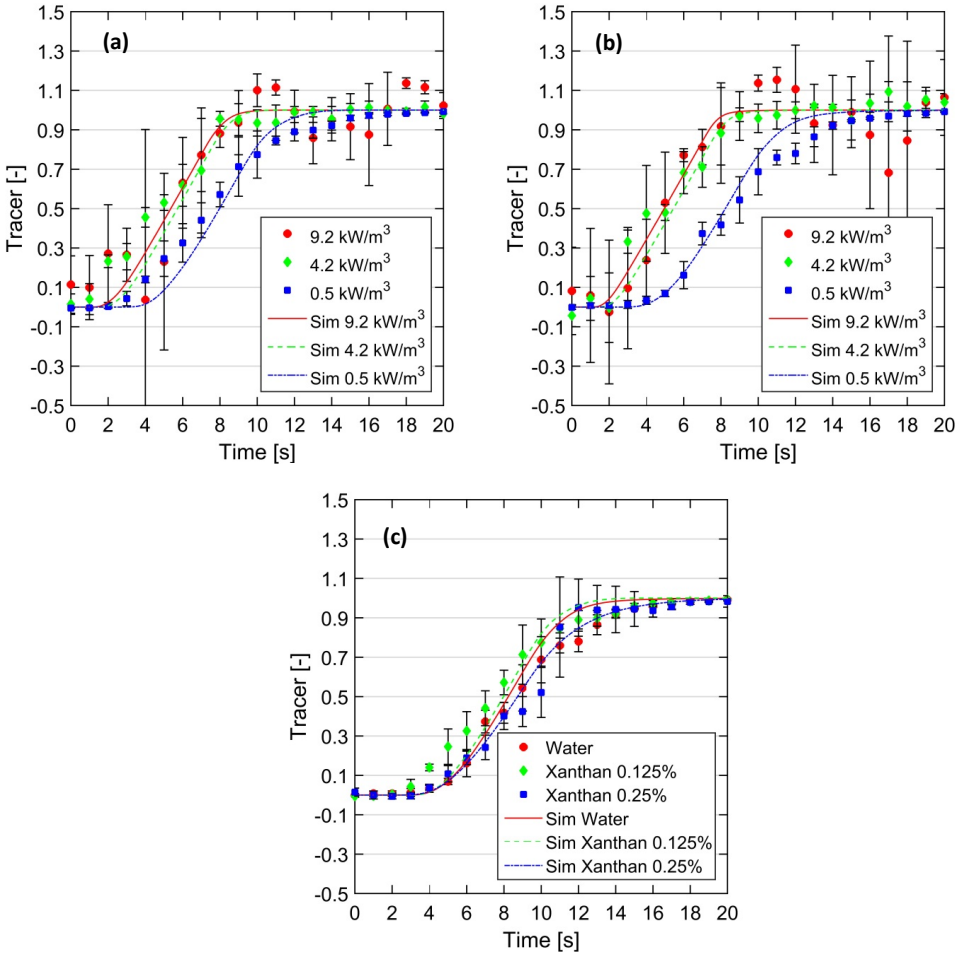

Figure 3.4 – Dimensionless tracer response to pulse injection for water at varying power input (a), 0.125 % Xanthan at varying power input (b) and the three fluids at 0.5 kw/m^3 (c). The error bars indicate one standard deviation obtained from triplicate experiments.

The dimensionless tracer profiles shown in Figure 3.4 share the same sigmoidal shaped curve, with only slight overshoot at power inputs of 9.2 kW m^{-3}. The power input to the system has a significant effect on the behaviour of the tracer, as clearly indicated in Figure 3.4 (a) and (b). The tracer profiles shown in Figure 3.4 (c) show that the type of fluid has little influence on the mixing of tracer. The uncertainty associated with the tracer profiles is likely caused by entrained air bubbles from surface aeration, which comes in contact with the conductivity sensor.

The simulated power input was compared to the measured value in terms of the resulting power number for relevant Reynolds numbers. This comparison is described in the supplementary material.

Comparing the experimental and simulated tracer profiles, for all investigated conditions and fluids, illustrates that the model is able to capture the dynamics of tracer addition. The ability to predict the tracer profile at process relevant conditions is an essential part in establishing confidence in CFD simulations in fermentation processes, as this exemplifies that substrate dispersion can be represented using such models.

3.5.4 Mass transfer

The prediction of mass transfer in stirred bioreactors using various simulation tools is extensively reported in literature [4,14,24–26]. Predicting the mass transfer in fed batch fermentation requires incorporation of the changing volume into the simulations. This was achieved by simulating multiple geometries corresponding to the conditions in a fed-batch fermentation. The rheology of the broth was altered for each simulation due to the growth of the *Trichoderma reesei*, which was taken into account in the model. The average bubble size was determined through an indirect method assuming that the mass transfer resistance k_L could be determined by Higbie's penetration theory [19]. This enabled an iterative approach to identify the required interfacial area that would give rise to the measured mass transfer coefficient. The iteration is carried out by changing the bubble size in the simulation, and after simulation convergence the predicted mass transfer coefficient is compared with the experimental data. The overall scheme is illustrated in Figure 3.5.

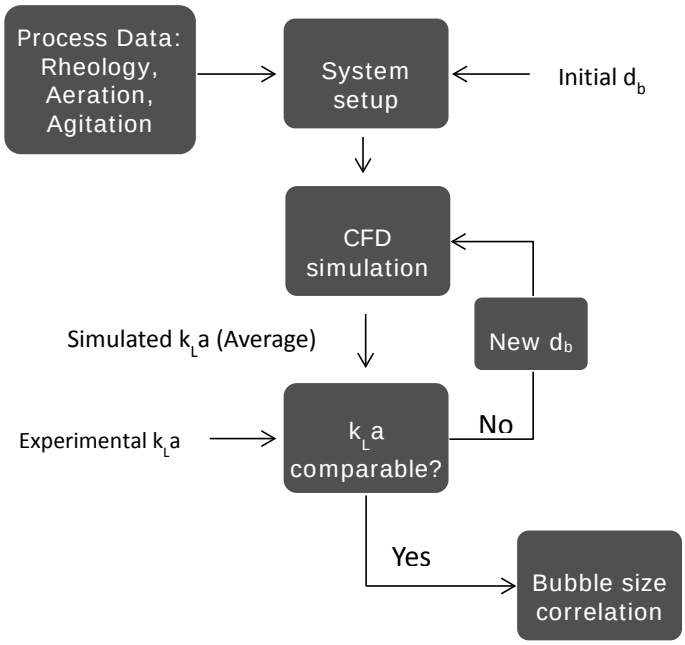

Figure 3.5 - Schematic illustration of the iterative process of determining the bubble size using CFD simulations and process data.

The indirect approach to determine the bubble size is attractive since it does not rely on experimental data of the bubble size. This is beneficial for industrial systems such as filamentous fermentation broths where such measurements are difficult and thus rare. However the computational demand of this method is substantial as it will require iterations of large two-phase simulations, which in cases with large geometries or a fine mesh will become time consuming. The method presented in Figure 3.5 was applied to 13 different conditions covering the three aeration rates and filling volumes of the fermenter. The comparability measure of the mass transfer coefficient was set to be 5% between experimental and simulated value. Figure 3.6 shows the resulting bubble size dependency of power input in the fermenter.

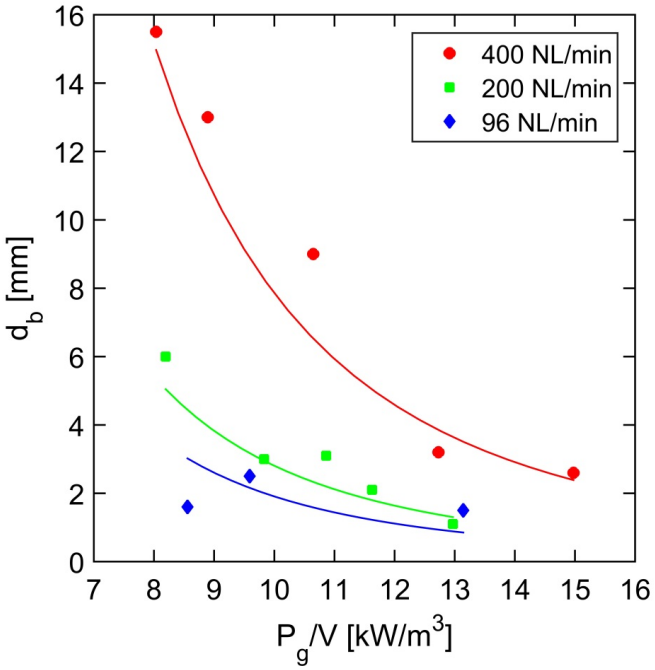

Figure 3.6 - Determined bubble size dependency on power input at different gas flow rates; 400 NL/min ●, 200 NL/min ■, 96 NL/min ♦. The solid lines indicate the respective correlation fit for the different conditions.

According to Figure 3.6 the bubble size varies from approximately 1 to 15 mm, which is similar to findings in studies where the bubble size was measured [27]. The bubble size is heavily correlated to the power input for the conditions investigated, and the correlation can be represented as:

$$d_b = C(v_g) \cdot \left(\frac{P_g}{V}\right)^{-2.95} \tag{3.5}$$

where C is a constant dependent on the gas flow rate and $\frac{P_g}{V}$ is the gassed power per volume ratio. Other literature correlations on bubble size include several effects such as viscosity, gas holdup and power dissipation [28]. The effect of power input is more severe in the correlation presented here compared to previous studies [28,29]. The previous correlations were developed considering the overall process parameters and not the hydrodynamics of the process, which is taken into consideration in the presented methodology. Furthermore the investigated fermentation broths in this study are non-Newtonian and shear thinning, which has not been investigated in the mentioned correlations.

In order to ensure that the simulations represent experimental data the model was validated with average k_La measurements gathered from three separate batches at identical conditions to the batches used for correlation development in terms of agitation and aeration. The validation result is evaluated in terms of a parity plot shown in Figure 3.7.

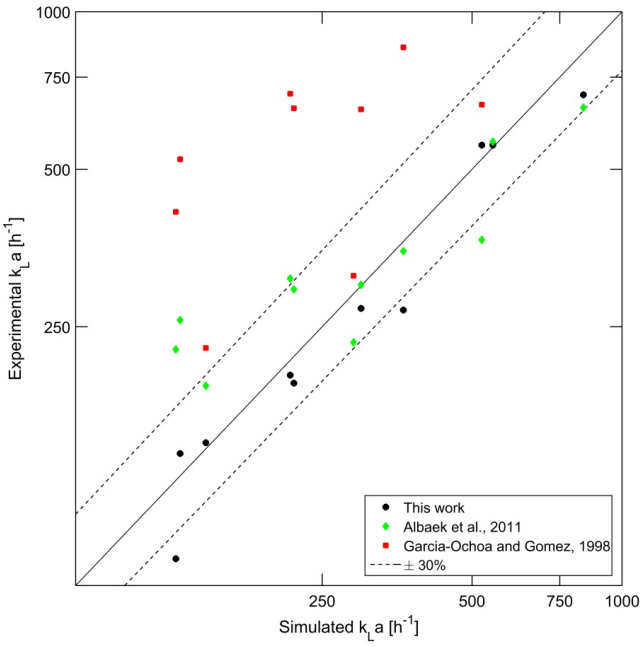

Figure 3.7 - Parity plot of experimentally obtained and simulated average k_La values for 10 fermentation conditions along with prediction from empirical correlations [4,30]. The dashed line indicates the ± 30 % deviation.

The model predicts the mass transfer coefficient to be within 30 % of the experimental value for 8 of the 10 conditions investigated as shown in Figure 3.7. Compared with other studies in the scientific literature the presented work achieves similar accuracy [4,5,31] without requiring complex measurements of bubble size. The assumption of an average bubble size, as well as using this bubble size correlation to fit the simulations to the experimental data within reasonable limits, is a viable approach to develop validated models. The variation in the parity plot data can also be associated with the uncertainty in k_La determination from fermentations.

The validated model can be used to identify spatial distribution of the mass transfer coefficient which is shown in Figure 3.8.

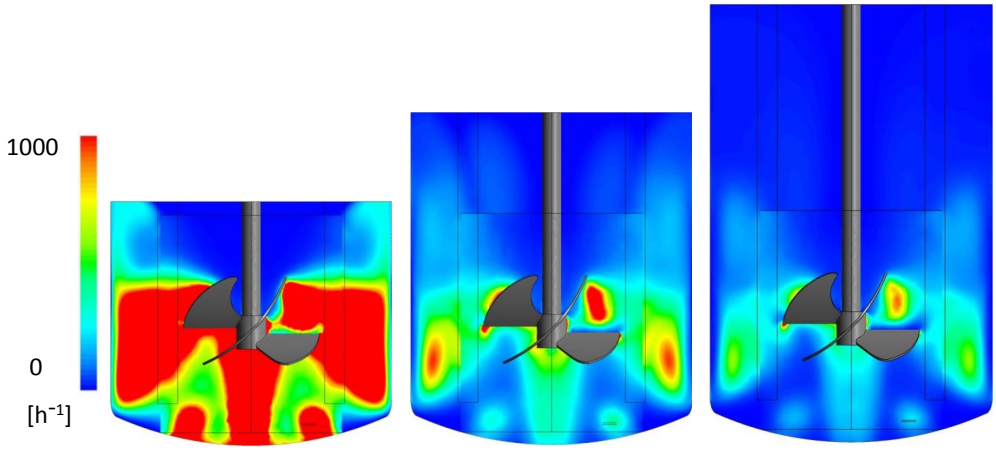

Figure 3.8 – Predicted distribution of k_La values for constant agitation and aeration with increasing volume and viscosity due to continuous feeding and subsequent growth.

The distribution of the mass transfer coefficient during the fermentation changes dramatically due to the increase in volume from the continuous feeding. Understanding the change in mass transfer coefficient during fed-batch fermentations enables better process control and optimization. The effect of the development in k_La distribution on microbial performance can be established by implementing fermentation stoichiometry and kinetics into the developed model. In this way, the CFD model can be converted to a tool that can be used for studying the effect of substrate gradients in larger tanks on the process performance.

3.5.5 Model Sensitivity

In order to address the applicability of the model, a sensitivity analysis was performed on the error propagation from the bubble size correlation to the mass transfer prediction. Previous studies revealed high sensitivity towards bubble size in two phase CFD simulations for bioreactors [32]. The uncertainty of the correlation fit to the data shown in Figure 3.6 is used as basis for estimating the model sensitivity. The error propagation was quantified by the least squares method described in [33]. The sensitivity of the CFD estimation of mass transfer was evaluated for a range of power inputs by determining the variation in model output from the bubble size correlation. The sensitivity measure, S_{MP}, is in this work defined as

$$S_{MP} = \frac{\sigma_M}{\sigma_p} \tag{3.6}$$

where σ_M is the change in model output and σ_p is the change in the parameter value. This measure is able to represent the scaled sensitivity of the model with regards to the input parameters [34]. The model sensitivity was evaluated in Figure 3.9.

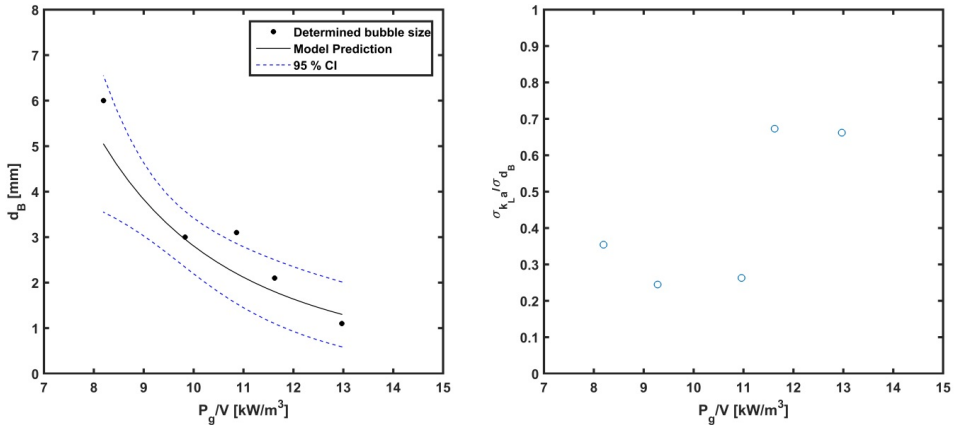

Figure 3.9 - Uncertainty of bubble size correlation at 200 NL/min (a) and subsequent impact on mass transfer prediction (b).

Figure 3.9 (a) shows that the relative uncertainty of the bubble size correlation is increasing with an increase in power input to the system from 30.4 % to 51.4 % at 8.2 kW m^{-3} and 13 kW m^{-3} respectively. Furthermore from Figure 3.9 (b) is it apparent that the sensitivity of the bubble size on the average k_La is largest at large power inputs with a value of 0.7 at a power input of 13 kW m^{-3}. The increased sensitivity can be explained by the small bubble size at high power input which causes a severe change in the k_La prediction.

The model sensitivity to bubble size is lower than one for all investigated cases indicating a dampening propagation of uncertainty in the developed CFD model. The sensitivity of the CFD model to changes in bubble size facilitates understanding of how certain a given correlation should be in order to obtain accurate predictions of mass transfer coefficients.

This sensitivity on bubble size is reassuring in the sense that an error in estimating the bubble size does not amplify through the mass transfer coefficient calculation. Such amplification would otherwise require a very high accuracy in the bubble size.

3.6 Conclusion

The performance in terms of mixing and mass transfer of a pilot scale fermenter with high power input has been experimentally investigated and simulated using commercial CFD software. The mixing characteristics of water and non-Newtonian xanthan gum solutions have been successfully represented by the developed model in terms of tracer profile and mixing time θ_{95} for power inputs from 0.5 to 9.2 kW m^{-3}. An indirect scheme has been developed to determine the bubble size in the fermenter using process data. The bubble size was shown to be dependent on the gas flow rate and power input for the investigated conditions, but independent on viscosity. The method was validated with independent data and proved to be as accurate as empirical correlations. Model sensitivity was assessed using linear error propagation and showed that the model has a dampening effect on uncertainty with regards to bubble size correlations. The method developed has shown a way to use and develop CFD simulations based on process data from industrial fed-batch fermentations. The derived CFD models and correlations can be used as a basis to also implement biological models to assess substrate dispersion and uptake rates.

3.7 Acknowledgments

Acknowledgments to Novozymes A/S and Lisa Mears for the experimental data used in this work. The project received financial support from Innovation Fund Denmark through the BIOPRO2 strategic research centre (Grant number 4105-00020B), Novozymes A/S and the Technical University of Denmark.

3.8 References

[1] R.M. Berka, J.R. Cherry, Enzyme biotechnology, Basic Biotechnol. (2006) 477–498.

[2] D. Martinez, R.M. Berka, B. Henrissat, M. Saloheimo, M. Arvas, S.E. Baker, J. Chapman, O. Chertkov, P.M. Coutinho, D. Cullen, E.G.J. Danchin, I. V Grigoriev, P. Harris, M. Jackson, C.P. Kubicek, C.S. Han, I. Ho, L.F. Larrondo, A.L. de Leon, J.K. Magnuson, S. Merino, M. Misra, B. Nelson, N. Putnam, B. Robbertse, A.A. Salamov, M. Schmoll, A. Terry, N. Thayer, A. Westerholm-Parvinen, C.L. Schoch, J. Yao, R. Barabote, R. Barbote, M.A. Nelson, C. Detter, D. Bruce, C.R. Kuske, G. Xie, P. Richardson, D.S. Rokhsar, S.M. Lucas, E.M. Rubin, N. Dunn-Coleman, M. Ward, T.S. Brettin, Genome sequencing and analysis of the biomass-degrading fungus Trichoderma reesei (syn. Hypocrea jecorina), Nat. Biotechnol. 26 (2008) 553–560. doi:10.1038/nbt1403.

[3] A.W. Nienow, Hydrodynamics of Stirred Bioreactors, Appl. Mech. Rev. 51 (1998) 3. doi:10.1115/1.3098990.

[4] M.O. Albaek, K. V. Gernaey, M.S. Hansen, S.M. Stocks, Modeling enzyme production with Aspergillus oryzae in pilot scale vessels with different agitation, aeration, and agitator types, Biotechnol. Bioeng. 108 (2011) 1828–1840. doi:10.1002/bit.23121.

[5] J.C. Gabelle, F. Augier, a. Carvalho, R. Rousset, J. Morchain, Effect of tank size on k La and mixing time in aerated stirred reactors with non-newtonian fluids, Can. J. Chem. Eng. 89 (2011) 1139–1153. doi:10.1002/cjce.20571.

[6] F. Garcia-Ochoa, E. Gomez, Bioreactor scale-up and oxygen transfer rate in microbial processes: An overview, Biotechnol. Adv. 27 (2009) 153–176. doi:10.1016/j.biotechadv.2008.10.006.

[7] D.D. McClure, J.M. Kavanagh, D.F. Fletcher, G.W. Barton, Oxygen transfer in bubble columns at industrially relevant superficial velocities: Experimental work and CFD modelling, Chem. Eng. J. 280 (2015) 138–146.

[8] L. Pakzad, F. Ein-Mozaffari, P. Chan, Using computational fluid dynamics modeling to study the mixing of pseudoplastic fluids with a Scaba 6SRGT impeller, Chem. Eng. Process. Process Intensif. 47 (2008) 2218–2227. doi:10.1016/j.cep.2007.12.003.

[9] A. Delafosse, M.L. Collignon, S. Calvo, F. Delvigne, M. Crine, P. Thonart, D. Toye, CFD-based compartment model for description of mixing in bioreactors, Chem. Eng. Sci. 106 (2014) 76–85. doi:10.1016/j.ces.2013.11.033.

[10] P. Moilanen, M. Laakkonen, J. Aittamaa, Modelling fermenters with CFD, Comput. Aided Chem. Eng. 20 (2005) 709–714. doi:10.1016/S1570-7946(05)80240-8.

[11] M. Laakkonen, P. Moilanen, V. Alopaeus, J. Aittamaa, Modelling local bubble size distributions in agitated vessels, Chem. Eng. Sci. 62 (2007) 721–740. doi:10.1016/j.ces.2006.10.006.

[12] S.U. Ahmed, P. Ranganathan, A. Pandey, S. Sivaraman, Computational fluid dynamics modeling of gas dispersion in multi impeller bioreactor, J. Biosci. Bioeng. 109 (2010) 588–597. doi:10.1016/j.jbiosc.2009.11.014.

[13] M. Laakkonen, P. Moilanen, V. Alopaeus, J. Aittamaa, Modelling Local Gas–Liquid Mass Transfer in Agitated Vessels, Chem. Eng. Res. Des. 85 (2007) 665–675. doi:10.1205/cherd06171.

[14] M.O. Albaek, K. V. Gernaey, M.S. Hansen, S.M. Stocks, Evaluation of the energy efficiency of enzyme fermentation by mechanistic modeling, Biotechnol. Bioeng. 109 (2012) 950–961. doi:10.1002/bit.24364.

[15] a. G. Pedersen, M. Bundgaard-Nielsen, J. Nielsen, J. Villadsen, O. Hassager, Rheological characterization of media containing Penicillium chrysogenum, Biotechnol. Bioeng. 41 (1993) 162–164. doi:10.1002/bit.260410121.

[16] M.O. Albæk, Evaluation of the efficiency of alternative enzyme production technologies, (2012).

[17] A. Ochieng, M. Onyango, CFD simulation of the hydrodynamics and mixing time in a stirred tank, Chem. Ind. Chem. Eng. Q. 16 (2010) 379–386. doi:10.2298/CICEQ100211040O.

[18] R. Clift, J.R. Grace, M.E. Weber, Bubbles, Drops and Particles, Academic Press, New York, USA, 1978.

[19] R. Higbie, The rate of absorption of a pure gas into a still liquid during short periods of exposure, Trans. Am. Inst. Chem. Eng. 31 (1935) 365–389.

[20] J. Gimbun, C.D. Rielly, Z.K. Nagy, Modelling of mass transfer in gas-liquid stirred tanks agitated by Rushton turbine and CD-6 impeller: A scale-up study, Chem. Eng. Res. Des. 87 (2009) 437–451. doi:10.1016/j.cherd.2008.12.017.

[21] K.M. Dhanasekharan, J. Sanyal, A. Jain, A. Haidari, A generalized approach to model oxygen transfer in bioreactors using population balances and computational fluid dynamics, Chem. Eng. Sci. 60 (2005) 213–218. doi:10.1016/j.ces.2004.07.118.

[22] J.C. Gabelle, E. Jourdier, R.B. Licht, F. Ben Chaabane, I. Henaut, J. Morchain, F. Augier, Impact of rheology on the mass transfer coefficient during the growth phase of Trichoderma reesei in stirred bioreactors, Chem. Eng. Sci. 75 (2012) 408–417. doi:10.1016/j.ces.2012.03.053.

[23] M.R. Marten, S. Velkovska, S. a Khan, D.F. Ollis, Rheological, Mass Transfer, and Mixing Characterization of Cellulase-Producing *Trichoderma reesei* Suspensions, Biotechnol. Prog. 12 (1996) 602–611. doi:10.1021/bp950066b.

[24] F. Garcia-Ochoa, E. Gomez, V.E. Santos, J.C. Merchuk, Oxygen uptake rate in microbial processes: An overview, Biochem. Eng. J. 49 (2010) 289–307. doi:10.1016/j.bej.2010.01.011.

[25] M. Laakkonen, Development and Validation of Mass Transfer Models for the Design of Agitated Gas-Liquid Reactors Development and Validation of Mass Transfer Models for the Design of Agitated Gas-Liquid Reactors, 2006.

[26] P. Moilanen, Modelling Gas-Liquid Flow and Local Mass Transfer in Stirred Tanks Modelling Gas-Liquid Flow and Local Mass Transfer in Stirred Tanks, 2009.

[27] P. Moilanen, M. Laakkonen, O. Visuri, V. Alopaeus, J. Aittamaa, Modelling mass transfer in an aerated 0.2 m3 vessel agitated by Rushton, Phasejet and Combijet impellers, Chem. Eng. J. 142 (2008) 95–108. doi:10.1016/j.cej.2008.01.033.

[28] F. Garcia-Ochoa, E. Gomez, Theoretical prediction of gas-liquid mass transfer coefficient, specific area and hold-up in sparged stirred tanks, Chem. Eng. Sci. 59 (2004) 2489–2501. doi:10.1016/j.ces.2004.02.009.

[29] S.S. Alves, C.I. Maia, J.M.T. Vasconcelos, a. J. Serralheiro, Bubble size in aerated stirred tanks, Chem. Eng. J. 89 (2002) 109–117. doi:10.1016/S1385-8947(02)00008-6.

[30] F. García-Ochoa, E. Gómez, Mass transfer coefficient in stirred tank reactors for xanthan gum solutions, Biochem. Eng. J. 1 (1998) 1–10. doi:10.1016/S1369-703X(97)00002-8.

[31] F. Garcia-Ochoa, E. Gomez, Prediction of gas-liquid mass transfer coefficient in sparged stirred tank bioreactors, Biotechnol. Bioeng. 92 (2005) 761–772. doi:10.1002/bit.20638.

[32] M. Mohajerani, M. Mehrvar, F. Ein-Mozaffari, CFD analysis of two-phase turbulent flow in internal airlift reactors, Can. J. Chem. Eng. 90 (2012) 1612–1631.

[33] M. Omlin, P. Reichert, A comparison of techniques for the estimation of model prediction

uncertainty, Sci. Technol. 115 (1999) 45–59.

[34] G. Sin, K. V Gernaey, A.E. Lantz, Good modelling practice (GMoP) for PAT applications: Propagation of input uncertainty and sensitivity analysis, Biotechnol. Prog. 25 (2009) 1043–1053.

Chapter 4

Bubble size distributions in a fed-batch *Trichoderma reesei* fermentation identified using an in situ optical measurement method

In this chapter, the bubble size distribution of a pilot scale fermenter is investigated using an endoscopic experimental approach. The purpose is to map the influence of process parameters on bubble size in industrial fermentations.

This chapter is submitted to a scientific journal and is only formatted to match the thesis layout. The article is authored by Christian Bach (PROSYS, DTU), Rayisa P. Moiseyenko (COMPUTE, DTU), Andreas Baum (COMPUTE, DTU), Thomas M. Jørgensen (COMPUTE, DTU), Ulrich Krühne (PROSYS, DTU), Sjef Cornelissen (Novozymes A/s), Mads O. Albaek (Novozymes A/S) & Krist V. Gernaey (PROSYS, DTU) author the article.

4.1 Abstract

A custom-made endoscopic measurement method able to detect bubble size distributions in industrial fermentation processes has been developed and tested in an aerobic *Trichoderma reesei* fermentation. The bubble size distributions were detected without altering the standard operating procedure. An image analysis algorithm was applied to specifically detect spherical and elliptical patterns in the viscous and turbid fermentation broth, which allowed a minimum of 70000 objects to be detected per sample. The number, area and volume based distribution were evaluated at eight different operating conditions during the fed-batch process. The Sauter mean diameter was found to depend on the power input to the power of -0.4 with a proportionality constant of 0.084 m. Investigations of the spread of the bubble size distributions showed that an increased power input resulted in more deterministic distributions, but the log-normal shape of the distributions was identified at all conditions. The method applied in this work is limited to detect bubbles between 0.1 and 10 mm in diameter due to the physical constraints of the measuring cell. The application of the technology in fermentation processes can lead to improved fundamental process understanding, relevant for complex numerical simulations, and process monitoring as an online assessment of the mass transfer potential.

4.2 Nomenclature

Roman	Description	Unit
a	Interfacial surface area	[m^{-1}]
d_B	Bubble diameter,	[m]
d_{32}	Sauter mean diameter	[mm]
C	Proportionality constant in bubble size correlation	[m]
D_{O_2}	Diffusion coefficient of oxygen in fermentation broth	[m^2/s]
F_A	Area based cumulative distribution function	[-]
F_N	Number based cumulative distribution function	[-]
F_V	Volume based cumulative distribution function	[-]
i	Index of bin number	[-]
k_L	Mass transfer coefficient	[m/s]
$k_L a$	Volumetric mass transfer coefficient	[1/s]
$\frac{P_G}{V}$	Gassed power input	[W/m^3]
P_A	Area based probability density function	[-]
P_N	Number based probability density function	[-]
P_V	Volume based probability density function	[-]
N	Number of bubbles in discrete bin	[#]
v_s	Superficial gas velocity	[m/s]
v_g	Gas flow rate	[NL/min]

Greek	Description	Unit
α	gas hold-up	[-]
β	exponent in bubble size correlation in Equation (4.2)	[-]
ϵ	Turbulent eddy dissipation rate	[m^2/s^3]
μ_{app}	Apparent viscosity	[Pa s]
ν	Kinematic viscosity	[m^2/s]

Abbreviation	Description
BSD	Bubble size distribution
CFD	Computational fluid dynamics

4.3 Introduction

Production of cellulase from submerged cultivations is an important part of the production of second-generation bioethanol [1]. Filamentous fungi, in particular *Trichoderma reesei* , have shown the ability to produce a cocktail of cellulases that efficiently degrade cellulose to fermentable sugars [2]. The industrial cultivation of *Trichoderma reesei* is carried out in large-scale aerobic fermenters, which is challenging because of the filamentous nature of the fungus [3]. Severe rheological changes during the fermentation become a limitation to the oxygen mass transfer capabilities and ultimately process productivity [3]. The oxygen transport is dependent on the mass transfer resistance and the available interfacial area between the gas phase and the liquid broth according to the classic film theory [4]. The overall rate coefficient of mass transfer $k_L a$ has been investigated for numerous processes and fermentation configurations, and the governing dependency on process conditions is known [5–7]. It is however not straightforward to deduct the effect of process conditions on the mass transfer resistance k_L or interfacial surface area a independently in industrial fermentation processes. In order to characterize the individual dependency of these parameters on process conditions, the mass transfer resistance or surface area must be known. Obtaining a predefined mass transfer resistance or interfacial surface area in a complex non-Newtonian fermentation broth with gas sparging is not feasible, because both variables depend on similar process characteristics [8]. In order to understand the effect of process conditions on the interfacial surface area, the bubble size and gas hold-up need to be measured. The interfacial area for dispersed spherical bubbles is dependent on gas hold-up and bubble size.

$$a = \frac{6 \cdot \alpha}{d_B} \tag{4.1}$$

where α is the gas hold up and d_B is the bubble diameter. This relation between interfacial area, gas hold-up, and bubble size is useful if empirical data of the gas hold-up and bubble size is available. Measuring the average gas hold-up in aerated fermentation processes is possible through a number of technologies, where visual inspection in a transparent vessel is the simplest [9]. Local gas hold-up measurements are much more challenging even in transparent vessels, where tomographic methods or multiple conductivity sensors remain the most viable options [10,11]. The determination of the size of gas bubbles is somewhat more challenging than measuring the gas hold-up, because it requires knowledge of the single bubbles contrary to the swarm of bubbles for gas hold-up measurements. Determination of bubble sizes in gas-liquid systems has been a subject of research for the past three decades, where new technologies have been assessed and compared with existing methods [12]. The

measurement of bubble sizes can generally be grouped into two distinctive groups namely: optical techniques or sensory techniques.

The sensory techniques rely upon measuring a change in signal as the gas bubbles reach one part of the sensor and then comparing it to the signal change when they reach another part of the sensor. Alignment and positioning of the two parts of the sensor is of upmost importance when converting the signals into bubble sizes [13]. The sensory techniques have been applied to many different gas-liquid systems, including bubble columns and stirred vessels [11,14,15].

Visual techniques rely upon capturing the size of the gas bubbles in a certain time span using conventional or high-speed camera equipment. Subsequently, the images are analysed to convert the detected objects from pixels in an image to a physical length scale. The acquisition of images can be carried out from outside the vessel looking through a transparent vessel or from inside the vessel using endoscopic techniques. External image capturing is technically straightforward except for avoiding image distortion, which can be mitigated by submerging the cylindrical reactor in a square transparent box [16]. The external visual technologies are limited to transparent vessels, which limits the industrial applicability of the technology to non-pressurized glass vessels [17]. Endoscopic techniques capture the bubble dynamics inside the reactor volume, and an endoscope is usually mounted through a process fitting. Different gas-liquid systems have been investigated using endoscopes as the primary source of size estimations or as a reference to benchmark sensory techniques [11,18]. Raimundo et al. 2016 [11] reported the bubble dynamics in a pilot scale bubble column using an 8 mm endoscope with illumination directly into the lens. However successful in determining the distribution of bubble sizes using this technique, a manual image analysis method had to be employed, which was inefficient and limited the sample size severely. Junker et al. (2007) [18] used a commercial setup (EnviroCam™) to investigate the bubble size distribution (BSD) in agitated fermentation vessels of different sizes. The setup consisted of an endoscope mounted with a LED housing to supply the required illumination. The setup was tested in a model liquid with different surfactant concentrations, and indicated the constraints of the technology at high gas hold-ups, where overlapping bubbles made it impossible to obtain a statistical distribution.

The correlation of process conditions and measured bubble sizes is generally described by the following equation:

$$d_{32} = C \cdot \left(\frac{P_g}{V}\right)^{\beta} \tag{4.2}$$

where d_{32} is the Sauter mean diameter, $\frac{P_g}{V}$ is the gassed power input to the vessel, and C and β are empirical constants. β has been found to depend mainly on the coalescence dynamics of the broth, being approximately -0.4 for non-coalescing and -0.14 for coalescing systems [12]. C reportedly depends mainly on the geometry of the system and is found by numerical fitting to experimental data [12].

The scope of this manuscript is to display the feasibility of a custom-made endoscopic setup to assess the BSD in a pilot-scale fermentation process with non-Newtonian culture broth. Furthermore, the application of a dedicated image analysing algorithm, which automates the detection and size estimation of bubbles, is explained. The effect of process conditions, such as agitation rate and aeration, is evaluated.

4.4 Materials and methods

4.4.1 Bioreactor configuration

The investigated *Trichoderma reesei* was cultivated in fed-batch operation in a 550 liter pilot scale fermenter with a single up-pumping impeller. Details of the fermenter are explained elsewhere [19,20]. The endoscope was installed in the bottom of the fermenter. In order to test the effect of power input on the bubble size, the agitation speed and aeration rate were altered from the operational set point for a ten minute period before acquiring the images. Between monitoring, the process was kept at constant agitation and aeration rate in order to avoid oxygen limitations. The images were collected over the course of 3 hours on average, and it is assumed that the viscosity of the fermentation media was not changing over the time course of the sampling.

4.4.2 Endoscope and high-speed camera

The endoscopic setup consisted of three separate parts: the high-speed camera, the endoscope and the fitting with illuminations.

4.4.2.1 High- speed camera

The high-speed camera used in this work was a Phantom Miro C110 from Vision Research, enabled to capture 800 frames per second at a resolution of 1280 x 1024 pixels. The camera was equipped with 8 GB of RAMs enabling a recording of approximately 4000 images per sample. An Ethernet cable connected the high-speed camera to a laptop PC for data transfer.

4.4.2.2 Endoscope

A C-mount was employed to connect the camera with a 10 mm HD Laparoscope from Olympus. The endoscope was thermostable, which allowed for a normal sterilization procedure with the endoscope installed. An O-ring and a nylon ferule ensured a leak-proof seal between the endoscope and the fitting.

4.4.2.3 Fitting with LED

In order to install the endoscope in the fermenter, a custom fitting was fabricated. The stainless-steel mount was fabricated with a housing for a 9 mm LED matrix from Cree, which delivers up to 49 W at 6400 lm. The fitting and housing of the LED are shown in Figure 4.1. The power supply to the LED was controlled externally, enabling tuning of the illumination of the gas bubbles in different process conditions.

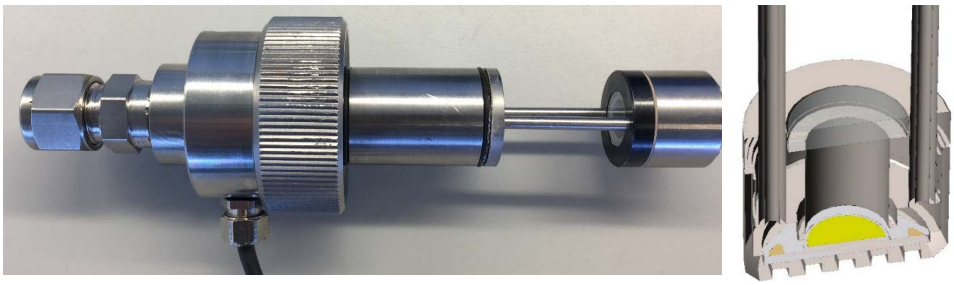

Figure 4.1 - Stainless steel fitting with LED housing (left). CAD drawing of LED housing (right) showing the Cree LED matrix and the complex design of the wiring.

The electrical wiring of the power supply to the LED was placed inside the support structure connecting the LED housing with the remainder of the fitting. This design enabled a relatively large LED to be included in the design, which is required to illuminate the investigated highly turbid fermentation broth.

4.5 Data acquisition and analysis Sample size

Image processing algorithms were implemented, in order to estimate the number of bubbles visible in each image frame. The criterion for counting a bubble is to observe a sufficient large arc of an ellipse being present in the image. Successively, the primary axis of the detected ellipse was used to estimate the size of the bubble. The essential part of the processing was based on an elliptical arc detector

published by V. Pătrăucean et al. 2012 [21]. This algorithm has been designed to minimize the number of false positive detections, by applying the so-called Helmholtz principle first stated by D. Lowe (1985) [22]. Furthermore, the algorithm is developed to avoid the need of image-dependent parameter tuning.

The algorithm operated on the spatial image gradients occurring in the grey scale images given by the video frames. The gradient changes across the borders of the recorded bubbles were sometimes too blurry for the algorithm to detect them robustly. This issue was solved by pre-processing the image frames with a contrast enhancement [23] followed by downscaling the images in order to assure steeper change in colour gradient [24]. Furthermore, the algorithm would occasionally detect a double border of the bubbles leading to double detection. This issue was solved by checking whether a detected ellipse contains another ellipse in its interior. In such cases the smaller one was neglected.

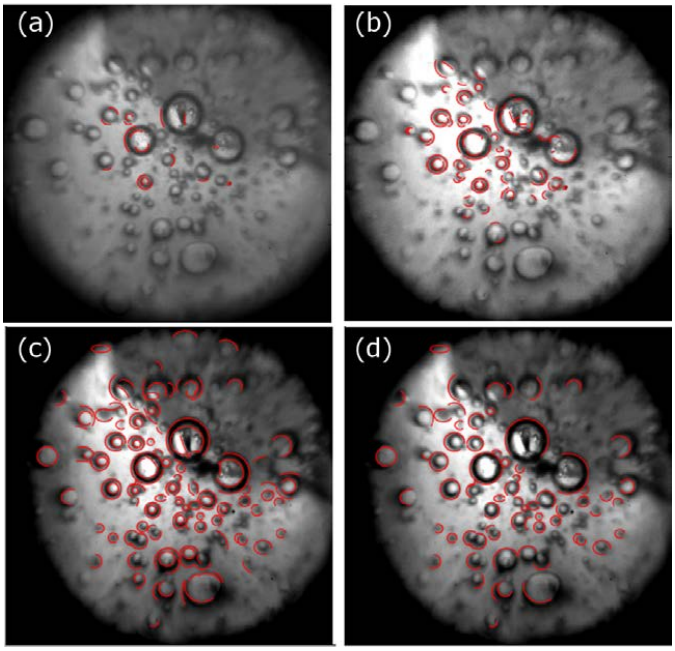

Figure 4.2 – A typical frame from the setup under varying stages in the image processing with the red lines indicating detected objects characterized by having an elliptic shape. (a) is the original image, (b) is the image after contrast enhancement, (c) is with additional downscaling and (d) shows the result of eliminating double detection.

Figure 4.2 shows the detected ellipses on the original image (a), after contrast enhancement (b), and after contrast enhancement combined with downscaling (c). The result after removal of double

detections is depicted in (d). The arc-segments whose angular extent was below 120 degrees were neglected. The selected scaling factor and contrast setting were chosen by applying scaling factors from 0.1 to one with step 0.1 and a contrast factor from one to eight with a step size of one and manually deciding which parameters gave the best performance from a given number of image frames.

The developed algorithm resulted in at least 70000 objects being captured for each process condition investigated, which formed the basis of the size distribution. The validation of the algorithm was done using 1 mm glass beads and is explained in detail in Appendix A1.

4.6 Results

4.6.1 Number, area and volume distributions

The output of the image detection algorithm is a vector containing the diameter of all detected objects at the given experimental condition. From the detected images, a size histogram can be calculated by indexing the particle sizes into a given number of bins/size intervals:

$$P(\overline{d_{B_i}}) = \frac{N_i}{\sum_i N_i}$$
$$\sum_i P(\overline{d_{B_i}}) = 1 \tag{4.3}$$

where $\overline{d_{B_i}}$ is the average diameter of the *i*-th bin. Evaluating the distribution of the bubble sizes in the process only based on the number of bubbles is not representative for processes where the area or volume of the bubbles has an important impact. In the study of gas liquid mass transfer the area and volume distributions are equally important to evaluate. The area and volume probability density function are defined as:

$$P_A(\overline{d_{B_i}}) = \frac{N_i \cdot \overline{d_{B_i}}^2}{\sum(N_i \cdot \overline{d_{B_i}}^2)} \tag{4.4}$$

$$P_V(\overline{d_{B_i}}) = \frac{N_i \cdot \overline{d_{B_i}}^3}{\sum(N_i \cdot \overline{d_{B_i}}^3)} \tag{4.5}$$

where P_A and P_V are the discrete area and volume based probability density function respectively. The different weights of the three probability density functions enable a thorough assessment of the distribution and the impact it has on process phenomena sensitive to the different weights. It is apparent that smaller bubbles at the investigated conditions dominate the number based distribution. The area and volume weighted probability density function are more dependent on large bubbles. The number, area and volume probability density functions for a gas flowrate of 200 NL/min and power input of 8.5kW/m^3 are shown in Figure 4.3.

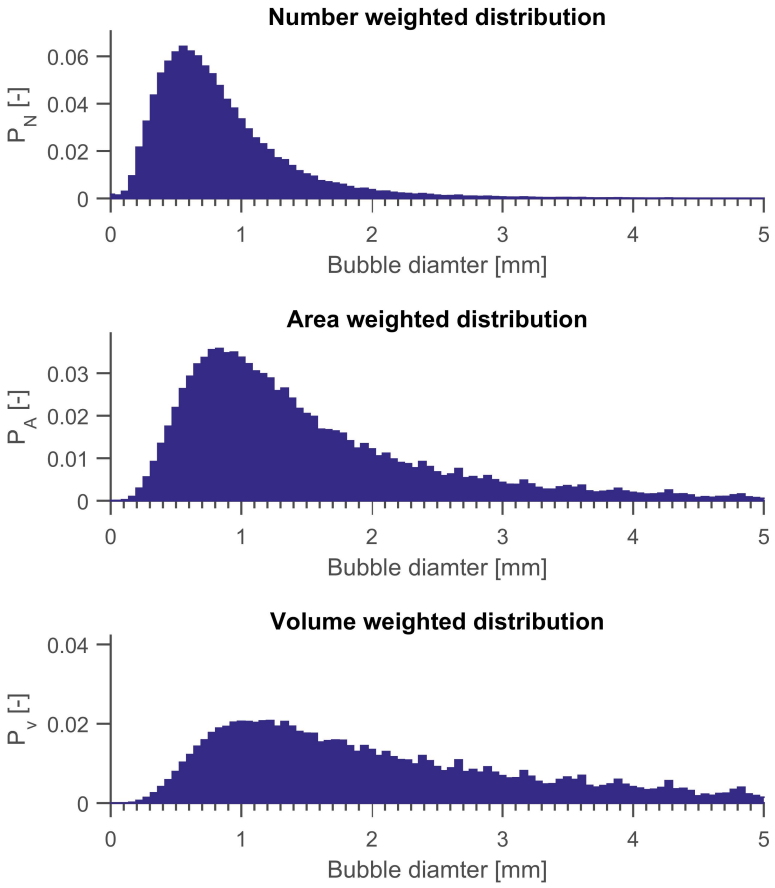

Figure 4.3 - Comparison of the discrete number, area and volume probability density functions of the bubble sizes at a power input of 8.5 kW/m^3 and gas flow rate of 200 NL/min. The distribution is discretized into two hundred bins.

Figure 4.3 shows that the mode of the distributions shifts as the weight is changed from number to volume. The number based probability density function has the same unimodal shape as previously reported for non-coalescing gas-liquid systems [25], even though the power input is almost an order of magnitude larger in this work. This analysis is based on an assumption of spherical bubbles, which from the collected images shown in Figure 4.2 is valid at the power inputs investigated. The comparison of the distributions can furthermore be based on the cumulative distribution function, which is expressed as:

$$F_N(d_B = k) = \sum_{i=0}^{k} P_N(d_B = i) \tag{4.6}$$

where $F_N(d = k)$ is the probability of the bubble being smaller than the discrete size k. The same relation between F and P is valid for the area and volume distributions. The cumulative distribution function for number, area and volume weighing is shown in Figure 4.4.

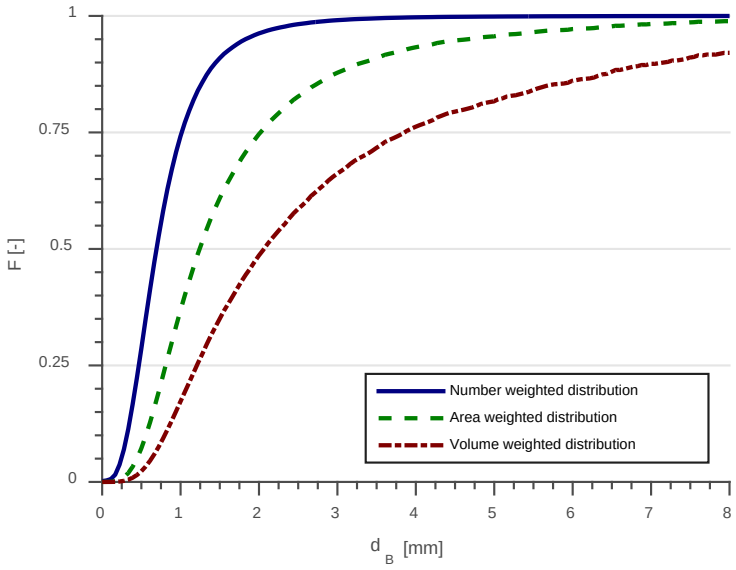

Figure 4.4 - Cumulative distribution function of number, area and volume weighted distribution of the bubble sizes at a power input of 8.5 kW/m3 and gas flowrate of 200 NL/min.

The cumulative distribution functions shown in Figure 4.4 indicate the difference in weighing the distributions by number, area and volume. Similar to Figure 4.3 it is apparent that a large part of the volume is accounted for by bubbles much larger than the median of a number based distribution. For instance, 25 percent of the volume of the distributions is made up by bubbles that are above 4 mm as seen by the red curve in Figure 4.4, which is approximately four times the number based median. The median of the different cumulative density functions are different, which supports the notion that the median of a distribution should be chosen with care.

4.6.2 Influence of gas flowrate and power input

The influence of power input on the bubble size in stirred gas-liquid systems has been studied in detail in numerous studies [12,18,26,27]. A comparison of the cumulative distribution function of the volume based distributions at different power inputs is shown in Figure 4.5.

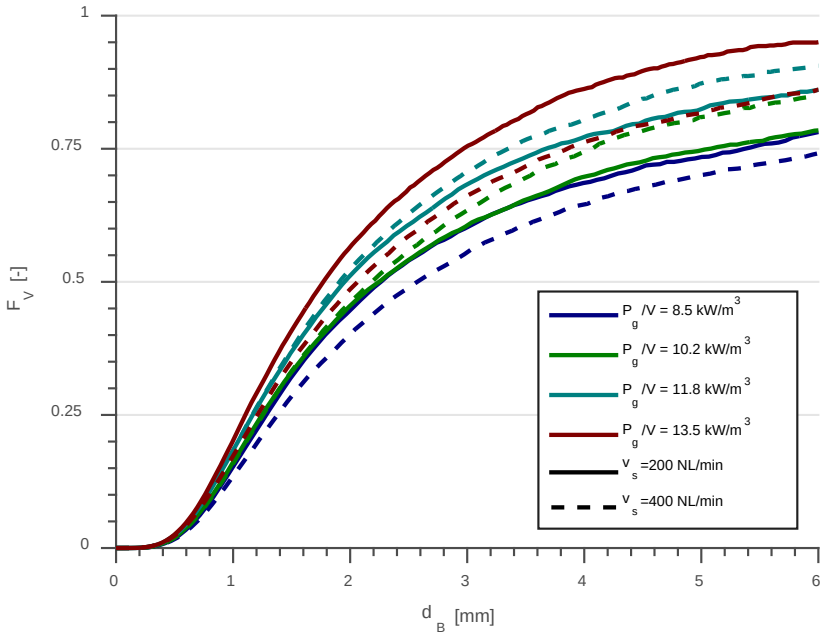

Figure 4.5 - An illustration of the effect of power input on the cumulative distribution function of a volume based BSD. The solid and dashed lines represents a gas flow rate of 400 and 200 NL/min repsectively.

Figure 4.5 shows how the volume based cumulative size distribution is affected by the gassed power input at different gas flow rates. The decrease in gassed power input infers an increase in the volume based median bubble size from approximately 1 to 1.5 mm in the investigated power input range at a gas flowrate of 400 NL/min. It is apparent that the increase in gassed power input decreased the bubble size in all investigated conditions, and that an increase in gas flow rate generally increases the volume based bubble size. The tendencies reported in Figure 4.5 confirm the findings of Junker et al. (2007) [18], who employed a similar technique to determine the bubble size.

Another commonly used metric to report the bubble size in gas-liquid systems is the Sauter mean diameter, which weighs the volume-based mean size with the area-based mean size [28]. The Sauter mean diameter is for a discrete size distribution determined by:

$$d_{32} = \frac{\sum N_i \cdot d_{B_i}^3}{\sum N_i \cdot d_{B_i}^2} \tag{4.7}$$

The Sauter mean diameter represents a bubble with the same volume to surface area as the entire population. A comparison of the estimated and measured Sauter mean diameter at the investigated conditions is shown in Figure 4.6.

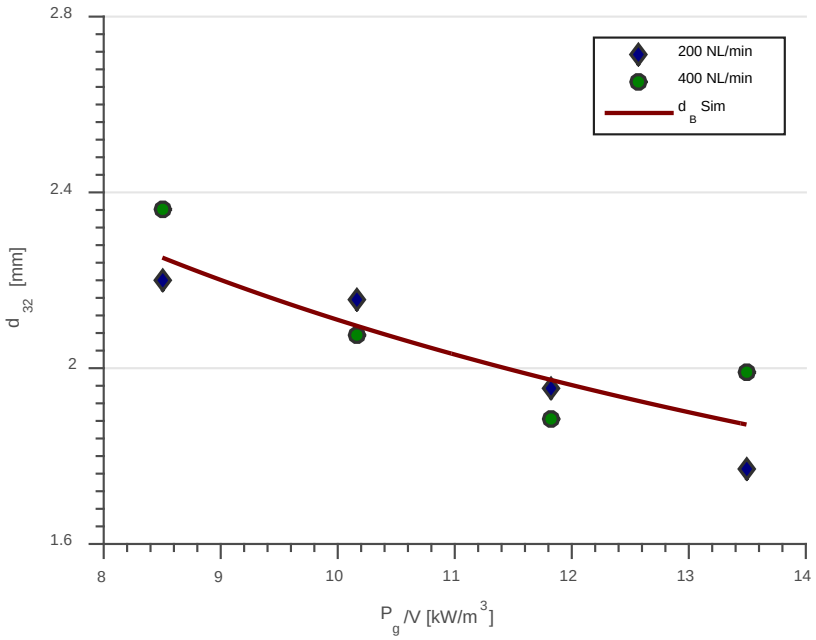

Figure 4.6 - Sauter mean diameter as a function of gassed power input at a gas flowrate of 200 NL/min (diamonds) and 400 NL/min (circles). The line indicates a predicted bubble size following Kolmogorov's theory of isotropic turbulence [29] with a proportionality constant of $C = 0.084\ m$.

The Sauter mean diameter of the eight investigated process conditions are shown in Figure 4.6, and indicate that the power input is the major contributor to the change in bubble size. The effect of the gas flowrate is negligible, similar to the results shown in Figure 4.5 , which confirms that the dominating effect is power draw of the impeller at least in the investigated range of conditions. A simple correlation between the Sauter mean diameter and the gassed power input similar to Equation (4.2)

has been fitted for the investigated conditions with an exponent of -0.4 and a proportionality constant of 0.084 m. This correlation is shown in Equation (4.8).

$$d_{32} = 0.084 \cdot \left(\frac{P_g}{V}\right)^{-0.4} \tag{4.8}$$

It should be noted that the proportionality constant and exponent on power input are sensitive and correlated, which means that the correlation should be used with care and only considered valid in the investigated range of power input. The expected dependency on power input from Kolmogorov's isotropic turbulence theory is confirmed by the correlation, which follows the data well [12]. The proportionality constant presented here is higher than previously reported by others [12], who found a proportionality constant of 0.016 m for a water-air mixture. The deviation might be because of the complex composition of the non-Newtonian fermentation broth. The mass transfer capabilities of the fermentation process investigated in this work has previously been characterized using Computational Fluid Dynamics and a correlation of the Sauter mean bubble diameter was developed [20]. The developed correlation based on numerical simulations suggested a stronger dependency of power input and a substantial influence of gas flowrate compared to the findings in this work. The Sauter mean diameter at different power inputs and 200 NL/min of gas flowrate does however correspond well with the numerical findings, where the measured Sauter mean diameters at 400 NL/min are smaller than the numerical findings. The numerical simulations were based on data from a full fed-batch, where the broth composition and reactor filling volume change, which could explain the difference in the two approaches. The broth rheology has been proposed to affect the coalescence frequency in gas liquid systems [30], and the filling volume will change the ratio between liquid height and impeller diameter, which will change the liquid flow inside the fermenter. In order to fully understand and compare the numerical finding with measured values more experiments or simulations must be carried out at identical process conditions.

4.6.3 Spread of the BSDs under different process conditions

Supplementary to the median and the Sauter mean diameter, the spread of the BSD is an interesting aspect to investigate. For a gas-liquid bubble column, the spread and shape of the BSD have shown to be highly affected by process conditions such as gas flowrate [31]. Besagni et al 2017 [31] showed for a 240 L bubble column that an increase of the superficial gas velocity from 0.0037 m/s to 0.018 m/s changed the median of the distribution severely but also shifted the BSD from a log-normal to a normal distribution in an air-water system. Laakkonen et al. (2005) [32] investigated the effect of stirred speed on the BSD in a 14 L stirred vessel equipped with a Rushton turbine. They found that the volume based

BSD shifted to smaller bubbles when increasing the stirred speed, and that the spread of the distribution decreased. The volume based BSDs are shown as boxplots in Figure 4.7 to assess the spread of the distributions across different process conditions.

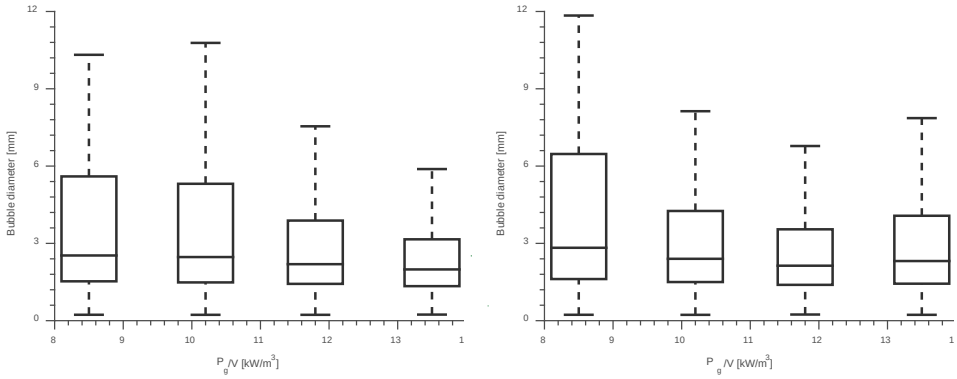

(a) **(b)**

Figure 4.7 – Boxplot of the volume based BSD at different power inputs at a gas flowrate of 200 NL/min (a) and 400 NL/min (b). The top and bottom line of the box indicate the 75th and 25th percentile respectively, where the horizontal line in the box represents the median. The whiskers indicate the extremes of the distributions, and outliers are not shown in these plots for simplicity.

Figure 4.7 shows the effect of increasing the power input on the spread and median of the BSD for a gas flowrate of 200 NL/min and 400 NL/min. The spread of the distribution are for both investigated gas flow rates higher at lower power input agreeing with literature findings in lab scale experiments. The spread, median and percentiles of the gas flowrates and power inputs are summarize in Table 4.1.

Table 4.1 - Summary of spread, median, 25th and 75th percentile for 8.5 and 13.5 kw/m^2 and 200 and 400 NL/min. The spread is determined as the difference between the 75th and 25th percentile.

Gas flow rate, v_g	**200 [NL/min]**		**400 [NL/min]**	
Power input, $\frac{P_g}{V}$	**8.5 [kW/m^3]**	**13.5 [kW/m^3]**	**8.5 [kW/m^3]**	**13.5 [kW/m^3]**
Median [mm]	2.5	2	2.8	2.3
25th percentile [mm]	1.5	1.3	1.6	1.4
75th percentile [mm]	5.6	3.2	6.5	4.1
Spread (75th-25th) [mm]	4.1	1.9	4.9	2.6

The median of the distribution does not vary significantly, whereas spread changes drastically at the different power inputs. The spread is reduced by almost 50 percent when the power input is increased from 8.5 to 13.5 for both gas flow rates, whereas the median is reduced by approximately 20 percent. The effect of the increased power input is for both investigated gas flowrates mainly in the fraction of large gas bubbles in each distribution Furthermore, Figure 4.7 shows that the shape of the BSD under varying conditions is similar, namely log normal in behaviour. Understanding how the spread of the distribution along with the median and 25 and 75 percentiles changes under different process conditions can be valuable both in fundamental understanding of the gas-liquid interaction and in numerical simulations of gas-liquid mass transfer in fermentation processes. The impact of the spread of the BSD in numerical simulation of fermentation processes is discussed in detail below.

4.7 Discussion

4.7.1 Effect of power input on bubble size in the context of mass transfer

The established dependency of power input on the Sauter mean diameter has interesting effects on mass transfer correlations. The bubble size is however only one of the variables that affect $k_L a$, and in order to investigate the effect of the bubble size on mass transfer, assumptions regarding the mass transfer coefficient and the gas hold-up are required. Combining the measured bubble sizes with a correlation for the gas hold-up the interfacial area, a, can be determined. In literature the dependency on power of the gas hold-up has been reported to be between 0.15 and 0.63 [8,9]. In this comparison two empirical correlations are used in order to illustrate the spread of the predictions obtained from empirical correlations of gas hold-up. The first correlation is from a 600 L fermenter equipped with a flat bladed turbine, and was derived at power inputs slightly lower than this work [36]. Their proposed correlation is shown in Equation (4.9).

$$\alpha = 32 \cdot \left(\frac{P_g}{V}\right)^{0.25} \cdot v_s^{0.75} \tag{4.9}$$

where v_s is the superficial gas velocity. The second correlation is derived from experiments with an up-pumping hydrofoil impeller in a reactor with an inner diameter of 0.29 m, where the power input was somewhat lower than investigated in this work [9]. The proposed correlation is shown in Equation (4.10).

$$\alpha = 0.2489 \cdot \left(\frac{P_g}{V}\right)^{0.6332} \cdot v_s^{0.5168} \tag{4.10}$$

The mass transfer coefficient has been showed by Kolmogorov's theory of isotropic turbulence to be dependent on the power input to the exponent of 0.25 [33], or by other authors been assumed independent of power input with a value of $4 \cdot 10^{-4}$ m/s [34]. The mass transfer coefficient can be expressed based on Kolmogorov's theory of turbulence as:

$$k_L = 0.4 \cdot \sqrt{D_{O_2}} \cdot \left(\frac{\epsilon}{\nu}\right)^{0.25} \tag{4.11}$$

where ϵ is the eddy dissipation rate, D_{O_2} is the diffusion coefficient of oxygen in the broth and ν is the dynamic viscosity of the broth. The eddy dissipation rate was determined from the power input and fermenter geometry as suggested by Garcia-Ochoa et al. (2004) [8] and the diffusion coefficient of oxygen in the broth was assumed to be $0.91 \cdot 10^{-9}$ m²/s [35].

The impact of the bubble size measurements on the volumetric mass transfer coefficient is tested in four scenarios in Figure 4.8, where different correlations of gas hold-up and mass transfer coefficient are combined. The scenarios are compared with a proven data driven correlation for $k_L a$ published previously [37]:

$$k_L a = 32 \cdot \left(\frac{P_g}{V}\right)^{0.53} \cdot v_s^{0.15} \cdot \mu_{app}^{-0.5} \tag{4.12}$$

where μ_{app} is the apparent viscosity. Both superficial gas velocity and apparent viscosity were determined from process data (data not shown). The correlation in Equation (4.12) is derived for the same process and in the same equipment as in this work making it a reasonable benchmark.

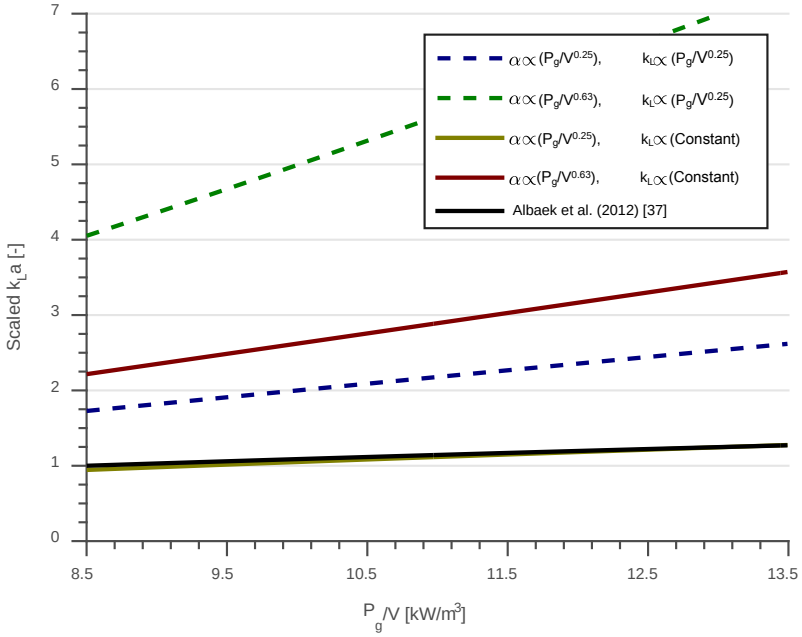

Figure 4.8- Scaled volumetric mass transfer coefficient assuming exponents of 0.25 and 0.63 on power input for gas hold-up and assuming expoennts of 0 and 0.25 on power input for the mass transfer coefficient. The predictions are compared with with the $k_L a$ correlation of Albaek et al. (2012) [37]. The $k_L a$ values are scaled for proprirytary reasons.

Figure 4.8 shows how the different correlations of gas hold-up and the mass transfer coefficeint affect the predictions of the volumetric mass transfer coefficeint using the bubble size data identified in this work. It is apparent that the predictions are quite diffirent to the correlation of Albaek et al. (2012)

[37], and that depending on how the gas hold-up and mass tranfer coefficent depend on the power input to the fermenter the $k_L a$ values deviate from the data driven correlation. From Figure 4.8 it appaers that an assumption of power input independent k_L values and a low dependency of gas hold-up is most comparible with the correlation, whereas the k_L predictions based on turbulence theory give rise to an overpredction compared to the correlation.

The correlations reported in literature of k_L and a do not all comply with the findings in the pilot scale fermentation investigated in this work. The cause of this deviation is impossible to determine with certainty without measuring the gas hold-up and $k_L a$ simultaneously. It is important to note that the exponents in the correlations $k_L a$ and gas hold-up are heavily correlated making these derivations uncertain in different geometries. A thorough study of the BSD and the gas hold-up under the industrial conditions in this work would be highly interesting, and could shed light on to whether the theoretical correlations of the parameters accounting for $k_L a$ are applicable in complex fermentation media.

4.7.2 Potential applications of in situ measurements of BSDs

A reliable tool able to assess the BSD in industrial fermentation vessels holds the potential to contribute to various parts of fermentation process development besides the fundamental insights illustrated in this work. Two potential applications are outlined in the following sections.

4.7.2.1 Bioprocess monitoring

Monitoring of bioprocesses revolves around retrieving information about process variables in real time in order to improve process stability and control. The variables available for monitoring are categorized as physical variables (Temperature, viscosity, pressure etc.), process variables (Oxygen, carbon dioxide, carbon source, pH etc.) and biological variables (Biomass, cell morphology, cell metabolism etc.) [38]. The range of physical variables available for monitoring could be extended to BSD if the endoscopic technique presented in this work was applied in a monitoring strategy. In order to use the equipment for monitoring purposes the data collection and analysis would have to be incorporated, but since the high-speed camera is compatible with MATLAB it should be realizable. On-line information of the BSD could serve as a valuable tool to understand the cause of insufficient oxygen supply during the process, in particular maintaining a stable oxygen concentration during anti-foam addition is an area of research interest. Similar visual techniques using an endoscope have been developed for biomass monitoring on-line, providing information of the microbial population in real time [39].

4.7.3 Clarification of assumptions used in Computational Fluid Dynamic simulations

Computational Fluid Dynamic (CFD) simulations of gas-liquid systems is greatly affected by the assumptions applied regarding the size and distribution of gas-bubbles [40]. The bubble size affects the fluid behavior in stirred vessels mainly through the drag coefficient responsible for momentum transport between the two phases. Current practice involves employing a population balance model approach in order to account for the breakup and coalescence of gas bubbles in the fermenter or the simplification of assuming a single bubble size [20,41,42]. The knowledge obtained from the measurement of the BSD can serve as a guideline for whether a full population balance modeling approach is required under the investigated conditions with CFD or whether the simplification of a deterministic BSD is sufficient. In particular, the ability to ascertain the effect of process conditions in an industrial setting can prove valuable in setting up CFD simulations. In some gas-liquid processes, the spread of the BSD could be small enough for the distribution to be assumed deterministic without a substantial simplification of the true distribution. Figure 4.7 showed that the spread of the distribution decreases with increasing power input, which would also indicate that in processes with a large power input the assumption of a single bubble size, is more valid.

4.8 Conclusion

The effect of power input and gas flowrate on BSDs in a *Trichoderma reesei* fermentation process has been showed to follow Kolmogorov's theory of isotropic turbulence. The measured Sauter mean diameter could be represented applying a proportionality constant of 0.084 m between 8.5 and 13.5 kw/m^3. The spread of the BSD was shown to decrease as a function of the power input to the fermenter, supported previous finding in lab scale systems. The findings presented show that the Sauter mean bubble diameter in a complex fermentation broth can be predicted by standard correlations, and that at constant gas hold-up the interfacial area is proportional with the power input to the power of -0.4.

The ability to determine the correlation between bubble size and power input in industrial fermentation systems empirically sheds light into the underlying mechanisms of gas-liquid mass transfer. The information obtained by this methodology can be combined with literature correlations and provide similar predictions of $k_L a$ as more classical approaches. It is however still required to study the gas hold-up and bubble size simultaneously under varying process conditions to characterize the mass transfer phenomena fully during industrial fermentations.

The presented technology can furthermore assist with increased process understanding and display fundamental relationships between process conditions and gas-liquid interactions. Additionally the sensor can also serve as an advanced tool in process monitoring to enable online assessment of the gas-liquid mass transfer. The fundamental understanding of the relationship between the BSD and process conditions can assist in developing models for CFD simulations of aerobic fermentation processes, which rely greatly on the assumptions regarding the size of gas bubbles. Employing the developed technology on a routine basis in industrial systems will inevitably give rise to additional applications of the developed optical measurement method.

4.9 Acknowledgements

The authors would like to acknowledge the Mafalda Dias Gomes for her assistance in the validation procedure and general contribution to the experimental part. Additionally the professionals of the fermentation pilot plant of Novozymes A/S are acknowledged for their corporation and willingness to allow this research. This project has received funding from Novozymes A/S, the Technical University of Denmark (DTU) and Innovation Fund Denmark in the frame of the Strategic Research Center BIOPRO2 (BIObased PROduction: TOwards the next generation of optimized and sustainable processes).

4.10 References

[1] M.R. Marten, S. Velkovska, S. a Khan, D.F. Ollis, Rheological, Mass Transfer, and Mixing Characterization of Cellulase-Producing *Trichoderma reesei* Suspensions, Biotechnol. Prog. 12 (1996) 602–611. doi:10.1021/bp950066b.

[2] D. Martinez, R.M. Berka, B. Henrissat, M. Saloheimo, M. Arvas, S.E. Baker, J. Chapman, O. Chertkov, P.M. Coutinho, D. Cullen, E.G.J. Danchin, I. V Grigoriev, P. Harris, M. Jackson, C.P. Kubicek, C.S. Han, I. Ho, L.F. Larrondo, A.L. de Leon, J.K. Magnuson, S. Merino, M. Misra, B. Nelson, N. Putnam, B. Robbertse, A.A. Salamov, M. Schmoll, A. Terry, N. Thayer, A. Westerholm-Parvinen, C.L. Schoch, J. Yao, R. Barabote, R. Barbote, M.A. Nelson, C. Detter, D. Bruce, C.R. Kuske, G. Xie, P. Richardson, D.S. Rokhsar, S.M. Lucas, E.M. Rubin, N. Dunn-Coleman, M. Ward, T.S. Brettin, Genome sequencing and analysis of the biomass-degrading fungus Trichoderma reesei (syn. Hypocrea jecorina), Nat. Biotechnol. 26 (2008) 553–560. doi:10.1038/nbt1403.

[3] E. Olsvik, B. Kristiansen, Rheology of filamentous fermentations, Biotechnol. Adv. 12 (1994) 1–39. doi:10.1016/0734-9750(94)90288-7.

[4] W.G. Whitman, The two film theory of gas absorption, Int. J. Heat Mass Transf. 5 (1962) 429–433. doi:10.1016/0017-9310(62)90032-7.

[5] M.O. Albaek, K. V. Gernaey, M.S. Hansen, S.M. Stocks, Modeling enzyme production with Aspergillus oryzae in pilot scale vessels with different agitation, aeration, and agitator types, Biotechnol. Bioeng. 108 (2011) 1828–1840. doi:10.1002/bit.23121.

[6] K. Van't Riet, Review of Measuring Methods and Results in Nonviscous Gas-Liquid Mass Transfer in Stirred Vessels, Ind. Eng. Chem. Process Des. Dev. 18 (1979) 357–364. doi:10.1021/i260071a001.

[7] J.M.T. Vasconcelos, a. W. Nienow, T. Martin, S.S. Alves, C.M. McFarlane, Alternative ways of applying the hydrogen peroxide steady state method of KLa measurement., Trans. Inst. Chem. Eng. 75 (1997) 467–472. doi:http://dx.doi.org/10.1205/026387697523967.

[8] F. Garcia-Ochoa, E. Gomez, Theoretical prediction of gas-liquid mass transfer coefficient, specific area and hold-up in sparged stirred tanks, Chem. Eng. Sci. 59 (2004) 2489–2501. doi:10.1016/j.ces.2004.02.009.

[9] T. Moucha, V. Linek, E. Prokopová, Gas hold-up, mixing time and gas-liquid volumetric mass transfer coefficient of various multiple-impeller configurations: Rushton turbine, pitched blade and techmix impeller and their combinations, Chem. Eng. Sci. 58 (2003) 1839–1846. doi:10.1016/S0009-2509(02)00682-6.

[10] R. Babaei, B. Bonakdarpour, F. Ein-Mozaffari, The use of electrical resistance tomography for the characterization of gas holdup inside a bubble column bioreactor containing activated sludge, Chem. Eng. J. 268 (2015) 260–269. doi:10.1016/j.cej.2015.01.042.

[11] P.M. Raimundo, A. Cartellier, D. Beneventi, A. Forret, F. Augier, A new technique for in-situ measurements of bubble characteristics in bubble columns operated in the heterogeneous regime, Chem. Eng. Sci. 155 (2016) 504–523. doi:10.1016/j.ces.2016.08.041.

[12] S.S. Alves, C.I. Maia, J.M.T. Vasconcelos, a. J. Serralheiro, Bubble size in aerated stirred tanks, Chem. Eng. J. 89 (2002) 109–117. doi:10.1016/S1385-8947(02)00008-6.

[13] A. Cartellier, Simultaneous void fraction measurement, bubble velocity, and size estimate using a single optical probe in gas-liquid two-phase flows, Rev. Sci. Instrum. 63 (1992) 5442–5453. doi:10.1063/1.1143416.

[14] D.D. Mcclure, J.M. Kavanagh, D.F. Fletcher, G.W. Barton, Development of a CFD Model of Bubble Column Bioreactors : Part One – A Detailed Experimental Study, (2013) 2065–2070. doi:10.1002/ceat.201300544.

[15] Y. Bao, L. Chen, Z. Gao, J. Chen, Local void fraction and bubble size distributions in cold-gassed and hot-sparged stirred reactors, Chem. Eng. Sci. 65 (2010) 976–984. doi:10.1016/J.CES.2009.09.051.

[16] V. Hudcova, V. Machon, a W. Nienow, Gas-liquid dispersion with dual Rushton turbine impellers., Biotechnol. Bioeng. 34 (1989) 617–628. doi:10.1002/bit.260340506.

[17] S.S. Alves, C.I. Maia, J.M.T. Vasconcelos, Gas-liquid mass transfer coefficient in stirred tanks interpreted through bubble contamination kinetics, Chem. Eng. Process. Process Intensif. 43 (2004) 823–830. doi:10.1016/S0255-2701(03)00100-4.

[18] B. Junker, W. Maciejak, B. Darnell, M. Lester, M. Pollack, Feasibility of an in situ measurement device for bubble size and distribution, Bioprocess Biosyst. Eng. 30 (2007) 313–326. doi:10.1007/s00449-007-0127-y.

[19] M.O. Albaek, K. V. Gernaey, S.M. Stocks, Gassed and ungassed power draw in a pilot scale 550 litre fermentor retrofitted with up-pumping hydrofoil B2 impellers in media of different viscosity and with very high power draw, Chem. Eng. Sci. 63 (2008) 5813–5820. doi:10.1016/j.ces.2008.08.024.

[20] C. Bach, J. Yang, H. Larsson, S.M. Stocks, K. V Gernaey, M.O. Albaek, U. Krühne, Evaluation of mixing and mass transfer in a stirred pilot scale bioreactor utilizing CFD, Chem. Eng. Sci. 171 (2017) 19–26. doi:10.1016/j.ces.2017.05.001.

[21] V. Pătrăucean, P. Gurdjos, R.G. Von Gioi, A parameterless line segment and elliptical arc detector with enhanced ellipse fitting, in: Lect. Notes Comput. Sci. (Including Subser. Lect. Notes Artif. Intell. Lect. Notes Bioinformatics), 2012: pp. 572–585. doi:10.1007/978-3-642-33709-3_41.

[22] Lowe. D, Perceptual Organization and Visual Recognition, Kluwer Academic Publishers, Amsterdam, 1985.

[23] P. Haeberli, D. Voorhies, Image processing by linear interpolation and extrapolation, IRIS Universe Mag. 28 (1994) 8–9.

[24] R. Grompone von Gioi, J. Jakubowicz, J.-M. Morel, G. Randall, LSD: a Line Segment Detector, Image Process. Line. (2012). doi:10.5201/ipol.2012.gjmr-lsd.

[25] V. Machon, A.W. Pacek, A.W. Nienow, Bubble Sizes in Electrolyte and Alcohol Solutions in a Turbulent Stirred Vessel, Chem. Eng. Res. Des. 75 (1997) 339–348. doi:10.1205/026387697523651.

[26] E. Galindo, A.W. Pacek, A.W. Nienow, Study of drop and bubble sizes in a simulated mycelial fermentation- broth of up to four phases, Biotechnol. Bioeng. 69 (2000) 213–221. doi:10.1002/(SICI)1097-0290(20000720)69:2<213::AID-BIT10>3.0.CO;2-D.

[27] G. Montante, D. Horn, a. Paglianti, Gas-liquid flow and bubble size distribution in stirred tanks, Chem. Eng. Sci. 63 (2008) 2107–2118. doi:10.1016/j.ces.2008.01.005.

[28] J. Sauter, Die Groessenbestimmung de rim Gemischnebel von Verbrennungskraftmaschinen Vorhandenen Brennstoffteilchen, Forschungsarbeiten Auf Dem Gebiete Des Ingenieurwesens. (1926) 279.

[29] A.N. Kolmogorov, The local structure of turbulence in incompressible viscous fluid for very large Reynolds numbers, Proc. R. Soc. 434 (1991) 9–13. doi:10.1098/rspa.1991.0075.

[30] T. Wang, J. Wang, Y. Jin, A novel theoretical breakup kernel function for bubbles/droplets in a turbulent flow, Chem. Eng. Sci. 58 (2003) 4629–4637. doi:10.1016/J.CES.2003.07.009.

[31] G. Besagni, F. Inzoli, The effect of electrolyte concentration on counter-current gas–liquid bubble column fluid dynamics: Gas holdup, flow regime transition and bubble size distributions, Chem. Eng. Res. Des. 118 (2017) 170–193. doi:10.1016/J.CHERD.2016.12.012.

[32] M. Laakkonen, P. Moilanen, T. Miettinen, K. Saari, M. Honkanen, P. Saarenrinne, J. Aittamaa, Local bubble size distributions in agitated vessel comparison of three experimental techniques, Chem. Eng. Res. Des. 83 (2005) 50–58. doi:10.1205/cherd.04122.

[33] J.C. Lamont, D.S. Scott, An eddy cell model of mass transfer into the surface of a turbulent liquid, AIChE J. 16 (1970) 513–519. doi:10.1002/aic.690160403.

[34] J.J. Heijnen, K. Van't Riet, Mass transfer, mixing and heat transfer phenomena in low viscosity bubble column reactors, Chem. Eng. J. 28 (1984) B21–B42. doi:10.1016/0300-9467(84)85025-X.

[35] C.S. Ho, L. -K Ju, Effects of microorganisms on effective oxygen diffusion coefficients and solubilities in fermentation media, Biotechnol. Bioeng. 32 (1988) 313–325. doi:10.1002/bit.260320308.

[36] M.M.L. de Figueiredo, P.H. Calderbank, The scale-up of aerated mixing vessels for specified oxygen dissolution rates, Chem. Eng. Sci. 34 (1979) 1333–1338. doi:10.1016/0009-2509(79)80025-1.

[37] M.O. Albaek, K. V. Gernaey, M.S. Hansen, S.M. Stocks, Evaluation of the energy efficiency of enzyme fermentation by mechanistic modeling, Biotechnol. Bioeng. 109 (2012) 950–961. doi:10.1002/bit.24364.

[38] P. Biechele, C. Busse, D. Solle, T. Scheper, K. Reardon, Sensor systems for bioprocess monitoring, Eng. Life Sci. 15 (2015) 469–488. doi:10.1002/elsc.201500014.

[39] K. Joeris, J.-G. Frerichs, K. Konstantinov, T. Scheper, In-situ microscopy: Online process monitoring of mammalian cell cultures, Cytotechnology. 38 (2002) 129–134. doi:10.1023/A:1021170502775.

[40] H.K. Larsson, U. Krühne, K. Gernaey, A.L. Skov, Modelling of Mass Transfer Phenomena in Chemical and Biochemical Reactor Systems using Computational Fluid Dynamics, Technical University of Denmark (DTU), 2015.

[41] C. Haringa, A.T. Deshmukh, R.F. Mudde, H.J. Noorman, Euler-Lagrange analysis towards representative down-scaling of a 22 m3 aerobic S. cerevisiae fermentation, Chem. Eng. Sci. 170

(2017) 653–669. doi:10.1016/j.ces.2017.01.014.

[42] M. Laakkonen, P. Moilanen, V. Alopaeus, J. Aittamaa, Modelling local bubble size distributions in agitated vessels, Chem. Eng. Sci. 62 (2007) 721–740. doi:10.1016/j.ces.2006.10.006.

Chapter 5

Measurement and prediction of oxygen gradients in an industrial scale *Trichoderma reesei* fermentation process using computational fluid dynamics

The prediction of oxygen concentrations in an industrial scale fermenter using CFD is illustrated in this chapter. The predicted oxygen concentrations is compared with measurements from an industrial fermentation process. The following chapter is prepared for later publication.

5.1 Abstract

Predicting oxygen gradients require models that account for liquid convection, oxygen mass transfer from the gas phase and kinetic expressions for oxygen uptake. This manuscript utilizes computational fluid dynamics (CFD) in order to account for convection and interfacial mass transfer. The gas-liquid hydrodynamics have been predicted for three 89 m^3 aerobic fermenters operating at the same power input and gas flow rate with varying impeller configuration. The oxygen gradients in the fermenters were simulated assuming an isotropic oxygen uptake rate in the fermenter volume reasoned from a regime analysis. The predicted oxygen concentrations were compared with oxygen concentrations measured in an industrial process with multiple oxygen sensors (but with a slightly different and confidential geometry). The predicted values were in the same range as the measured ones, which implies that CFD is a reasonable tool in assessing oxygen gradients in large scale fermentation processes. The simulations illustrate the importance of convectional flow in bioreactors in order to achieve homogeneous oxygen concentrations, and how different impeller geometries operating at the same power input and gas flow rate affects the observed gradients.

5.2 Nomenclature

Roman	Description	Unit
q_{p_i}	Rate of change of parameter p_i	[-]
p_i	Process parameter	[-]
H	Height of fermenter	[m]
H_T	Total height of fermenter	[m]
D	Impeller diameter	[m]
T	Fermenter diameter	[m]
d_B	Bubble diameter	[m]
P/V	Power per volume	[w/m^3]
k_L	Mass transfer coefficient	[m/s]
D_{O_2}	Diffusion coefficient of oxygen	[m^2/s]
Y_{xo}	Yield of oxygen on biomass	[g/g]
Y_{xs}	Yield of substrate on biomass	[g/g]
C_s	Concentration of limiting carbon source	[g/L]
K_s	Half saturation concentration of limiting carbon source	[g/L]
X	Concentration of biomass	[g/L]
k_La	Volumetric mass transfer coefficient	[1/h]
Greek	**Description**	**Unit**
τ_i	Characteristic time of parameter i	[s]
σ	Surface tension	[N/m]
ρ_L	Density of fermentation broth	[kg/m^3]
μ_G	Viscosity of gas	[Pa s]
μ_a	Apparent viscosity of fermentation broth	[Pa s]
ϵ_L	Turbulence eddy dissipation rate	[m^2/s^3]
ν_l	Kinematic viscosity of fermentation broth	[m^2/s]
μ_{max}	Maximum growth rate	[1/h]
α	Gas hold-up	[-]

Abbreviation	Description
CFD	Computational fluid dynamics
CPU	Central processing unit

DP	Down-pumping impeller
RDT	Rushton disc turbine
PBT	Pitch blade turbine
OUR	Oxygen uptake rate
OTR	Oxygen transfer rate
UP	Up-pumping impeller

5.3 Introduction

A major bottleneck in fermentation process development is a lack of understanding of the changes in hydrodynamics at scale compared to laboratories [1]. This is true for technology transfer to new manufacturing plants, as well as when trying to retrofit existing equipment to new processes. In order to bridge this gap the conditions at scale needs to be described and understood in detail. Sweere et al. (1983) [2] first suggested the concept of trying to keep the end in mind and developing the processes focused on the manufacturing scale. The resulting regime analysis focuses on identifying the rate limiting phenomena occurring at scale. In order to quantify these phenomena a range of characteristic times were established based on the time required to alter a given process parameter beyond a specified threshold. The characteristic time of a given phenomenon is defined as:

$$\tau_i = \frac{\Delta p_i}{q_{p_i}} \tag{5.1}$$

where Δp_i is the specified threshold of process parameter p_i and q_{p_i} is the rate of change of the parameter p_i. This concept is applicable to a range of phenomena in a fermentation process at scale such as glucose uptake, oxygen uptake, heat production and removal and others. The resulting characteristic time is then compared with the mixing time in the fermenter, and if the characteristic time is larger than the mixing time by an order of magnitude one should expect gradients of that process parameter. Screening for rate limiting phenomena in a simple matter is a valuable tool during early process development, but also relies greatly on the assumptions made in determining the rate of change for the process parameter. In order to assess the implication of process gradients on process performance higher level models that are able to reproduce the process gradients are required. This has historically been achieved by discretizing the fermenter volume into a number of well-defined compartments in which the process conditions were considered constant [3]. Compartment based models have been successfully applied to a multitude of fermentation processes at different scales, where convection and hydrodynamics were expected to play a role [4]. Calibrated and validated compartment models are applicable in multiple aspects in bioprocess development such as monitoring and process control. Tuning of inter-compartmental flows is however a complex matter and requires transient tracer response data.

Computational fluid dynamics (CFD) is an often used tool in describing hydrodynamic conditions of bioreactors at different scales and different processes [5–9], avoiding the need for empirical tuning.

The spatial glucose concentration in a pilot scale bubble column has been illustrated for *Saccharomyces cerevisiae* utilizing CFD [8]. Feeding position showcased severe impact on the distribution of glucose in the bubble column, which had a substantial impact on the predicted glucose yield decreasing by 25 % compared to perfect dispersed glucose. Haringa et al. (2017) [6] investigated a 22 m^3 stirred bioreactor using an Euler-Euler approach for the gas-liquid interaction and an Euler-Lagrangian approach for understanding the microorganism behaviour. Similar for both these studies is that they suggest a complex interconnection between gas-liquid hydrodynamics and microbial nutrient uptake.

Measuring oxygen concentrations in multiple positions in industrial scale bioreactors has previously been achieved by moving a sensor vertically up and down during the process [10,11]. This work aims to show how Euler-Euler two-phase CFD simulations can be used in understanding the complex behaviour of industrial fermentation processes. This is achieved by investigating the oxygen gradients in an 89 m^3 agitated fermenter equipped with different impellers. The predicted oxygen gradients are compared with measurements carried out in an industrial fermenter using multiple optical sensors.

5.4 Material and methods

5.4.1 Experimental work

The oxygen gradients were studied in an industrial fed-batch *Trichoderma reesei* fermentation process. The actual operational conditions and real fermenter geometry are not included in this manuscript for proprietary reasons. The oxygen concentration was measured at four locations in the vessel. The measurements were obtained by optical fibres placed at different heights of the fermenter by mounting a custom-made stainless steel bracket on the baffle that allowed the fibres to be fixed in a certain position. The installation on the baffle is shown in Figure 5.1.

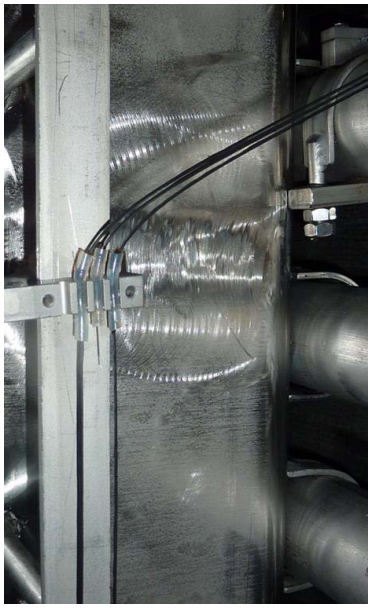

Figure 5.1 - Optical fibres installed along the baffle inside the industrial fermenter. The fibres were protected using a plastic cover when fixed in the bracket.

The optical fibres were chosen because they are flexible and can withstand sterilization, and multiple fibres can be installed in every fitting. A Microx 4 transmitter (PreSens) was used for each optical fibre to log the recorded data with ten second intervals. The sensors were calibrated in water under aeration at 37°C and intense agitation prior to the sterilization. The location of the four optical sensors is given in Table 5.1.

Table 5.1 - Location of optical fibre sensors compared to the liquid height H_T

Sensor	**1**	**2**	**3**	**4**
Height $\left[\frac{H}{H_T}\right]$	0.1	0.375	0.75	0.94

The viscosity of the fermentation broth was sampled in the fermenter and characterized at 25 °C using a controlled strain and stress rheometer (ARG2, TA Instrument, DE) with a 1° gap angle cone-and-plate of 30 mm radius. The shear stress was evaluated at shear rates ranging from 1 1/s to 500 1/s similar to other studies at pilot scale [7,12,13]

5.4.2 Numerical work

5.4.2.1 Fermenter case studies

The numerical simulations in this work are based on three separate cases that resemble the industrial fermenter where the oxygen concentration was measured. The three cases are identical in terms of operational conditions with respect to power input and gas flowrate matching the conditions of the experimental work. The impeller geometry and configuration are different in the three cases in order to demonstrate how the fermenter design affects the oxygen concentration predicted by the CFD simulations. Cooling coils are included in the geometries as stacked tori to simplify the structural meshing surrounding the coils. The geometrical features and impeller configuration of the three cases are summarized in Table 5.2

Table 5.2 - Geometrical features and impeller configuration of the simulated fermenters

Common geometrical features	
H_T	10.4 m
D/T	1/3
H_T/T	3
Sparger	Ring
Liquid volume	89 m^3
Impeller configuration	
Case 1	4 x RDT
Case 2	1 x RDT + 3 x DP-PBT
Case 3	1 x RDT + 3 x UP-A310

The investigated fermenters are geometrically similar to the industrial fermenter, but for proprietary reason not identical. The three geometries are shown in a 3-D rendering in Figure 5.2.

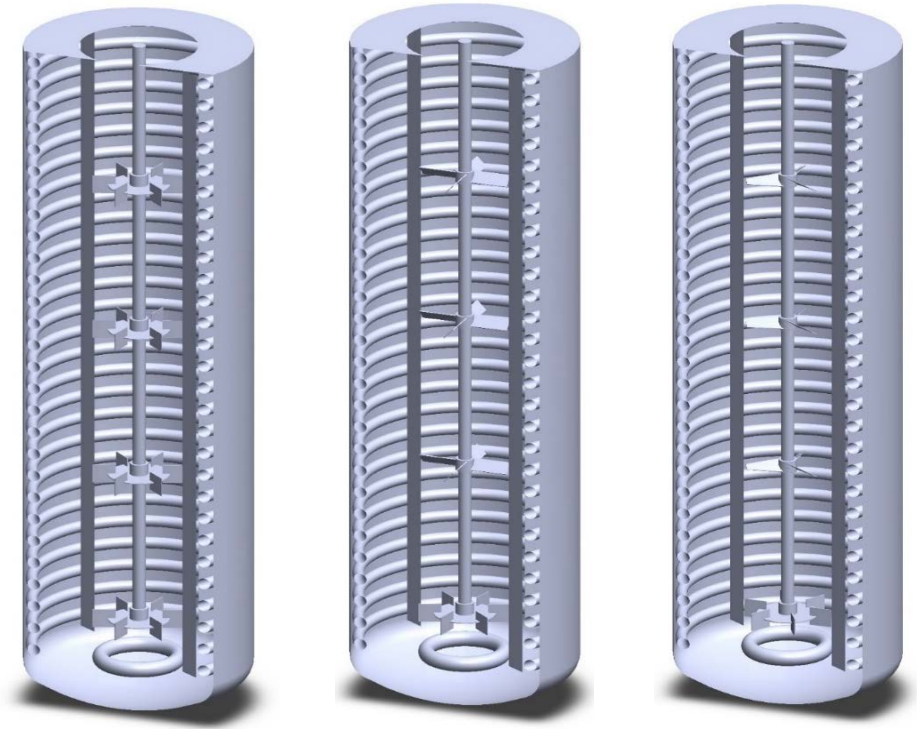

Case 1 **Case 2** **Case 3**

Figure 5.2 – 3-D rendering of the three investigated geometries: Case 1 (Rushton turbines), Case 2 (Down-pumping PBTs) and Case 3 (Up-pumping hydrofoils)

5.4.2.2 Model considerations

Gas-liquid modelling

The CFD simulations were carried out using the commercial code ANSYS CFX 16.1 and meshing of the geometries was done using ANSYS ICEM. The meshing was done predominately as structured mesh and only for the hydrofoils in Case 3, an unstructured mesh was employed. The mesh details are available in the supplementary material. The domain was divided into a rotating domain accounting for the impeller and shaft and a stationary domain containing the baffles and cooling coils. The rotating domain accounted for 27 percent of the total fermenter volume for all cases. A transient frozen rotor or sliding mesh boundary condition was assumed for the rotating domain similar to previous studies [7,14]. A no-slip condition was assumed for the liquid phase and a free slip condition was assumed for the gas phase on all surfaces in the fermenters, and an Euler-Euler approach was applied for the gas

and liquid interactions. The fermenter top was modelled assuming degassing conditions, allowing only the gas phase to escape the flat surface boundary. Turbulence was accounted for using the standard $k-\epsilon$ model. The shear thinning rheology of the fermentation broth was included by applying a power law correlation between viscosity and shear rate, and the consistency and flow index were based on the measured viscosity. The surface tension was assumed to be similar to water and air with a value of 72 mN/m, and was considered to be constant during the fermentation despite of the viscosity increase [15]. A single bubble diameter was assumed in the fermenter, which was chosen based on the correlation of Calderbank (1958) [16].

$$d_B = 2.25 \cdot \frac{\sigma^{0.6}}{\frac{P}{V}^{0.4} \cdot \rho_L^{0.2}} \cdot \alpha^{0.5} \cdot \left(\frac{\mu_G}{\mu_a}\right)^{0.25} \tag{5.2}$$

where σ is the surface tension, α is the gas hold-up, μ_g and μ_a are the gas and liquid viscosity respectively and ρ_L is the broth density. The interfacial area was determined from the local gas hold-up and the bubble size according to Equation (5.2) , and the mass transfer coefficient was calculated according to Lamont and Scott (1970) [17].

$$k_L = 0.4 \cdot \mathcal{D}_{O_2}^{0.5} \cdot \left(\frac{\epsilon_L}{\nu_L}\right)^{0.25} \tag{5.3}$$

where $\mathcal{D}_{O_2}$ is the diffusion constant of oxygen in the broth, ϵ_L is the turbulence eddy dissipation rate in the broth and ν_L is the dynamic viscosity of the broth. The diffusion constant of oxygen in the fermentation broth has been shown to depend on the medium composition and microbial host [18], which for a filamentous fungus was found to be $\mathcal{D}_{O_2} = 0.91 \cdot 10^{-9}$ m²/s.

5.4.2.3 Microbial kinetics

The spatial oxygen concentration in the fermenter is the result of an equilibrium between the convectional flow of oxygen, oxygen transfer from the gas to the liquid phase and uptake by microbial consumption [11]. The consumption of oxygen by the microorganism is generally taken into account by using the kinetic expressions of microbial growth, which consumes oxygen depending on the growth rate. The saturation based Monod kinetics are the simplest and most widely used model to account for the growth rate dependency on the carbon source [19]. Assuming that the oxygen uptake rate (OUR) is only dependent on growth, it can be expressed as shown in Equation (5.4) .

$$OUR = Y_{xo} \cdot X \cdot \frac{\mu_{max} \cdot C_s}{K_s + C_s} \tag{5.4}$$

where Y_{XO} is the yield of oxygen on biomass, X is the concentration of biomass, μ_{max} is the maximum growth rate, K_s is the half saturation constant, and C_s is the concentration of the limiting substrate. Monod kinetics have been coupled with CFD simulations at large scale previously for both bubble columns and stirred fermenters [6,8]. The growth kinetics of a given organism is important to determine whether the carbon source gradients are of interest in the process, and in particular when the organism has high maximum growth rates.

5.5 Regime analysis

The growth kinetics are determined from steady state or accelerated steady state fermentations, which can be time consuming and complicated. Prior to carrying out a full characterization of the growth kinetics it can be beneficial to investigate whether carbon source concentration gradients are to be expected in the fermenter by performing a regime analysis [20]. Assuming the process is limited by the carbon source, the characteristic time of the carbon source consumption can be determined by the biomass growth rate and the average carbon source concentration in the fermenter, as stated in Equation (5.1).

$$\tau_s = \frac{C_{s,ave}}{X \cdot Y_{xs} \cdot \mu_{max} \cdot \frac{C_{s,ave}}{K_s + C_{s,ave}}} \tag{5.5}$$

where $C_{s,ave}$ is the average concentration of the carbon source. The regime analysis allows a comparison of different microorganisms with different growth kinetics in a simple manner. The microbial growth kinetics from literature for four common industrial microbial hosts are summarized in Table 5.3.

Table 5.3 - Growth kinetics of four relevant industrial microorganisms

Organism	Type	Substrate	μ_{max} [1/h]	K_s [g/L]	Y_{xs} [g/g]	Reference
Saccharomyces cerevisiae	Yeast	Glucose	0.49	0.02	0.51	[21]
E. coli	Bacteria	Glucose	0.55	0.05	0.5	[22]
Trichoderma reesei	Fungi	Xylose	0.11	0.48	0.60	[23]
Penicillium chrysogenum	Fungi	Glucose	0.33	0.15	0.56	[24]

Table 5.3 shows how different the key characteristics of the growth kinetics are for different microbial hosts found in literature. The growth kinetics of the different strains vary significantly across the four examples shown in Table 5.3, which means that the rate at which the microbial species will consume

substrate will be very different depending on the strain used in the fermenter. In order to understand the process implication of the differences in growth kinetics a comparison of the characteristic time of carbon source consumption of different microorganisms is shown in Figure 5.3.

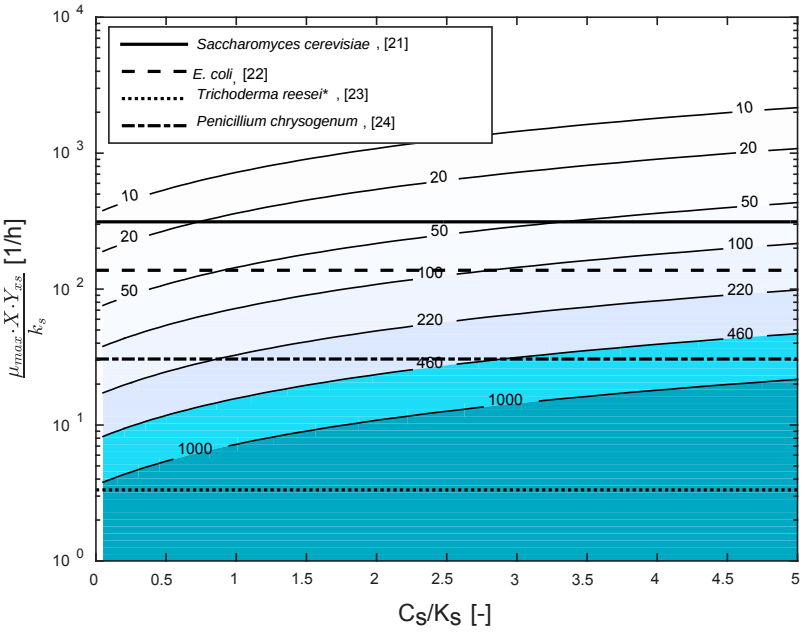

Figure 5.3 – Contour plot of the characteristic time, in seconds, of the carbon source consumption as a function of the maximum substrate uptake rate ($\mu_{max} \cdot X \cdot Y_{XS}$) divided with the half saturation constant and average carbon source concentration divided by the half saturation concentration for five different microbial hosts with $X = 25$ g/L. *The growth kinetics of *Trichoderma reesei* is based on xylose while the rest of the data is based on glucose as carbon source.

Figure 5.3 shows the characteristic time of carbon source consumption of four different microbial hosts used in industrial processes at a biomass concentration of 25 g/L. The characteristic time of carbon source consumption is dramatically different for the different organisms shown and ranges over many orders of magnitude, from 25 to >1000 seconds (*Saccharomyces cerevisiae* to *Trichoderma reesei*) at a carbon source concentration equal to the half saturation concentration ($C_S = K_S$). This massive difference between the various microorganisms reveals, why certain bioprocesses can suffer from carbon source gradients and others will be unaffected at the same operational conditions, just because of their difference in growth kinetics.

Comparing the characteristic times in Figure 5.3 with the expected mixing time in industrial fermenters, in the range of 30 to 200 seconds [26], it is apparent that for *E. coli*, *S. cerevisiae* the

characteristic time of carbon source consumption is similar or smaller than the mixing time. This could lead to carbon source gradients [2]. It is also apparent that the two fungi and in particular *T. reesei* consumes the carbon source slower than the bacteria and yeast, and compared with industrial scale mixing time it should not be expected that carbon source gradients will occur for these organisms assuming a biomass concentration of 25 g/L.

Gradients in carbon source have previously been shown both experimentally and with numerical simulations for *S. cerevisiae* in a 22 m^3 fermenter with glucose measurements at multiple locations operating at 10 g/L of biomass and with a mixing time of approximately 150 seconds [6,27]. *E. coli* is also known to suffer from carbon source gradients at industrial scale (12 m^3) leading to by-product formation and reduced biomass yield [28]. Haringa et al. (2016) [29] investigated *P. chrysogenum* in a 54 m^3 stirred fermenter and showed severe glucose gradients in the fermenter with a mixing time of approximately 308 seconds. The simulated conditions were late in the fermentation resulting in a biomass concentration of 55 g/L, which would correspond to a characteristic time of carbons source consumption of approximately 100 seconds according to Figure 5.3 at $C_S = K_S$, which is less than the mixing time confirming the findings of the regime analysis.

Understanding the characteristic time of carbon source consumption can guide the assumptions made in the CFD simulations regarding the microbial kinetics. For instance for *T. reesei* the characteristic time of carbon consumption is much higher than the expected mixing time, which would allow deducing that the concentration of the carbon source is homogenous in the fermenter. This is in part due to the low maximum growth rate of *T. reesei*, but also the high half saturation constant of this microorganism, which corresponds to a generally slow consumption of carbon source. A constant concentration of carbon source would lead to a constant oxygen uptake rate following Equation (5.4), which excludes the need for kinetic models in order to investigate the oxygen concentration in the fermenter. In view of the latter, the oxygen rate is considered isotropic in the *T. reesei* process in this work.

5.6 Results

5.6.1 Gas – liquid hydrodynamics and mass transfer

The flow patterns of stirred reactors are, besides the operating conditions, affected by the impeller size and configuration as well as internal installations inside the reactor. The liquid flow patterns of large-scale fermenters have been described under non-aerated and aerated conditions based on visual observations [26]. The volumetric mass transfer coefficient is a key process parameter in aerobic fermentations and in particular for viscous fermentation processes [30]. Spatial distribution of the mass transfer coefficient has previously been investigated in stirred systems at pilot scale using compartment models and CFD simulations [7,31,32], and compared with volume average measurements of $k_L a$. Local measurements of $k_L a$ are very complex and rely on assumptions for the hydrodynamics in the liquid phase because the methodology is based on a measurement of the oxygen concentration [33]. The predicted spatial distribution of $k_L a$ and the flow pattern of the three investigated cases is shown in Figure 5.4.

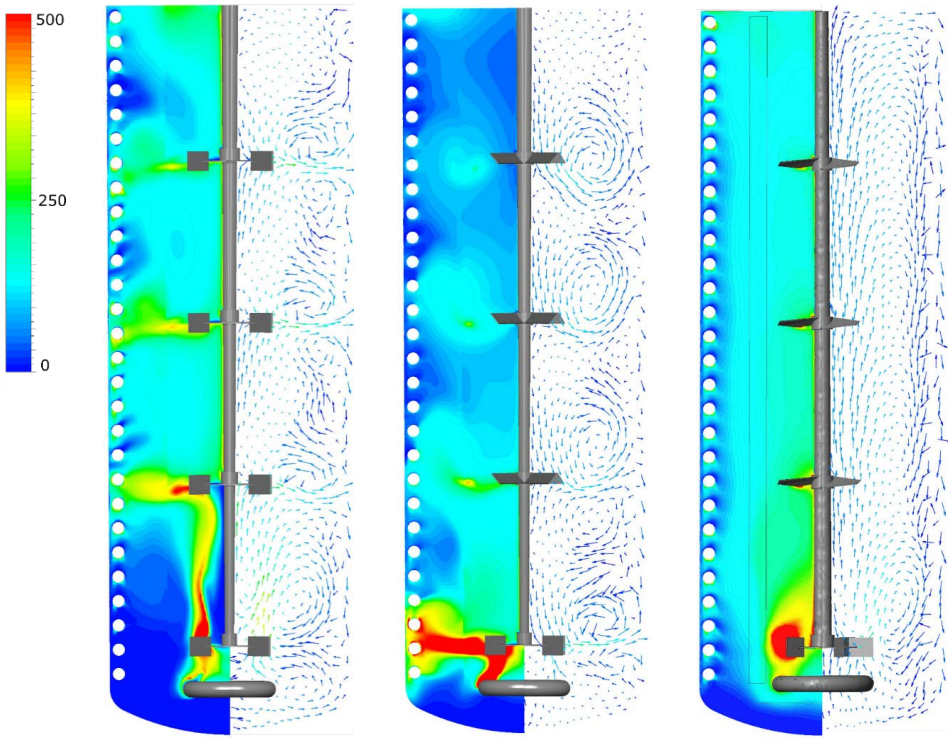

Figure 5.4 – Contour of the volumetric mass transfer (left) and the liquid flow pattern (right) under aerated conditions for the three investigated cases. The same power input and aeration rate is considered for each case.

The flow pattern of the investigated geometries is remarkably different in each case revealing the impact of the impeller geometry. The axial dispersion with recirculation loops from the four Rushton turbines in Case 1 is as expected in such a configuration, but the aeration distorts the recirculation loops corresponding with previously reported numerical predictions in similar geometries [6]. In particular, the flow profile around the bottom impeller in Case 1 differs severely from the expected behavior, which is due to a flooded state as can be seen in Figure 5.4. The flooding predicted by the simulations is in line with empirical correlations for RDTs [34]. The down-pumping PBTs in Case 2 result in strong recirculation loops between the top of the impeller and the walls as a result of the opposite motion of the down-pumping impeller and the upwards moving gas phase. In order to have a reasonable comparison of the three cases the power input was kept constant, which meant that Case

1, because of the larger power number of Rushton turbines, was operated at lower impeller speed causing the flooding in that case. The Rushton turbine in the bottom disperses the air effectively for both Case 2 and 3 because of the higher impeller speed at these conditions. The up-pumping A310 impellers in Case 3 lead to an even flow from the bottom to the top in one large loop. The single loop of liquid motion in Case 3 is contradicting the observations of Vrabel et al. (2000) [26], who suggested that multiple circulation loops should exist in this configuration. The reason for this difference could be that they studied larger up-pumping impellers ($0.61 \cdot T$) than the ones considered in this work, which could explain the difference in flow pattern.

The spatial distribution of $k_L a$ apparent in Figure 5.4 is highly dependent on the configuration of the impellers in the large scale fermenter. The up-pumping motion of the A310 impellers in Case 3 gives rise to an even distribution of the spatial volumetric mass transfer coefficient, and is in great contrast to the down-pumping PBT investigated in Case 2. The flooded condition of the bottom impeller in Case 1 leads to a situation where a large part of the volume is without any gas and subsequently without interfacial surface area, which greatly affects the $k_L a$ in the bottom of the fermenter. The gas hold-up values are not included for proprietary reasons, but were found to be similar to previously reported values for large scale bioreactors [6,35].

5.6.1.1 Mixing time

The mixing time has been considered a valuable process metric over the past decades in relation to the quantification of mixing performance of bioreactors of different size and configuration [34]. The mixing time of stirred bioreactors is dependent on the flow pattern inside the bioreactor and the scale of the bioreactor, making it an important metric for process scale-up. The mixing time is in this work defined as the time required to reach 95 % of the homogeneous concentration following a pulse addition of tracer. The predicted mixing time values for the three cases are shown in Table 5.4.

Table 5.4 - Predicted mixing time of each investigated cases. The mixing time is defined, as the time required for achieving 95 % homogeneity.

Case	τ_{mix} [s]
1	191
2	172
3	30.1

Table 5.4 illustrates the impact of impeller geometry at constant power input and gas flow rate in large scale aerated bioreactors. The compartmentalizing configuration of Case 1 and Case 2 results in mixing times around 3 minutes, which is 6 times the mixing time of the up-pumping A310 configuration of Case 3. This severe difference is previously described by Vrabel et al. (2000) [26], who investigated mixing times in 12 and 30 m^3 bioreactors experimentally and found similar trends.

5.6.2 Oxygen gradients

In order to evaluate the performance of each geometry, the mass transfer capabilities and hydrodynamics should be combined with oxygen uptake and oxygen transfer, enabling the prediction of the oxygen gradients. This approach is similar to recent studies in industrial bubble columns [8]. The oxygen transfer rate and resulting oxygen concentration are shown in Figure 5.5

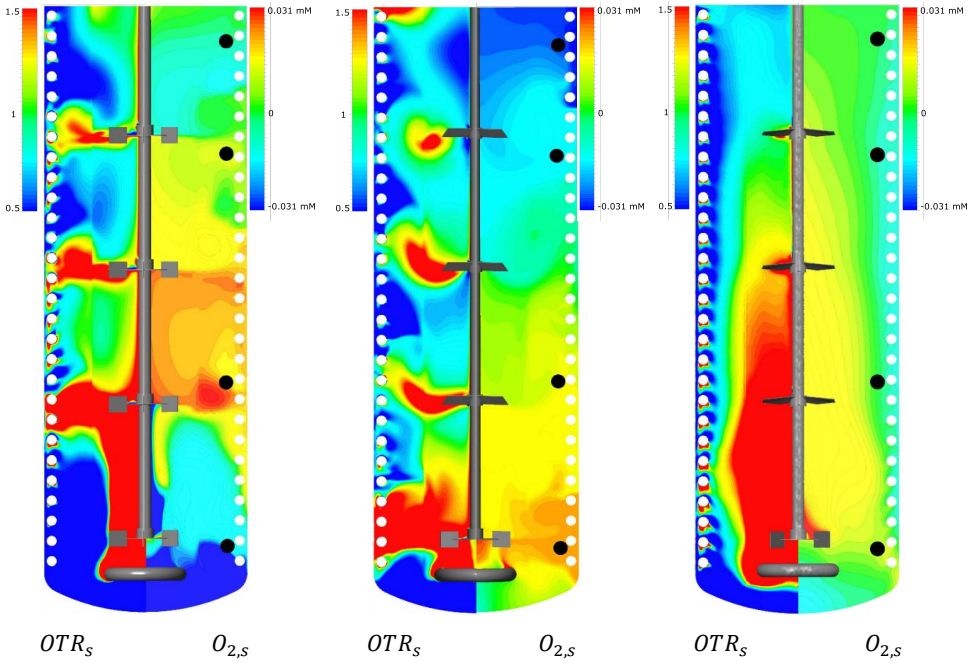

Figure 5.5 - Normalized oxygen transfer rate (OTR_S) and normalized oxygen concentration ($O_{2,S}$) contour plot for each geometry working at identical power input and gas flow rate. The oxygen transfer rate and oxygen concentration are scaled by their volumetric average for properitary reasons. The black dots indicate the location of the optical oxygen sensors.

Figure 5.5 displays the clear influence of convection in the oxygen concentration profiles when assuming an isotropic oxygen uptake rate. Omitting the convectional flow in the liquid phase would

result in a concentration profile proportional to the OTR profile, which is far from the predicted scenario in Figure 5.5. The oxygen concentration profile of Case 1 illustrates the compartmentalization produced by multiple Rushton turbines in particular for the top three impellers. This compartmentalization from multiple Rushton turbines confirms the results of numerical simulations of similar reactors [6]. The flow patterns predicted by the down-pumping PBT's in Case 2 gives rise to some compartmentalization as well, but not to the same extent as found in Case 1. The expected convectional performance of Case 3 from Table 5.4 is confirmed in Figure 5.5 resulting in small gradients in oxygen concentration compared to the other cases, and indicates that the up-pumping configuration has substantial benefits in terms of liquid blending. The oxygen concentration generally decreases towards the top of the reactor for all cases, which is caused by the decrease in saturation concentration resulting from a change in hydrostatic pressure towards the top of the fermenter. The drastic changes in oxygen concentration near the RDT predicted for Case 1 are similar to the empirical findings of Oosterhuis et al. (1983) [36] in a 25 m^3 bioreactor with RDT turbines.

5.6.3 Comparison of experimental and simulated oxygen concentrations

In order to evaluate the assumptions associated with the gas-liquid hydrodynamics and microbial kinetics the predicted oxygen concentrations are evaluated along the baffle in the three simulated geometries and compared with the findings from the measurements in the industrial bioreactor. The normalized oxygen concentrations of the three simulated cases and the normalized measurements are shown in Figure 5.6.

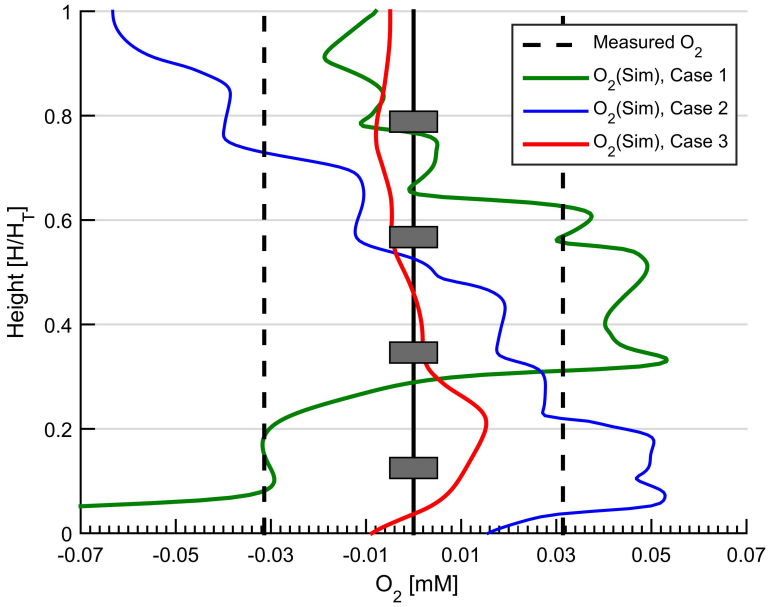

Figure 5.6 - Normalized oxygen concentration evaluated along the baffle inside the fermenter for the three simulated cases (solid line) and the range of oxygen concentration ($\pm 0.031\ mM$) measured at full scale (dashed lines). The grey bars indicate the location of the impellers in the simulated fermenters.

Figure 5.6 shows the effect of impeller configuration on the oxygen concentration from top to bottom of the fermenter evaluated along the baffle. The oxygen concentration in Case 1 is -0.07 mM below the average concentration in the bottom of the tank, and reaches the highest concentration of 0.055 mM above the average oxygen concentration between 30 % and 50 % of the total height. The highest oxygen concentration, 0.055 mM higher than the average concentration, in Case 2 is observed in the bottom of the fermenter between 0.05 and 0.2 of the total height and the lowest concentration is calculated to be a the very top of the fermenter. The oxygen concentration steadily decreases from

the 20 % of the fermenter height towards the top. The oxygen concentration in Case 3 has a maximum, similar to Case 2, around 20 % of the fermenter height with a value of 0.015 mM above the average concentration and the lowest concentration is observed at 80 % of the fermenter height. The range of measured oxygen concentration was found to be $\pm$ 0.031 mM of the average oxygen concentration in the fermenter. The measured data is reported as the span of oxygen concentrations because of the geometrical differences between the simulated geometry and the geometry of the industrial fermenter. The geometrical differences makes a comparison of the spatial concentration of oxygen in the simulated and measured case misleading. In order to make a comparison of spatial oxygen concentrations the geometries must be the same. The range of measured oxygen concentrations is similar to the predicted range, and indicates that the complex CFD simulations are able to reproduce the expected range of oxygen gradients. Additionally, the three investigated cases show how important liquid convection is in mitigating gradients in a large scale fermenter operating at the same power input and gas flow rate. The concentration gradient of the up-pumping A310 configuration of Case 3 is minor in comparison with the other cases, which supports the conclusions of the mixing time study of Table 5.4. The steep increase of the oxygen concentration close to the second Rushton turbine in Case 1 and the bottom RDT in Case 2 is comparable with findings of Oosterhuis et al (1983) [36], which further supports the confidence in the CFD simulations. In the three investigated cases, the oxygen gradient is merely a result of difference in the oxygen transfer rate, due to hydrostatic pressure and spatial $k_L a$ distribution, and liquid convection, due to the assumption a of spatially constant oxygen uptake rate. This assumption appears to be valid for the *T. reesei* process, since the measured oxygen concentration is similar to the predicted values.

The simulation study presented in Figure 5.5 and Figure 5.6 illustrates that the blending capabilities of a bioreactor are equally important as the oxygen transfer capabilities if oxygen gradients are a concern. In particular the axial convection is important, which can be improved considerably by introducing an up-pumping impeller above the bottom RDT following previous experimental findings in large scale bioreactors [26].

Two-phase CFD simulations on the scale of industrial size fermenters remain a computationally heavy effort even with improvements in parallel computing and CPU efficiency. Simplifications in the mechanisms involved in the simulations can hence be highly valuable and enable characterization of problems that would otherwise be unfeasible to solve in a time frame of weeks or even months. In this context, regime analysis plays an important role in enabling the numerical simulation of industrial processes. This has been shown by Haringa et al (2017) [6], who omitted the influence of oxygen from

simulations of an aerobic *S. cerevisiae* fermentation because it would not play a role under the investigated process conditions, and only focused on the hydrodynamics of the gas-liquid system and the effect of glucose.

An evaluation of the required complexity of the involved phenomena is essential if numerical analysis of industrial scale processes is to become a standard procedure. In this context, a simple regime analysis could serve as of part of a systematic investigation of the required complexity required to reproduce a given process behaviour.

5.7 Conclusion

The gas-liquid hydrodynamics of three 89 m^3 fermenters have been investigated using computational fluid dynamics. The simulated flow profile and spatial $k_L a$ distribution revealed that the impeller configurations influence the bioreactor hydrodynamics significantly when operating at the same power input and gas flow rate. Flooding was observed for Case 1 (4 x RDTs) due to the lower impeller speed in order to obtain the same power input as the other cases. A study of the mixing time revealed large variation between Case 3 (RDT + 3 x UP-A310) and the other cases, which is explained by the difference in flow profile of the up-pumping impellers in Case 3 and the down-pumping or radial impellers of Case 2 (RDT + 3 x DP-PBT) and Case 1 respectively.

The oxygen gradient in the three fermenters was predicted assuming an isotropic oxygen uptake rate, and revealed a large influence of liquid convection inside the fermenter. Comparing the oxygen gradient with measured values of a geometrically similar industrial fermenter confirmed that the predicted oxygen gradient was in the same range as the measured values.

The presented study in this manuscript indicates that commercial CFD software is able to predict the range of oxygen gradients in a viscous *T. reesei* fermentation at industrial conditions. Regime analysis can be utilized as a simplification tool in order to avoid implementation of the unnecessary additional complexity of microbial growth kinetics, which is not relevant if the mixing intensity is sufficient compared to the carbon uptake rate.

5.8 Acknowledgements

The authors would like to acknowledge Lisa Mears and Daniela Quintanilla for their work regarding sampling of the fermentations and analysis of in particular broth viscosity. This project has received funding from Novozymes A/S, the Technical University of Denmark (DTU) and Innovation Fund Denmark in the frame of the Strategic Research Center BIOPRO2 (BIObased PROduction: TOwards the next generation of optimized and sustainable processes).

5.9 References

[1] H. Noorman, An industrial perspective on bioreactor scale-down: What we can learn from combined large-scale bioprocess and model fluid studies, Biotechnol. J. 6 (2011) 934–943. doi:10.1002/biot.201000406.

[2] A.P.J. Sweere, Regime analysis and scale-down: tools to investigate the performance of bioreactors, 9 (1987) 386–398.

[3] J. Zahradník, R. Mann, M. Fialová, D. Vlaev, S.D. Vlaev, V. Lossev, P. Seichter, A networks-of-zones analysis of mixing and mass transfer in three industrial bioreactors, Chem. Eng. Sci. 56 (2001) 485–492. doi:10.1016/S0009-2509(00)00252-9.

[4] P. Vrábel, R.G.J.M. Van der Lans, F.N. Van der Schot, K.C. a M. Luyben, B. Xu, S.O. Enfors, CMA: Integration of fluid dynamics and microbial kinetics in modelling of large-scale fermentations, Chem. Eng. J. 84 (2001) 463–474. doi:10.1016/S1385-8947(00)00271-0.

[5] J. Morchain, J.C. Gabelle, A. Cockx, A coupled population balance model and CFD approach for the simulation of mixing issues in lab-scale and industrial bioreactors, AIChE J. 60 (2014) 27–40. doi:10.1002/aic.14238.

[6] C. Haringa, A.T. Deshmukh, R.F. Mudde, H.J. Noorman, Euler-Lagrange analysis towards representative down-scaling of a 22 m3 aerobic S. cerevisiae fermentation, Chem. Eng. Sci. 170 (2017) 653–669. doi:10.1016/j.ces.2017.01.014.

[7] C. Bach, J. Yang, H. Larsson, S.M. Stocks, K. V Gernaey, M.O. Albaek, U. Krühne, Evaluation of mixing and mass transfer in a stirred pilot scale bioreactor utilizing CFD, Chem. Eng. Sci. 171 (2017) 19–26. doi:10.1016/j.ces.2017.05.001.

[8] D.D. McClure, J.M. Kavanagh, D.F. Fletcher, G.W. Barton, Characterizing bubble column bioreactor performance using computational fluid dynamics, Chem. Eng. Sci. 144 (2016) 58–74. doi:10.1016/j.ces.2016.01.016.

[9] a Lapin, C. Maul, K. Junghans, a Lu, Industrial-scale bubble column reactors: gas}liquid #ow and chemical reaction, Chem. Eng. Sci. 56 (2001) 239–246.

[10] R. Manfredini, V. Cavallera, L. Marini, G. Donati, Mixing and oxygen-transfer in conventional stirred fermenters, Biotechnol. Bioeng. 25 (1983) 3115–3131. doi:10.1002/bit.260251224.

[11] N.M. Oosterhuis, N.W. Kossen, Dissolved oxygen concentration profiles in a production-scale bioreactor., Biotechnol. Bioeng. 26 (1984) 546–550. doi:10.1002/bit.260260522.

[12] M.O. Albæk, Evaluation of the efficiency of alternative enzyme production technologies, (2012).

[13] L. Mears, S.M. Stocks, M.O. Albaek, G. Sin, K. V. Gernaey, Mechanistic Fermentation Models for Process Design, Monitoring, and Control, Trends Biotechnol. 35 (2017) 914–924. doi:10.1016/J.TIBTECH.2017.07.002.

[14] J.C. Gabelle, F. Augier, a. Carvalho, R. Rousset, J. Morchain, Effect of tank size on k La and mixing time in aerated stirred reactors with non-newtonian fluids, Can. J. Chem. Eng. 89 (2011) 1139–1153. doi:10.1002/cjce.20571.

[15] F.H. Deindoerfer, E.L. Gaden, Effects of liquid physical properties on oxygen transfer in penicillin

fermentation., Appl. Microbiol. 3 (1955) 253–7. http://www.pubmedcentral.nih.gov/articlerender.fcgi?artid=1057115&tool=pmcentrez&rendertype=abstract.

[16] P.H. Calderbank, Physical rate processes in industrial fermentation Part I: The interfacial area in gas-liquid contacting with mechanical agitation, Chem. Eng. Res. Des. (1958).

[17] J.C. Lamont, D.S. Scott, An eddy cell model of mass transfer into the surface of a turbulent liquid, AIChE J. 16 (1970) 513–519. doi:10.1002/aic.690160403.

[18] C.S. Ho, L. -K Ju, Effects of microorganisms on effective oxygen diffusion coefficients and solubilities in fermentation media, Biotechnol. Bioeng. 32 (1988) 313–325. doi:10.1002/bit.260320308.

[19] J. Monod, The Growth of Bacterial Cultures, Annu. Rev. Microbiol. 3 (1949) 371–394. doi:10.1146/annurev.mi.03.100149.002103.

[20] A.P.J. Sweere, K.C.A.M. Luyben, N.W.F. Kossen, Regime analysis and scale-down: Tools to investigate the performance of bioreactors, Enzyme Microb. Technol. 9 (1987) 386–398. doi:10.1016/0141-0229(87)90133-5.

[21] E. Postma, W. Alexander Scheffers, J.P. Van Dijken, Kinetics of growth and glucose transport in glucose-limited chemostat cultures ofSaccharomyces cerevisiae CBS 8066, Yeast. 5 (1989) 159–165. doi:10.1002/yea.320050305.

[22] B. Xu, M. Jahic, S.-O. Enfors, Modeling of Overflow Metabolism in Batch and Fed-Batch Cultures of Escherichia coli, Biotechnol. Prog. 15 (1999) 81–90. doi:10.1021/bp9801087.

[23] D.W. Schafner, R.T. Toledo, Cellulase production in continuous culture byTrichoderma reesei on xylose-based media, Biotechnol. Bioeng. 39 (1992) 865–869. doi:10.1002/bit.260390808.

[24] R.D. Douma, P.J.T. Verheijen, W.T.A.M. de Laat, J.J. Heijnen, W.M. van Gulik, Dynamic gene expression regulation model for growth and penicillin production in Penicillium chrysogenum, Biotechnol. Bioeng. 106 (2010) 608–618. doi:10.1002/bit.22689.

[25] J. Villadsen, J. Nielsen, G. Lidén, Bioreaction Engineering Principles, 3rd ed., Springer, 2011. doi:10.1007/978-1-4419-9688-6.

[26] P. Vrábel, R.G.J.M. Van Der Lans, K.C.A.M. Luyben, L. Boon, A.W. Nienow, Mixing in large-scale vessels stirred with multiple radial or radial and axial up-pumping impellers: Modelling and measurements, Chem. Eng. Sci. 55 (2000) 5881–5896. doi:10.1016/S0009-2509(00)00175-5.

[27] G. Larsson, M. Törnkvist, E. Ståhl Wernersson, C. Trägårdh, H. Noorman, S.O. Enfors, Substrate gradients in bioreactors: Origin and consequences, Bioprocess Eng. 14 (1996) 281–289. doi:10.1007/s004490050218.

[28] F. Bylund, E. Collet, S.-O. Enfors, G. Larsson, Substrate gradient formation in the large-scale bioreactor lowers cell yield and increases by-product formation, Bioprocess Eng. 18 (1998) 171–180. doi:10.1007/s004490050427.

[29] C. Haringa, W. Tang, A.T. Deshmukh, J. Xia, M. Reuss, J.J. Heijnen, R.F. Mudde, H.J. Noorman, Euler-Lagrange computational fluid dynamics for (bio)reactor scale down: An analysis of organism lifelines, Eng. Life Sci. 16 (2016) 652–663. doi:10.1002/elsc.201600061.

[30] S.M. Stocks, Industrial enzyme production for the food and beverage industries : process scale up and scale down, in: Microb. Prod. Food Ingredients, Enzym. Nutraceuticals, 2013: p. 656. doi:10.1533/9780857093547.1.144.

[31] M. Laakkonen, P. Moilanen, V. Alopaeus, J. Aittamaa, Modelling Local Gas–Liquid Mass Transfer in Agitated Vessels, Chem. Eng. Res. Des. 85 (2007) 665–675. doi:10.1205/cherd06171.

[32] P. Moilanen, M. Laakkonen, J. Aittamaa, Modelling fermenters with CFD, Comput. Aided Chem. Eng. 20 (2005) 709–714. doi:10.1016/S1570-7946(05)80240-8.

[33] M. Fujasová, V. Linek, T. Moucha, Mass transfer correlations for multiple-impeller gas-liquid contactors. Analysis of the effect of axial dispersion in gas and liquid phases on “local” kL a values measured by the dynamic pressure method in individual stages of the vessel, Chem. Eng. Sci. 62 (2007) 1650–1669. doi:10.1016/j.ces.2006.12.003.

[34] A.W. Nienow, Hydrodynamics of Stirred Bioreactors, Appl. Mech. Rev. 51 (1998) 3. doi:10.1115/1.3098990.

[35] P. Vrábel, R.G.J.M. Van der Lans, Y.Q. Cui, K.C.A.M. Luyben, Compartment Model Approach: Mixing in Large Scale Aerated Reactors with Multiple Impellers, Chem. Eng. Res. Des. 77 (1999) 291–302. doi:10.1205/026387699526223.

[36] N.M.G. Oosterhuis, N.W.F. Kossen, Oxygen transfer in a production scale bioreactor, Chem. Eng. Res. Des. 61 (1983) 308–312.

Chapter 6

Hypothesis driven compartment model for stirred bioreactors utilizing computational fluid dynamics and multiple pH sensors

In this chapter, a novel methodology of scaling down numerical models of hydrodynamics in bioreactors is presented. The methodology is applied to a pilot fermenter as a case study.

This chapter is submitted as a research article for publication in a scientific journal and is only formatted to match the thesis layout. The article is authored by Anders Nørregaard (Novo Nordisk A/S)*, Christian Bach (PROSYS, DTU) *, Ulrich Krühne (PROSYS, DTU), Ulrik Borbjerg (Novo Nordisk A/S) & Krist V. Gernaey (PROSYS, DTU)

*Both authors contributed equally to the work.

6.1 Abstract

The ability to understand and predict mixing behaviour in stirred bioreactors by the use of mathematical models is an effective strategy to improve or ensure performance of the process. Historically compartment models have been developed to facilitate the prediction of the hydrodynamics and in the last decade, computational fluid dynamics (CFD) has become the standard tool to assess this in detail. Despite the development of computational capacity CFD simulations of bioreactors remains a challenge at industrial scale where the need for simplified models is apparent due to scale and complex phenomena occurring at scale. The combination of CFD and compartment models has been investigated in this work using a pilot scale stirred bioreactor equipped with three Rushton disc turbines and multiple pH sensors as case study. A hypothesis driven compartmentalization strategy consisting of five subsequent steps has been developed and applied to the pilot scale stirred bioreactor. The compartmentalization resulted in 56 compartments with unidirectional flow between adjacent compartments. The performance of the methodology was evaluated against a data driven compartment approach and the full CFD simulation in the ability to recreate transient tracer profiles following top and bottom feeding of tracer. The data driven compartment model proved to be the most accurate of the three investigated methods, while the hypothesis driven compartment method had a 10-12 % higher error on prediction. The developed methodology should be considered a viable alternative to conventional CFD methods when complex phenomena such as multidimensional populations balance modelling is of interest.

6.2 Nomenclature

Roman	Description	Unit
C	Scaled tracer concentration	[-]
EF	Exchange flow	[kg/s]
F	Mass flow rate	[kg/s]
FC	Circumferential flow rate	[kg/s]
FH	Horizontal flow rate	[kg/s]
FV	Vertical mass flow rate	[kg/s]
H	Vertical division	[m]
R	Radial division	[m]
t	Time	[s]
v_p	Liquid velocity	[m/s]
V	Compartment volume	[m^3]
W	Circumferential division	[°]
x_1	Dimension	[m]
x_2	Dimension	[m]
ρ	Liquid density	[kg/m^3]
Indices		
i	Vertical position	
j	Horizontal position	
k	Wedge position	
f	Feed compartment	

Abbreviations	Description
CFD	Computational fluid dynamics
RDT	Rushton disc turbine
RANS	Reynolds average Navier-Stoke
RMSE	Root mean square error

6.3 Introduction

Mixing characteristics in stirred bioreactors is a topic that has been studied intensely for decades [1]. The knowledge of mixing in a biotechnological process can be useful in design, scaling and troubleshooting of the process. The mixing dynamics can also be coupled to the biochemical reactions in the vessel as well as gas-liquid mass transfer to simulate the effects of substrate gradients on the process [2]. Mixing is usually quantified through tracer experiments including but not limited to pulses of acid/base, salt, radioactive elements or liquids of different temperature. The pulses are measured with one or more sensors inside the vessel to quantify the distribution of the tracer over time [3]. In particular for investigation in smaller vessels (<1 m^3) the response of the sensor becomes an important factor, since the measurement delay can be of the same order of magnitude as the tracer dynamics [4,5]. Design and completion of these experimental investigations is time consuming and requires a meticulous choice of sensors and equipment. Mathematical models can be applied to facilitate the understanding of the phenomena involved in mixing of stirred bioreactors, which leverages the experimental efforts to increase their impact.

Compartment models, sometimes named Network of Zones models, are based on well mixed tanks in series have been used as a model framework for modelling hydrodynamics [6,7]. These methods are suitable when multiple sensors are used in the vessel to determine the tracer concentration profiles at different locations in the vessel, but when the number of compartments in the models starts to increase to a number higher than the number of sensors, a problem of parameter identifiability can arise. Computational fluid dynamics (CFD) is an alternative model approach used to simulate hydrodynamic flows in bioreactors [8,9]. These models show an interesting potential, but are complicated and require considerable computational resources to work, especially when the CFD model is coupled to reaction and mass transfer. In the last decade mixing studies have started integrating the knowledge acquired from CFD simulations with the limited computational effort of compartment models[10–12].

The scope of this article is to compare a CFD model with experimental data acquired in a pilot scale bioreactor at Novo Nordisk A/S. The results from the CFD model are then used to produce a hypothesis driven compartment model. Finally, the investigated models are benchmarked against experimental data.

6.4 Materials and methods

Mixing behaviour was quantified using acid and base tracer experiments in a linear pH buffer solution. The medium is composed of 2 mM succinic acid and 2 mM malonic acid as proposed by Poulsen and Iversen [13], which produces a linear pH response in a range from 3 to 6 pH units. All experiments were conducted within the linear pH range. Alternating pulses of approximately 46 %wt H_2SO_4 or KOH solution were used to produce tracer response curves, measured with 5 pH electrodes of the model: CPS471D-7211 (Endress + Hauser). The pH sensors were installed on a steel beam attached to a cooling coil in the bioreactor. The sensors were positioned directly between two baffles. Acid and base pulses were in turn added at three different heights using a system of silicone tubes fastened to the baffle and entering the vessel through the top. The dosing and sensor positions are shown in Figure 1 b). A peristatic pump model: 323S (Watson Marlow) was used to pump pH tracer solution into the vessel over a period of approximately 3 seconds. pH was logged with a central data logger model: MW100 (Yokogawa) for all pH electrodes. All experiments were done in quadruplicates and were carried out at a single filling level covering all three Rushton disc turbines (RDTs) in the bioreactor. Three different agitation speeds were investigated. Even though the mixing models investigated in this work, are aimed at aerobic fermentation processes, this article only deals with non-aerated mixing. This is done to limit the complexity of the data set and the simulations. The combined experimental work entails 36 tracer additions by combining three mixing intensity conditions with three dosing points and four repetitions for each condition. The individual mixing profiles are normalized from 0 to 1, where 0 represents the start pH in the vessel before the pulse is added and 1 the final pH after homogenization.

Figure 6.1 a) displays an example of 4 repeated mixing tracer profiles with top dosing.

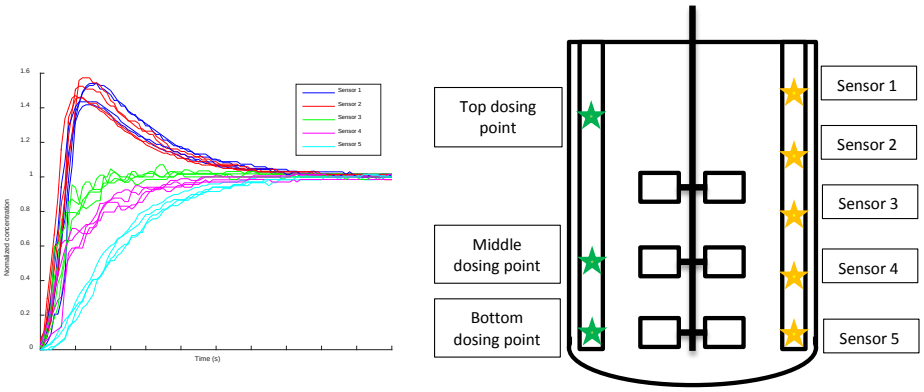

a) b)

Figure 6.1 - a) Example of a normalized mixing profile measured with 5 pH electrodes. The time axis is normalized due to confidentiality. b) Diagram of the bioreactor used as experimental basis for the work. The vessel is equipped with three Rushton disc turbine

6.4.1 4+1 compartment model

It has long been established that RDT impellers have a tendency of producing horizontal separation of the liquid flow in a bioreactor. Thus a 3 x RDT configuration can roughly be assumed to divide the vessel into four well mixed zones [14]. With this in mind, a four compartment model was used as the simplest reference model for this study. The model is highly data driven and thus requires large amounts of experimental data. It is also the model which requires the least amount of calculations and iteration to work properly, i.e. solution of this model is relatively straightforward. The model geometry was taken directly from the vessel dimensions and impeller positions, while four exchange flows between compartments are estimated with an optimization algorithm (fmincon, matlab R2015b) to fit the experimental data. A fifth pseudo compartment was added to the model to help simulate the addition of the tracer, and this is done to improve the model ability to mimic the process of the pH tracer being mixed into the bulk flow in the vessel. The feeding compartment is assumed to be small (0.1 litres) and coupled directly to the compartment closest to the dosing point with an exchange flow. The 4+1 compartment model is described in detail in Appendix 1. The parameter estimation was carried out with a single set of exchange flows to fit both bottom and top dosing, in order to get a robust model.

6.4.2 CFD flow characterization

A CFD simulation was made for each of the different agitation speeds using the commercial CFD software ANSYS CFX version 16.1. The simulation was carried out as a single phase RANS simulation, where turbulence was accounted for using the standard $\kappa - \epsilon$ model. The impeller motion was

captured using a transient frozen rotor also known as sliding mesh boundary condition, which has proven applicable for mixing time determination in previous studies [11,15]. Discretization of the domain was done using a hexahedral mesh configured in ICEM CFD 16, and consisted of 734,000 elements in total. The full geometry was simulated in order to capture the spatial effects of measuring and adding tracer in different locations in the vessel. A scalar was used to determine tracer dissipation and simulate the addition of acid or base in the solution. The tracer addition was based on an assumption of an ideal pulse over three seconds.

6.4.3 Hypothesis driven 56+1 model

The novel hypothesis driven compartment model developed in this work relies on evaluating circumferential, axial and radial flow at different locations in the vessel. The compartments are defined as volumes with unidirectional flow on each surface in either the radial, axial or circumferential direction. This definition limits the degrees of freedom of the generated compartments because each compartment must have two surfaces in the axial, radial and circumferential direction. Expanding this definition to other coordinate systems is not covered in this work, and is subject to further research. The description of the methodology is carried out using the investigated pilot scale vessel as a case study, and every step of the method will be explained in more detail in relation to this case study. The general workflow of the methodology is shown in Figure 6.2.

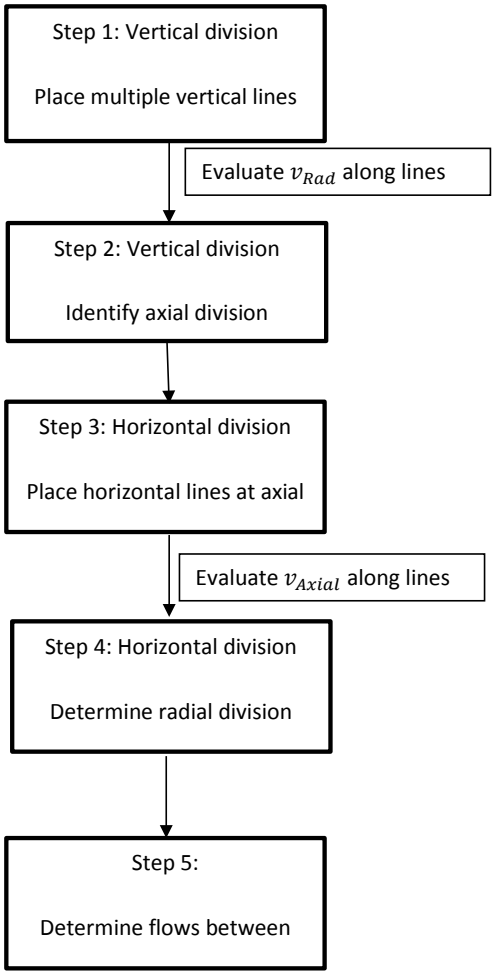

Figure 6.2 - Schematic workflow of compartment methodology, which enables identification of individual compartments in a bioreactor

6.4.3.1Step 1 – Vertical division

The first step in the methodology entails the placement of multiple vertical lines in the geometry of the CFD model. The vertical lines are placed in multiple locations as shown in Figure 6.3 a) to ensure that the vertical division is as global as possible. Furthermore having multiple sample points helps to determine the spatial uncertainty of the compartments.

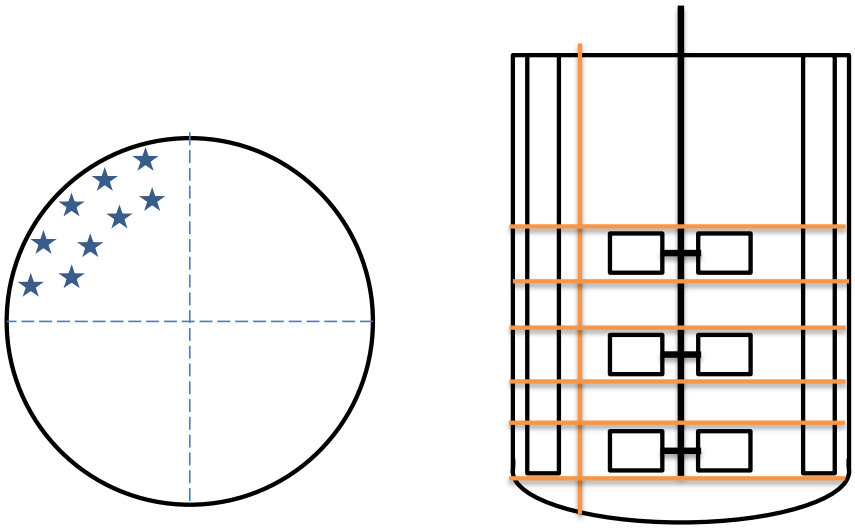

Figure 6.3 - a) The top down look into the bioreactor. Blue stars indicate where vertical lines have been placed to determine horizontal flow profiles using evaluation of flows. b) The cross sectional view of the vertical and horizontal lines, which are used in the method to identify the location of each compartment.

6.4.3.2 Step 2 - Vertical division

The radial flow velocity is evaluated along the vertical lines in the bioreactor. The sign of the radial velocity will indicate whether the bulk flow is directed towards the wall of the bioreactor or towards the impeller shaft. Vertical division of the vessel is located at the height of every change in radial flow direction. Figure 6.4 depicts a common radial velocity profile resulting from this analysis.

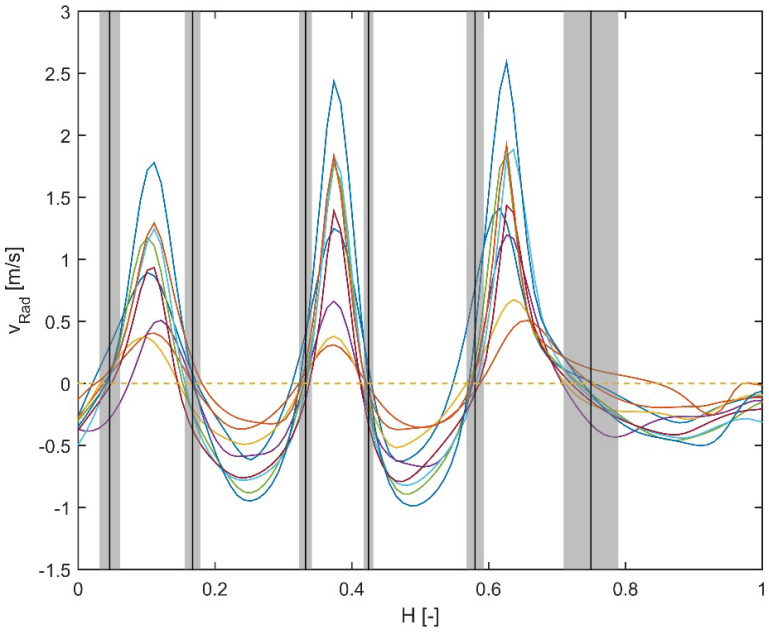

Figure 6.4 - Radial flow profiles at medium agitation speed as a function of dimensionless height evaluated along the vertical lines identified in the first step of the methodology. The black lines indicate the location of vertical division and the grey area indicates the standard deviation from the mean division height. The dashed line indicates the turning point from flow towards the wall and towards the shaft.

The collected flow profiles shown in Figure 4 indicate that despite the varying positions of the vertical lines from Step 1, general trends are observable. The effect of the impeller action is apparent in the peaks of radial velocity for all impeller positions and investigated flow lines. Determination of the axial compartment division is carried out by identifying the reactor height where radial flow alternates from moving towards the reactor wall to moving towards the impeller shaft or the other way around, as indicated by vertical black lines in Figure 6.4. This results in six vertical divisions for the investigated geometry yielding 7 compartments in the height of the vessel.

6.4.3.3 Step 3 – Radial division

Based on the axial divisions identified in Step 2 horizontal lines, as shown in Figure 6.3 b), are placed at each height from the centre of the reactor to the wall.

6.4.3.4 Step 4 – Radial division

In a similar manner as in step 1 to 3, the radial division of compartments are identified by evaluating the axial flow velocity along the horizontal lines resulting from Step 3 in the methodology. The axial velocity profiles along the six horizontal lines are shown in Figure 6.5.

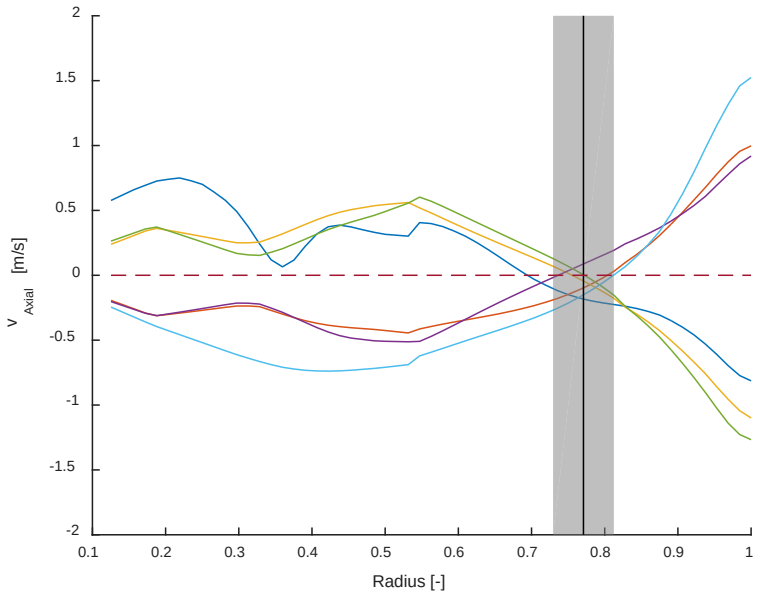

Figure 6.5 - Axial velocity profiles as a function of scaled reactor radius for the six horizontal lines identified in Step 3. The vertical black line indicates the mean radius of flow direction change and the grey area indicates the standard deviation from the mean.

The six velocity profiles shown in Figure 6.5 can be grouped in two, where the first group represents compartments with axial positive (upward) flow close to the impeller and the second group consists of axial negative (downward) flow close to the impeller. The mean intersection radius is used as the definition of the horizontal division of the vessel.

6.4.3.5 Circumferential division

In order to simulate the clockwise mixing of liquid when seen from above, the vessel is divided in four wedges separated by the planes made up of the two pairs of baffles. This is illustrated as the blue dotted cross in Figure 6.3 a).

Combining the division from Step 2 and Step 4 the full compartmentalization is complete and the compartment structure can be visualized as seen in Figure 6.6

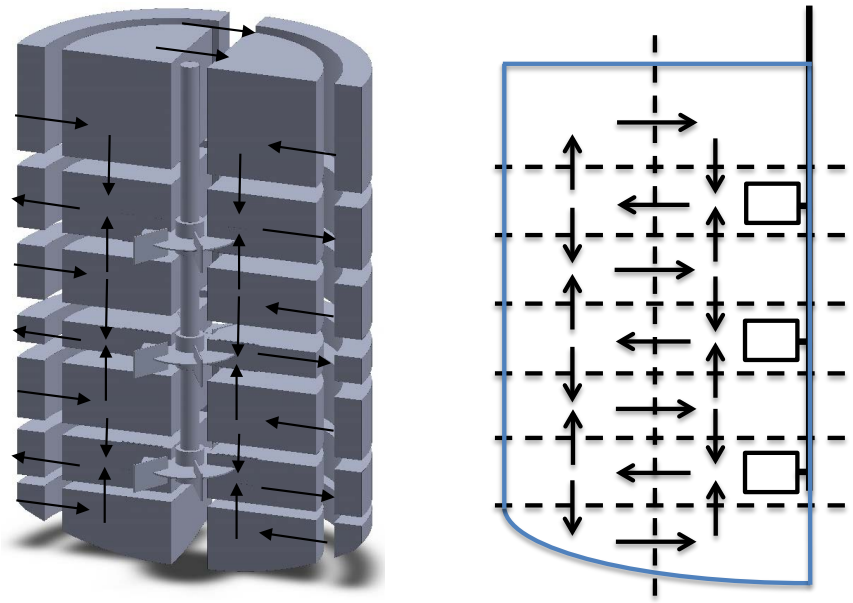

a) b)

Figure 6.6 - a) Hypothesis driven compartment model structure. The vessel is divided into 7 horizontal and 2 vertical zones as well as 4 "wedges" produced by the baffles. The resulting model has 56 compartments. b) 2D representation of flows in 14 compartments in one "wedge". The figure is not to scale.

The structure shown in Figure 6.6 is intuitive and similar to previous reported compartment structures for reactors containing multiple RDT's [16]. Contrary to previous attempts, this model structure is deducted from numerical simulations of the hydrodynamics and the position of each compartment is chosen in order to make sure that the flow is indeed uniform at the interface. A detailed definition of each flow and compartment in the model is described in the supplementary material of this manuscript.

6.4.3.6 Step 5 – flow quantification

The fifth and final step of the methodology consists of determining the liquid flow between each of the identified compartments resulting from Step 1 to 4. The unidirectional flow on every surface in every compartment is determined as the area integral of the velocity perpendicular to the surface.

$$F = \int \int v_p \, dx_1 \, dx_2 \cdot \rho \qquad (6.1)$$

Where F is a unidirectional mass flow, v_p is the velocity perpendicular to the given surface, x_1 and x_2 are the dimensions suspending the surface and ρ is the liquid density. The integration is carried out in ANSYS CFD-POST, where each interface is defined in the reactor. The data is exported as .csv files to be used in MATLAB for further analysis.

The described methodology is in this work applied to a single-phase stirred tank equipped with Rushton turbines, but it is equally applicable to any geometry and also for multiphase systems. The circumferential division of the vessel is carried out assuming rotational symmetry in the investigated case. Other geometries might require an investigation of the uniformity of the fluid flow in the circumferential direction, which should be done along the lines used in Step 1 and 3.

6.5 Results

The experimentally determined tracer profiles are in this section compared with the three model methods described in this work. The ability to predict mixing time has previously been used as a measure to benchmark hydrodynamic models, being it network-of-zones, CFD or tanks in series models [8]. However, if the aim of the models is to ultimately describe process kinetics, such as substrate addition or species mixing, a more rigorous measure should be adopted. In this work the models have been benchmarked by comparing the predicted and measured pH tracer profile from the time of injection to homogeneous mixing. This is a demanding measure for such models, and maximizes the utilization of the collected data.

6.5.1 4+1 compartment model

The interchange flows between the four main compartments were estimated through an optimization algorithm based on the tracer response for all agitation speeds and pulse positions. The experimental setup contained five pH sensors, but the model only contains four bulk compartments, which meant that the two top sensors (one and two) are combined in the top compartment. This is described in Table A2 in the supplementary materials. The resulting model outputs are summarized in Figure 6.7.

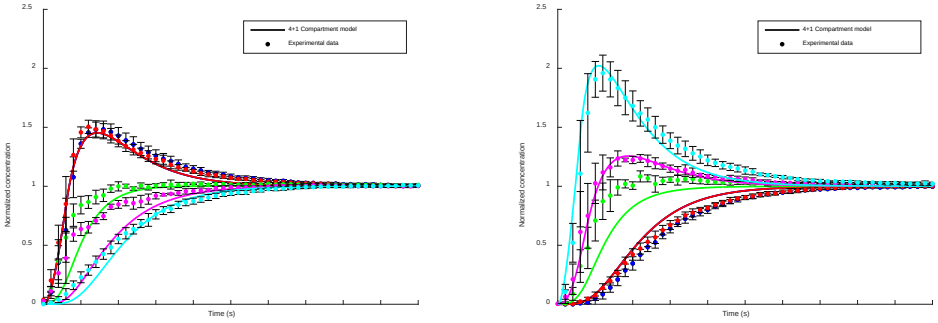

Figure 6.7 - Experimental and simulated tracer response curve for medium agitation using top (a) and bottom dosing (b). Solid lines indicate the model simulations and points depict experimental data. ● Sensor 1, ● sensor 2, ● sensor 3, ● sensor 4 and ● sensor 5. The experimental data for the sensors is shown an average with error bars corresponding to one standard deviation.

Figure 6.7 a) shows that the 4+1 compartment model generally has the ability to recreate the tracer profiles of the sensors in the reactor following a three second tracer dose. The fact that the fitted model corresponds well to the experimental data confirms the hypothesis of compartmentalization in reactors with multiple Rushton disc turbines.

6.5.2 Hypothesis driven compartment model

The hypothesis based compartment method resulted in 56 bulk compartments and a feed compartment, where interchange flows between compartments were calculated from CFD simulations. The predictive ability of the model is evaluated in Figure 6.8, where the tracer response from a top and bottom pulse is compared with simulations.

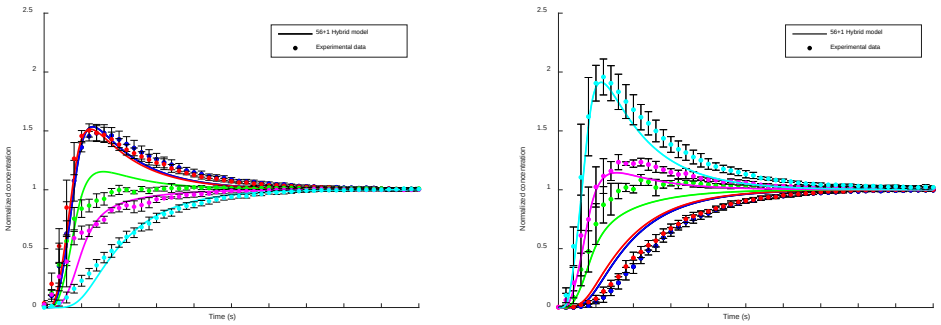

a) **b)**

Figure 6.8 - Measured and simulated tracer response from a top a) and bottom b) pulse. The hypothesis driven compartment model output is shown as a solid line and the data are shown as points. ● Sensor 1, ● sensor 2, ● sensor 3, ● sensor 4 and ● sensor 5. The experimental data for the sensors is shown an average with error bars corresponding to one standard deviation.

Following a top pulse, the tracer trajectory of the sensors one, two, four and five is well represented by the model as shown in Figure 6.8a). Comparing to the 4+1 compartment model, the response of sensor one and two are in the hypothesis driven approach two separate outputs. The overshoots of the bottom two sensors as a consequence of dosing a pulse in the bottom of the reactor, as depicted in Figure 6.8b), are described well by the model. Generally, the developed model describes the transient behavior of tracer addition in both top and bottom of the reactor very well for all five sensors, and the deviations apparent in Figure 6.8 are mainly small parallel shifts of the response profiles. This indicates that the developed model is able to recreate the major trends of the hydrodynamics occurring in the bioreactors.

6.5.3 CFD model

In order to benchmark the hypothesis driven methodology, the underlying CFD models ability to represent the dynamic tracer profile is evaluated against the measured values from a top and bottom pulse. The tracer profiles from the CFD simulations, shown in Figure 6.9, are evaluated in the node closest to the physical position of each sensor in the bioreactor.

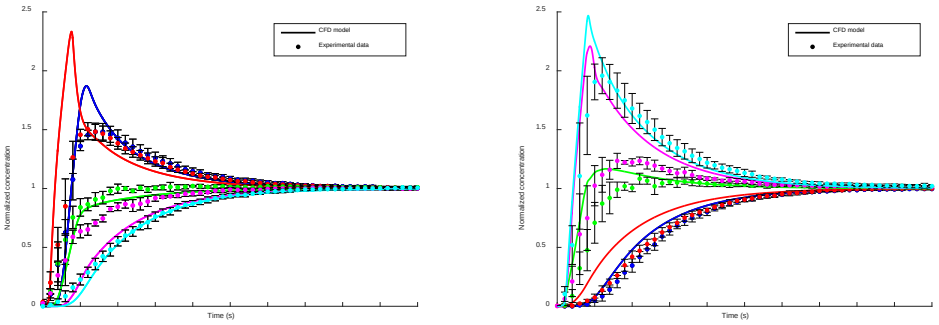

a) b)

Figure 6.9 - Measured and predicted values of tracer response following a three-second pulse in the top a) and bottom b) of the reactor. The simulations are shown as a solid line and points depict the measurements. ● Sensor 1, ● sensor 2, ● sensor 3, ● sensor 4 and ● sensor 5. The experimental data for the sensors is shown an average with error bars corresponding to one standard deviation.

The CFD simulations suggest a larger overshoot of the tracer concentration than observed experimentally for both top and bottom feeding as seen in Figure 6.9 a) and b). The tracer response of sensor three is well described by the CFD simulations in the case of top and bottom dosing. The overshoot witnessed in the sensor response close to the feeding point is more pronounced than for the other methods investigated above. This is most likely caused by the fact that the dosing of tracer is assumed to be a perfect pulse. The 4+1 compartment method and the hypothesis driven approach both include a dosing compartment, which can mitigate the imperfections of the experimental pulse dosing, which took 3 seconds in total.

6.5.4 Comparing the models

In order to compare the performance of the different modelling methods across the different conditions investigated the root mean square error (RMSE) between measurements and predictions were calculated for all conditions.

$$RMSE = \sqrt{\left(C_{i,j,k}^{exp}(t) - C_{i,j,k}^{sim}(t)\right)^2} \quad (6.2)$$

where $C_{i,j,k}(t)$ is the simulated or experimental concentration of tracer measured in compartment i, j, k at time t. This measure was scaled by the summated error from the 4+1 compartment model at medium agitation intensity. Furthermore, the RMSE for each condition is scaled by the associated mixing time to avoid bias of faster mixing conditions. A summary of this analysis is shown in Table 6.1.

Table 6.1 - Comparison of compartment model performance based on summed RMSE of each model at different agitation intensities. The summed RMSE values are scaled based on the error of medium agitation of the 4+1 compartment model.

	Low agitation	Medium agitation	High agitation
4+1 Compartments	1.37	1.00	0.78
56+1 Hypothesis driven	1.54	1.10	0.95
CFD	3.96	2.96	1.91

Table 6.1 reveals that the data driven 4+1 compartment model predicts the tracer profiles of the pH sensors more accurately than the hypothesis driven model and the CFD simulations for all investigated conditions. The models are generally more accurate with increasing agitation intensity, which is likely caused by a movement towards ideal mixing with increasing agitation intensity. The fact that the simple data driven 4+1 compartment model outperforms the other model strategies is not surprising given the fact that the data available is optimal for such model development. Due to the large data pool, the interchange flows between the four bulk compartments can be estimated with minimal correlation, which improves the predictive capabilities. Most bioreactors described in the literature contain only one or two sensors, and thus the collected data would not be sufficient to identify each flow individually, and as a consequence the predictive ability of the model would decrease.

The hypothesis driven compartment model is 10-12 % worse than the 4+1 compartment model for the investigated conditions, which is impressive given the fact that all the interchange flows between the 56 compartments were predicted. The hypothesis driven methodology performs on par with the data driven 4+1 compartment in the case study investigated in this work, but if the data available would be

less the data driven model would perform worse. The hypothesis driven method is on the contrary less dependent on data and it can be assumed that the accuracy showcased here should be expected in other case studies.

It is apparent from Table 1 that the CFD simulation is association with a lower accuracy than the other two models shown in this work. This can seems surprising since the hypothesis driven model is based upon the results from the CFD simulations. The majority of the error associated with the CFD simulations is however observed in the beginning of the tracer profiles and originates from the sensor that is placed closest to the feeding locations. This can be explained by the sensitivity of the tracer dispersion, and the fact that the compartment models both have a dosing compartment to avoid these overestimations.

A comparison of the tracer profiles of each of the models and the associated experimental data is shown in Figure 6.10.

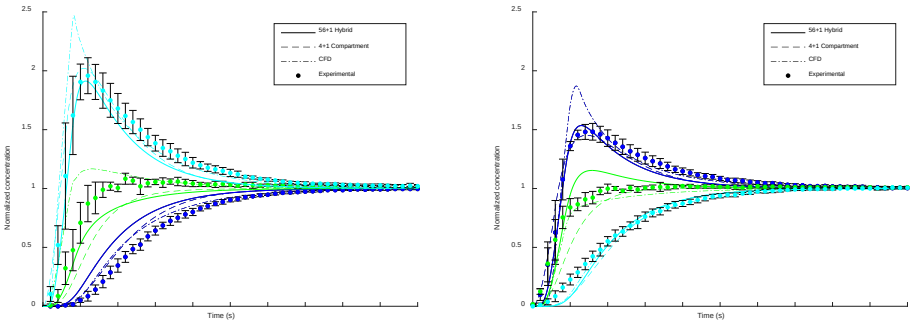

Figure 6.10 - Experimental data, shown as dots, for ● Sensor 1, ● sensor 3 and ● sensor 5 is compared with the hypothesis driven model (—), the 4+1 compartment model (— —) and the CFD model (— · —) following a pulse in the bottom a) and top b) of the reactor. The experimental data for the sensors is shown an average with error bars corresponding to one standard deviation.

The performance of the different models to recreate the tracer response is summarized in Figure 6.10, and it is apparent that the model performance in terms of tracking the tracer trajectory is rather similar, with model predictions that are close to the experimental values. As mentioned above, the CFD simulations suggest a slightly more pronounced peak in the bottom sensors overshoot, whereas the compartment models provide predictions which are closer to the experimental value. The accuracy of the CFD simulations is similar to previous findings in smaller systems, where CFD was used to predict

the tracer response [17]. The model predictions of the trajectory of sensor three in Figure 10 deviates between the different model approaches tested, where the CFD simulations predict a faster increase in concentration than the experimental values, and the compartment model predicts a slower approach towards reaching the homogeneous concentration. For all investigated conditions the sensor in the middle of the tank, sensor three, has been the most difficult to represent correctly in the model. This could be explained by the sensors position, which is in between the middle and top impeller, which also places it right between two recirculation loops, and hence small changes to the position of the loop will greatly affect the sensor response. The accuracy of the model prediction is also affected by the fact that each pH sensor is not located in the centre of each compartment, this affects how well each sensor represents the average concentration in its corresponding compartment. In order to fully confirm this more experimental work would be required, in which the sensor could be moved slightly up or down.

The dosing compartment introduced in the compartment models developed in this work is a necessary tool required to characterize the feeding of tracer, since the experimental dosing is not ideal. The measured signal by the five pH sensors is highly dependent on the exact feeding characteristic developed by the dosing pump and tubing, and since the model is required to recreate this pH signal in great detail the dosing compartment is relevant. Depending on the feeding system, the interchange flow between the dosing compartment and the compartment model will change, and this variable is therefore specific for the setup used, and requires tuning.

Complex phenomena occurring in a stirred bioreactor, which is not feasible or reasonable with CFD simulations, can be investigated using the developed compartmentalization method. This has been showcased before with regards microbial population heterogeneity using population balance models [18,19]. A simplified compartment model that represents the hydrodynamics of the bioreactor can furthermore be used to study multidimensional populations balance models, which currently is not reasonable in combination with common CFD tools [20]. A particular interesting topic is the developing field of mechanistic fermentation models for monitoring and control of bioprocesses [21]. Correct representation of the hydrodynamics in the fermenter could eliminate the extended use of process time delays used in advanced controllers. In particular, if the manipulated variable is substrate or nutrient feeding the application of an advanced hydrodynamic model appears attractive.

Constructing compartment models based on a hypothesis of the hydrodynamics in the process does not only apply for bioreactors. Processes that rely on complex phenomena and dynamics occurring at a large scale could also be subject to the methodology described in this work.

6.5.5 Experimental recommendations

Placement of sensors in a mixing experiment is a balance between systematically positioning sensors with equal distance to avoid any bias on sensor placement on one hand, and placing sensors in critical positions where a bulk mixing zone is expected and thus avoiding incorrect assumptions when comparing sensors and compartments in the mathematical models on the other hand. In the experimental data used in this work, sensors were positioned systematically and sensors and tracer dosing points were placed on the same mounting bracket since this was a practical solution. The tracer dosing is highly dependent on location in the vessel, which is also the reason why a feeding compartment is used to simulate the addition of tracer to the bulk liquid. In future work, tracer addition will be designed to mimic the substrate addition point in the vessel, to make sure that any assumptions used for tracer feed addition will also apply to substrate addition to get a better agreement between the pure mixing model and the complete reactor model.

6.6 Conclusion

Pilot scale mixing data was benchmarked against a RANS CFD model and a data driven four compartment model, representing a highly theoretic and empirical modelling approach respectively. Both models were able to describe the mixing data satisfactory but the models rely on either large amounts of computational effort or experimental data to be executed. Based on the CFD model, a novel methodology for developing compartment models that describe the hydrodynamics in a pilot scale bioreactor has been proposed and evaluated. The methodology relies upon conventional CFD methods to determine the radial and axial placement of each compartment by evaluating the directional change in axial and radial flow in the bioreactor.

The hypothesis driven methodology has proven to be within 15 % of the performance of a purely data driven four-compartment approach for the bioreactor equipped with three Rushton turbines and five pH sensors.

The hypothesis driven model increases the number of compartments compared to the data driven model, which enables the model to simulate three dimensional hydrodynamic flow, while still limiting the computational requirements to include simulation of reaction- and mass transfer kinetics. The model only uses one empirically fitted parameter, which limits the required experimental data significantly.

The methodology developed in this work is applicable to other bioreactor geometries, but also to other processes such as crystallization, wastewater treatment or combustion. The simplified hydrodynamic

model has the potential to serve as a platform for implementation of complex phenomena, which would not be computationally feasible in standard CFD software.

6.7 Acknowledgements

The authors would like to acknowledge Nanna Petersen Rønnest and Martin Peter Breil who have contributed directly to the project.

This project has received funding from Novo Nordisk A/S, the Technical University of Denmark (DTU) and Innovation Fund Denmark in the frame of the Strategic Research Center BIOPRO2 (BIObased PROduction: TOwards the next generation of optimized and sustainable processes).

6.8 References

[1] A.W. Nienow, Hydrodynamics of Stirred Bioreactors, Appl. Mech. Rev. 51 (1998) 3. doi:10.1115/1.3098990.

[2] N.M. Oosterhuis, N.W. Kossen, Dissolved oxygen concentration profiles in a production-scale bioreactor., Biotechnol. Bioeng. 26 (1984) 546–550. doi:10.1002/bit.260260522.

[3] P. Vrábel, R.G.J.M. Van der Lans, F.N. Van der Schot, K.C. a M. Luyben, B. Xu, S.O. Enfors, CMA: Integration of fluid dynamics and microbial kinetics in modelling of large-scale fermentations, Chem. Eng. J. 84 (2001) 463–474. doi:10.1016/S1385-8947(00)00271-0.

[4] A. Zhang, V.L. Tsang, R. Korke-Kshirsagar, T. Ryll, Effects of pH probe lag on bioreactor mixing time estimation, Process Biochem. 49 (2014) 913–916. doi:10.1016/j.procbio.2014.03.005.

[5] P.A. Vanrolleghem, G. Sin, K. V. Gernaey, Transient response of aerobic and anoxic activated sludge activities to sudden substrate concentration changes, Biotechnol. Bioeng. 86 (2004) 277–290. doi:10.1002/bit.20032.

[6] M. Reuss, Oxygen Transfer and Mixing: Scale-Up Implications, Biotechnol. Set. (2001) 185–217. doi:10.1002/9783527620999.ch10b.

[7] R. Mann, R.A. Williams, T. Dyakowski, F.J. Dickin, R.B. Edwards, Development of mixing models using electrical resistance tomography, Chem. Eng. Sci. 52 (1997) 2073–2085. doi:10.1016/S0009-2509(97)00035-3.

[8] C. Bach, J. Yang, H. Larsson, S.M. Stocks, K. V Gernaey, M.O. Albaek, U. Krühne, Evaluation of mixing and mass transfer in a stirred pilot scale bioreactor utilizing CFD, Chem. Eng. Sci. 171 (2017) 19–26. doi:10.1016/j.ces.2017.05.001.

[9] P. Moilanen, M. Laakkonen, J. Aittamaa, Modelling fermenters with CFD, Comput. Aided Chem. Eng. 20 (2005) 709–714. doi:10.1016/S1570-7946(05)80240-8.

[10] F. Bezzo, S. Macchietto, C.C. Pantelides, General hybrid multizonal/CFD approach for bioreactor modeling, AIChE J. 49 (2003) 2133–2148. doi:10.1002/aic.690490821.

[11] A. Delafosse, M.L. Collignon, S. Calvo, F. Delvigne, M. Crine, P. Thonart, D. Toye, CFD-based compartment model for description of mixing in bioreactors, Chem. Eng. Sci. 106 (2014) 76–85. doi:10.1016/j.ces.2013.11.033.

[12] F. Bezzo, S. Macchietto, A general methodology for hybrid multizonal/CFD models: Part II. Automatic zoning, Comput. Chem. Eng. 28 (2004) 513–525. doi:10.1016/j.compchemeng.2003.08.010.

[13] B.R. Poulsen, J.J.L. Iversen, Mixing determinations in reactor vessels using linear buffers, Chem. Eng. Sci. 52 (1997) 979–984. doi:10.1016/S0009-2509(96)00466-6.

[14] R. Manfredini, V. Cavallera, L. Marini, G. Donati, Mixing and oxygen-transfer in conventional stirred fermenters, Biotechnol. Bioeng. 25 (1983) 3115–3131. doi:10.1002/bit.260251224.

[15] C. Haringa, A.T. Deshmukh, R.F. Mudde, H.J. Noorman, Euler-Lagrange analysis towards representative down-scaling of a 22 m^3 aerobic S. cerevisiae fermentation, Chem. Eng. Sci. (2017). doi:10.1016/j.ces.2017.01.014.

[16] P. Vrábel, R.G.J.M. Van Der Lans, K.C.A.M. Luyben, L. Boon, A.W. Nienow, Mixing in large-scale vessels stirred with multiple radial or radial and axial up-pumping impellers: Modelling and measurements, Chem. Eng. Sci. 55 (2000) 5881–5896. doi:10.1016/S0009-2509(00)00175-5.

[17] A. Delafosse, M.L. Collignon, S. Calvo, F. Delvigne, M. Crine, P. Thonart, D. Toye, CFD-based compartment model for description of mixing in bioreactors, Chem. Eng. Sci. 106 (2014) 76–85. doi:10.1016/j.ces.2013.11.033.

[18] J. Morchain, J.C. Gabelle, A. Cockx, Coupling of biokinetic and population balance models to account for biological heterogeneity in bioreactors, AIChE J. 59 (2013) 369–379. doi:10.1002/aic.13820.

[19] J. Morchain, J.C. Gabelle, A. Cockx, A coupled population balance model and CFD approach for the simulation of mixing issues in lab-scale and industrial bioreactors, AIChE J. 60 (2014) 27–40. doi:10.1002/aic.14238.

[20] R.L. Fernandes, M. Carlquist, L. Lundin, A.-L. Heins, A. Dutta, S.J. Sørensen, A.D. Jensen, I. Nopens, A.E. Lantz, K. V. Gernaey, Cell mass and cell cycle dynamics of an asynchronous budding yeast population: Experimental observations, flow cytometry data analysis, and multi-scale modeling, Biotechnol. Bioeng. 110 (2013) 812–826. doi:10.1002/bit.24749.

[21] L. Mears, S.M. Stocks, M.O. Albaek, G. Sin, K. V. Gernaey, Mechanistic Fermentation Models for Process Design, Monitoring, and Control, Trends Biotechnol. 35 (2017) 914–924. doi:10.1016/J.TIBTECH.2017.07.002.

Chapter 7

Conclusions and future perspectives

Following each chapter in this thesis, the main conclusions have been presented in the context of that chapter. In this chapter, the conclusions are presented in a broader perspective together with suggestions for future work.

7.1 Modelling

Hydrodynamics play a key role in fermentation process performance, and understanding of the relationship between hydrodynamics and microbial kinetics is essential in order to avoid unwanted process heterogeneities. In terms of understanding and visualizing the hydrodynamics inside aerated fermentation processes, this thesis has shown that CFD is a valuable tool. The predicted hydrodynamics and mass transfer characteristics have been evaluated for an aerobic *Trichoderma reesei* fermentation process at pilot and full scale. The mass transfer predictions of the commercial CFD software combined with literature correlations have proven accurate and are comparable to data driven empirical correlations. The combination of CFD and microbial kinetics has massive potential in both optimization of current processes and introduction of new processes with challenging traits.

The oxygen concentration prediction in this work is based upon a measurement of the oxygen uptake rate from the industrial scale fermentation. In order to avoid this dependency on measurements or assumptions of microbial uptake, models of microbial kinetics have to be developed. The improved modelling capabilities using various versions of CFD simulations demand greater insight into the microbial physiology and an improved understanding of how the microorganism adapts to changing environments. Some progress has been made for certain microorganisms [1,2], but in order to capitalize fully on the improved computational efforts more work should be carried out. The derived CFD models and correlations can be used as a basis to also implement biological models to assess substrate dispersion and uptake rates. Emphasis should however be put on using e.g. regime analysis as a simplification tool to maintain only the necessary complexity of the microbial growth kinetics in

the models, because the computational cost of introducing additional complexity in a full- scale simulation is proportional to the number of nodes in the simulation.

A hypothesis driven compartmentalisation method has been developed and applied to a pilot scale bioreactor with satisfactory results. This case study illustrates that in order to leverage the time and computational effort associated with simulations of production scale fermentation processes modelling scale-down should be considered. The understanding achieved from the detailed numerical simulations can be condensed to a reduced number of compartments with unidirectional flow that can serve as a simulation platform for process development. The reduced number of compartments enables the incorporation of other models against a reasonable computational cost. For example, a compartment model can be combined with an incorporation of a population balance models that can account for the population heterogeneity in the fermenter [3], or advanced process control strategies could be incorporated that could improve substrate feed addition [4]. Additionally, the simplification of the hydrodynamic model enables more users to apply the model: users without knowledge of CFD, but only basic MATLAB programming knowledge, can easily apply the compartment model, thereby increasing the impact of the CFD simulations significantly.

7.2 Measurements

Validation of the numerical methods remains a challenge because spatially resolved measurements of process variables are challenging and often unfeasible in industrial systems, such as a *Trichoderma reesei* fermentation. The application of multiple independent measurements such as, oxygen transfer rate, gas hold-up, gassed power draw and carbon evolution rate could, if available simultaneously, serve as an indirect validation of the simulations. These measurements are averaged over the volume of the fermenter and do not serve as true spatially resolved measurements of the system, which could be a problem at large scale.

Technology exists that is able to capture the distribution of bubble size during an industrial fermentation as highlighted in this thesis. The presented technology can assist in acquiring increased process understanding and display fundamental relationships between process conditions and gas-liquid interactions. Additionally, the sensor can also serve as an advanced tool in process monitoring to enable on-line assessment of the gas-liquid mass transfer. The fundamental understanding of the relationship between the bubble size distribution and process conditions can assist in developing models for CFD simulations of aerobic fermentation processes, which rely greatly on assumptions regarding the size of gas bubbles. Employing the developed technology on a routine basis in industrial

systems will inevitably give rise to additional applications of the developed optical measurement method.

The impact of this information should be assessed by simultaneously measuring the gas hold-up and thereby determining the fundamental correlations between mass transfer coefficient k_L, the interfacial area a and the process conditions such as power input, gas flow rate and viscosity. Furthermore, the knowledge of these phenomena and their dependency on process conditions could be compared with numerical predictions of the bubble break-up and coalescence in fermentation media.

Experimental data of process gradients from industrial scale are scarce in the open literature, because of the concern about protecting intellectual property of companies on the one hand, and technical difficulties associated with obtaining the measurements on the other hand. Experimental data, and in particular spatially resolved experimental data, do not alone improve the understanding of the origin of process gradients, but merely identify whether they occur. In order to capitalise on empirical spatially resolved information of process variables, advanced models have to accompany the measurements, and this combination can determine the origin of the process gradients. Advanced sensor technologies, such as free-floating particles, enabling direct measurements of the flow pattern in the fermenters could reduce the requirements of advanced modelling to accompany measurements. Naturally, the data obtained from the measurements would require some modelling to interpret and analyse the data, but probably not to the extent of requiring advanced CFD simulations. The industrial viability of these technologies is still unknown, but the research potential for such investigations is obvious.

7.3 References

[1] W. Tang, A.T. Deshmukh, C. Haringa, G. Wang, W. van Gulik, W. van Winden, M. Reuss, J.J. Heijnen, J. Xia, J. Chu, H.J. Noorman, A 9-pool metabolic structured kinetic model describing days to seconds dynamics of growth and product formation by Penicillium chrysogenum, Biotechnol. Bioeng. 114 (2017) 1733–1743. doi:10.1002/bit.26294.

[2] M. De Mey, H. Taymaz-Nikerel, G. Baart, H. Waegeman, J. Maertens, J.J. Heijnen, W.M. van Gulik, Catching prompt metabolite dynamics in Escherichia coli with the BioScope at oxygen rich conditions, Metab. Eng. 12 (2010) 477–487. doi:10.1016/j.ymben.2010.04.003.

[3] J. Morchain, J.C. Gabelle, A. Cockx, Coupling of biokinetic and population balance models to

account for biological heterogeneity in bioreactors, AIChE J. 59 (2013) 369–379. doi:10.1002/aic.13820.

[4] L. Mears, S.M. Stocks, G. Sin, K. V. Gernaey, A review of control strategies for manipulating the feed rate in fed-batch fermentation processes, J. Biotechnol. 245 (2017) 34–46. doi:10.1016/J.JBIOTEC.2017.01.008.

List of publications

Articles

C. Bach, J. Yang, H. Larsson, S.M. Stocks, K. V Gernaey, M.O. Albaek, U. Krühne, Evaluation of mixing and mass transfer in a stirred pilot scale bioreactor utilizing CFD, Chem. Eng. Sci. 171 (2017) 19–26. doi:10.1016/j.ces.2017.05.001.

Bach, C., Spann, R., Larsson, H. K., Pereira Rosinha Grundtvig, I., Albæk, M. O., Gernaey, K. V., & Krühne, U. Computational Fluid Dynamics - en genvej til procesindsigt. Dansk Kemi 97(10) (2017), 14–17

Conference abstracts

Bach C, Albæk MO, Krühne U, Gernaey KV. Large scale simulations of Trichoderma reesei fermentation using computational fluid dynamics: Approach and early successes. Recent Advances in Fermentation Technology 2017, Bonita springs, United States. 2017. Accepted for an oral presentation.

Bach C, Albæk MO, Krühne U, Gernaey KV, Ein-Mozaffari F. Flow characterization of aerated bubble column reactor using electrical resistance tomography and computational fluid dynamic methods. 10th World Congress of Chemical Engineering (WCCE10), Barcelona, Spain. 2017. Accepted for an oral presentation.

Bach C, Albæk MO, Krühne U, Gernaey KV. A novel in situ measurement method of bubble sizes in bioreactors using a high speed camera. International Symposium on Mixing in Industrial Processes IX, Birmingham, United Kingdom. 2017. Accepted for poster presentation.

Bach C, Albæk MO, Stocks SM, Krühne U, Gernaey KV. A CFD model for determining mixing and mass transfer in a high power agitated bioreactor. MIXING XXV Conference, Quebec City, Canada. 2016. Accepted for an oral presentation.

Bach C, Albæk MO, Krühne U, Gernaey KV. Hydrodynamic Characterization of Substrate Gradients in a Pilot Scale Fermenter Using CFD and Spatially Distributed Sensors. Recent Advances in Fermentation Technology 2015, Clearwater Beach, United States. 2015. Accepted for a poster presentation

Appendix A

Supporting information for Chapter 3

This appendix contains information about the boundary conditions applied in the model described in the manuscript. Furthermore, the mesh sensitivity of the model and the prediction of turbulent impeller power number are described.

Boundary conditions and solver settings

The walls in the model were modeled with a no slip condition for liquid and a free slip condition for gas in order to distinguish between the interactions of the different fluids with the walls in the geometry. The baffles in the fermenter were simulated as 0-thickness walls which follows the guidelines from Gunyol and Mudde (2009) [1]. A rotational periodicity was applied to the symmetry plane in the geometry allowing the simulation of only half of the reactor. The top of vessel was modelled as an opening allowing only the liquid to reenter the domain in order to represent the dynamic fluid behavior at the top of the liquid surface. The rotation of the impeller was captured in the model using a multiple reference frame interface as shown in Figure 1 and similar to other previous studies [2]. The air was introduced in the sparger as mass flow rate normal to the sparger surface. The sparger was supplied with a no slip condition for the continuous phase.

The solution was set up using a two stage scheme. Initially the solution was achieved using a first advection scheme followed by a high resolution scheme when the flow was fully developed. This decreased the computational time without losing the accuracy. The convergence was achieved using a time step of 0.001 s in order to avoid numerical instabilities.

Mesh sensitivity

In order to make sure that the simulations were independent on the mesh configuration a mesh sensitivity study was performed. A change less than 5 % in mixing time was used as the acceptable threshold for mesh independent results. Three different mesh densities were tested and the results are summarized in Table A.1

Table A.1 - Result of mesh sensitivity study covering a coarse, medium and fine mesh with varying element density.

Mesh	Element density [#/L]	t_{95} [s]	Difference [%]
Coarse	914.6	9.1	17
Medium	2017.3	8.15	4.5
Fine	6475.8	7.8	-

The simulations exhibit some mesh sensitivity in particular when the coarse mesh is compared with the fine mesh, which results in a 17 % difference in simulated mixing time. It is apparent from Table A.1 that the medium mesh density satisfies the threshold in the compromise between computational time and simulation accuracy.

Power number prediction

The power input is a key performance indicator of stirred vessels. This is apparent from the correlations of performance parameters such as mixing time, k_La and bubble size, which all are dependent on the power supplied to the vessel. Hence it is essential that the developed model is able to predict the power input to the fermenter for a range of conditions. The power input was computed from the simulation by evaluating the torque delivered by the impeller for relevant Reynolds numbers. The measured and predicted power number are both shown in Figure A.1.

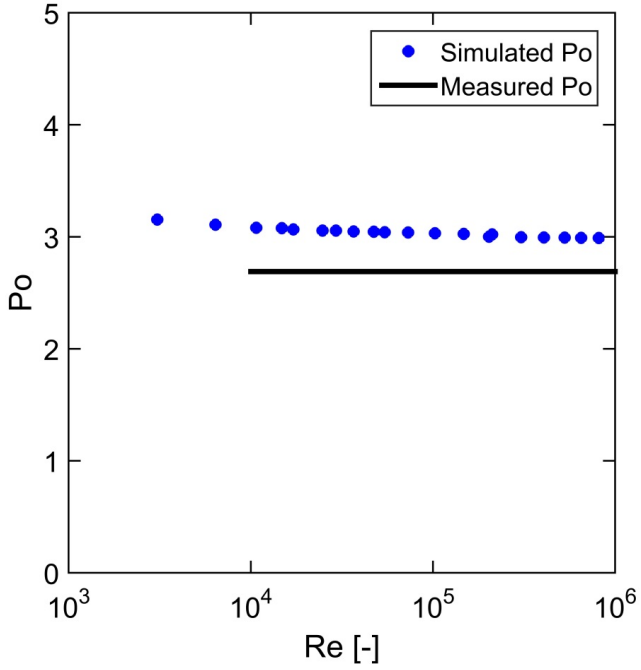

Figure A.1 - Comparison of measured and simulated power number in the turbulent regime. The measured power number is based on previously published results by [3]**.**

The deviation for the investigated conditions in the turbulent region is less than 12.5 %. This difference shows that the developed model can predict the power input to the vessel to an extent similar to other literature on power input to bioreactors [4].

Appendix B

Supporting information for Chapter 4

An important aspect of quantifying the size of detected objects from the captured images is a calibration method that can convert pixels into millimeters in a robust manner as well as validating that the method actually estimates the particle sizes of concern. A standard procedure of calibrating optical methods of size detection is using fixed size glass beads in a controlled environment [5]. The detection method employed in this work was calibrated using 1 mm glass bead from VWR. The calibration was carried out in a 250 mL stirred system operating at 1.9 kW/m^3. The agitation in the lab scale system induced some gas entrainment from the surface introducing a fraction of small objects in the calibration. The resulting size distribution is shown in Figure B.1

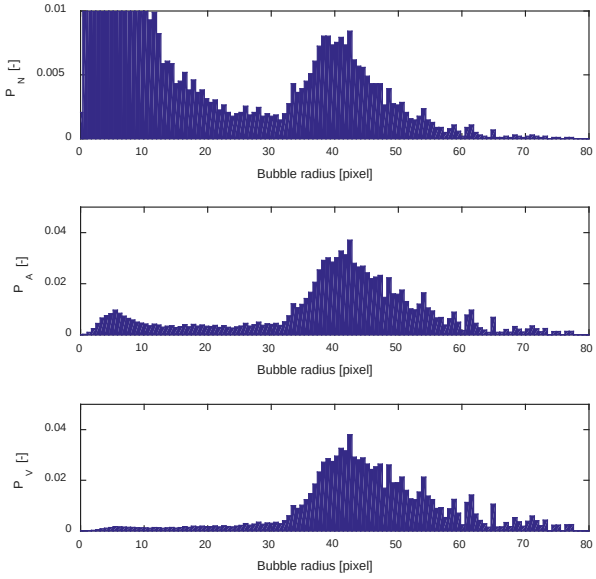

Figure B.1 – Probability density function of number, area and volume based distributions of 1 mm glass beads in a 250 mL stirred vessel.

The entrained gas bubbles from the reactor surface dominates the number based BSD as seen in Figure B.1 resulting in a large number of objects with sizes between 0 and 10 pixels. The peak of the glass

beads is detectable when looking closer into the number distribution and clearly visible in the area and volume based size distributions. The mode of the peak represents the average size of the detected glass beads, and the different modes are summarized in Table B.1.

Table B.1 – Model of peak in number, area and volume based BSDs of 1 mm glass beads used for calibration of detection method.

Distribution	Mode [pixel]
Number	40.7
Area	41.35
Volume	42.03

From Table B.1 it is apparent that even though the number, area and volume distributions are weighted differently the mode of the peak representing the glass beads is approximately 41 pixels corresponding to a particle with 1 mm in diameter. The instrumental broadening, i.e. the spread of the peak around 41 pixels, is largely because the detected bubbles will distribute about the focus plan of the optical recording system. This is of no major concern, as it is mainly interesting to observe how bubble size distributions compare for different process conditions that in estimating the exact numbers.

Appendix C

Supporting information for Chapter 5

The discretisation of the fermenter volume used for the numerical simulations of the flow in Chapter 5 was done in ICEM CFD 16.0. The geometry was divided into a rotating domain including all the impellers and a stationary domain comprised on the baffles, cooling coils and vessel wall. The stationary domain was meshed as a hexahedral mesh, and the same mesh was used for all simulations. Case 1 and Case 2 was discretised as a hexahedral mesh, where as Case 3 because of the complex impeller geometry had to be meshed using an unstructured tetrahedral routine. The mesh statistics are summarized in Table C.1.

Table C.1 – Mesh density of the mesh used in the various cases investigated.

Case	Mesh density [#/m^3]
1	$85 \cdot 10^3$
2	$130 \cdot 10^3$
3	$129 \cdot 10^3$

The mesh densities shown in Table C.1 are comparable with other studies of industrial two-phase bioreactors. Haringa et al (2017) [6] simulated a 22 m^3 aerobic fermenter with a mesh density of $163 \cdot 10^3$ #/m^3 and Morchain et al (2014) [7] simulated a 70 m^3 aerobic fermenter with a mesh density of $142 \cdot 10^3$ #/m^3 similar to the cases studied in this work. The mesh density of Case 1 is lower than the other cases because of the simplicity of the four Rushton turbines investigated in that scenario.

Appendix D

Supporting information for Chapter 6

4 + 1 Compartment model

The compartment model is based on the assumption that the radial flow from each of the 3 RDTs divides the bulk liquid in the bioreactor into 4 compartments. Each compartment is assumed ideally mixed and is geometrically defined by the vessel dimensions as well as the position of the impellers. Neighboring compartments are connected by exchange flows (EF_i), representing the liquid flow between the compartments. Each of the exchange flows are bidirectional. In addition to the 4 main compartments making up the bulk liquid in the vessel, a feed compartment is added to the model. The feed compartment is an attempt to simulate the initial mixing of liquid added to the vessel, accelerating the added plume of liquid into the bulk flow in the reactor. The feed compartment connected to the compartment where the tracer is added (compartment 1 for simulating top dosing and compartment 4 for bottom dosing) with an exchange flow denominated feed flow (EF_f). In or der to limit the number of parameters in the model, one value of the feed flow parameter is shared for simulating both top and bottom dosing.

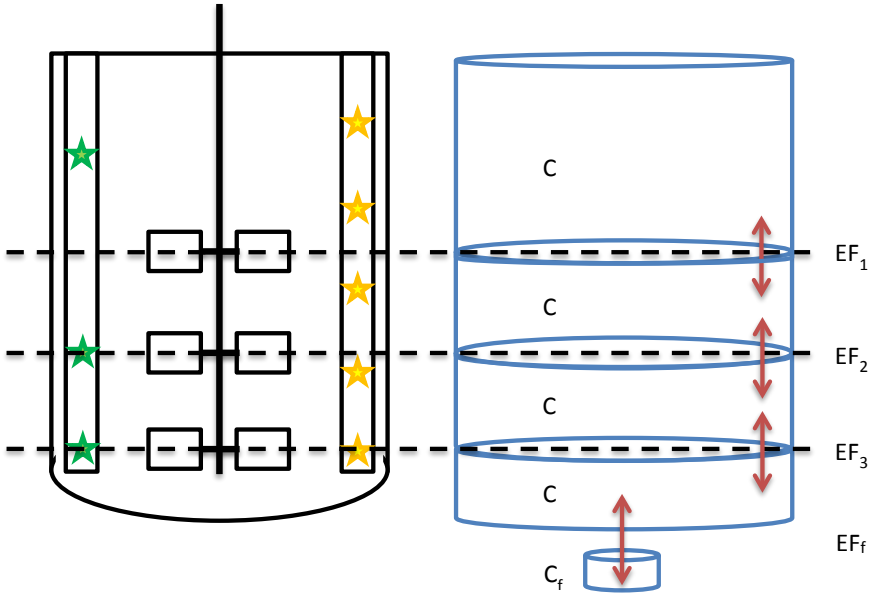

Figure D.1 – Diagram of bioreactor and associated compartment model. The dotted line represents the impeller zone division by Rushton disc turbines producing radial flow. Red arrows represent

exchange flows between compartments. Yellow stars represent pH sensors and green stars represent dosing points. Compartments are numbered (Ci) where i denominate compartment number or feed compartment with associated exchange flows (EFi).

The complete list of parameters is shown in Table C.1. In the model the three exchange flows and one feed flow is determined empirically with the matlab function fmincon (matlab 2015b). Compartment volumes are calculated from vessel geometry.

Table D.1 - Model parameters of the 4+1 compartment model

Parameter name	Description	Unit	Calculation method	Number of parameter values in model
$\boldsymbol{EF_i}$	Exchange flow between compartments i and i + 1.	[m^3/s]	Empirically fitted to experimental data	4
$\boldsymbol{V_i}$	Volume of compartment i	[m^3]	Vessel geometry	4
$\boldsymbol{V_f}$	Volume of feed compartment	[m^3]	Small pseudo value	1
$\boldsymbol{C_i}$	Normalized tracer concentration in compartment i	[U/m^3]	Simulated value	4
$\boldsymbol{C_f}$	Normalized tracer concentration in feed compartment	[U/m^3]	Simulated value	1

When comparing model simulations to experimental data, each sensor reading in the dataset are compared to the compartment corresponding to the physical location of the sensor. This is described in Table D2. Since the sensors are arranged systematically with even spacing in the vessel. The sensors are not all positioned in the center of their corresponding compartment which is indicated in Figure D.1. This is a cause of error in the model since the sensors are assumed to represents the average pH in their corresponding compartment.

Table D.2 - Sensor compartment coupling

Sensor #	Compartment #
1	1
2	1
3	2
4	3
5	4

Table D.3 shows the mass balances that make up the 4+1 compartment model with bottom dosing. The system of equations is solved with the ode15s solver (matlab 2015b). The model is solved in two parts with and without the addition of tracer to the feed compartment. The set of equations in Table D.3 represents the model after the simulated addition of tracer. The tracer is added to the mass balance for c_f as a linear flow over three seconds.

TableD.3 - 4+1 model mass balance equations

$\frac{dc_1}{dt} = (EF_1 \cdot c_1 - EF_1 \cdot c_2)/V_1$
$\frac{dc_2}{dt} = (EF_1 \cdot c_1 + EF_2 \cdot c_3 - EF_1 \cdot c_2 - EF_2 \cdot c_2)/V_2$
$\frac{dc_3}{dt} = (EF_2 \cdot c_2 + EF_3 \cdot c_4 - EF_2 \cdot c_3 - EF_3 \cdot c_3)/V_3$
$\frac{dc_4}{dt} = (EF_3 \cdot c_3 + FF_1 \cdot c_f - EF_3 \cdot c_4 - FF_1 \cdot c_4)/V_4$
$\frac{dc_f}{dt} = (FF_1 \cdot c_f - FF_1 \cdot c_4)/V_f$

Hypothesis driven compartment model

The hypothesis driven model consists of 56 main compartments representing the bulk liquid in the vessel, as well as one feed compartment representing the plume formed by liquid added to the vessel. The number of main compartments and geometric position of each compartment division is based on

the hypothesis driven model methodology as described in the materials and methods section. The model describes the liquid flow in the vessel in three dimensions.

As described in the hybrid model methodology, the model consists of two parts.

1) A systematic division of the bulk liquid into 56 individual compartments consisting of:
    a. 6 horizontal divisions creating 7 compartments in the height of the vessel
    b. 1 radial division creating an inner and an outer cylinder
    c. 4 circumferential divisions creating 4 wedges.
2) The unidirectional flow of liquid going to and from each compartment and its neighboring compartments.
    a. 14 circumferential flows ($FC_{i,j}$)
    b. 6 inner vertical and 6 outer vertical flows that are averaged to 6 vertical flows (FV_i)
    c. 7 Horizontal flows (FH_i) based on the vertical flows.
    d. 1 Feed flow from feed compartment.

Figure 6.2 a) displays a three dimensional rendering of the model compartmentalization. Figure D.2 displays a schematic illustration of the compartments and parameters in the hypothesis driven model.

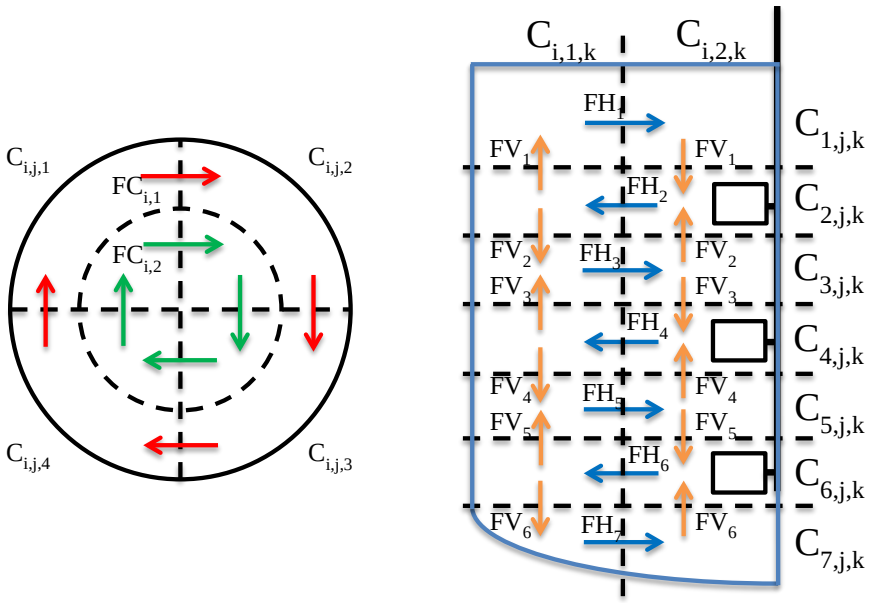

Figure D.2: a) Upside-down view of the four wedges in the model compartments are denominated ($C_{i,j,k}$) where i specify vertical position, j specify horizontal position and k specify wedge number. Red arrows indicate the outer circumferential flow ($FC_{i,1}$). Green arrows indicate inner circumferential flow ($FC_{i,2}$). Figure A2 b) cut-through view of one wedge in the model. Orange arrows indicate vertical flows calculated with the CFD software (FV_i). Blue arrows indicate horizontal flows (FH_i).

The CFD software is only able to calculate flow over flat compartment interphases. These include vertical and circumferential flows. The value of each vertical flow is calculated by the CFD software as inner and outer components. Since these values are almost identical, FV_j is treated as one average value for the inner and outer component of the vertical flow ($FV_i = (FV_{i,outer} + FV_{i,inner})/2$). This is done in order to avoid numerical errors in the model.

Since horizontal flows pass through a curved compartment interphase, these are not calculated directly by the CFD software. The horizontal flows are instead calculated manually, based on the flow assumptions show in Figure D.2 b). The horizontal flows are calculated as shown in Table D.4.

Table D.4 - Calculation of horizontal flows.

$FH_1 = FV_1$
$FH_2 = FV_1 + FV_2$
$FH_3 = FV_2 + FV_3$
$FH_4 = FV_3 + FV_4$
$FH_5 = FV_4 + FV_5$
$FH_6 = FV_5 + FV_6$
$FH_7 = FV_6$

In a similar fashion as used in the 4+1 compartment model. A feed compartment and corresponding feed flow are introduced to the model in order to simulate the delay between a tracer is added to the liquid and the tracer plume is accelerated into the bulk liquid flow in the vessel. The volume of the feed compartment is assumed small and the feed flow is empirically fitted to the experimental data using the function fmincon (matlab 2015b)

Sensor compartment coupling

As with the 4+1 compartment model, pH sensors are coupled to the compartment closest to its physical location in the vessel. Sensor data is compared to compartments as shown in Table D5. Tracer dosing is added to the wedge 90° downstream of the sensor location. In the experimental set up, sensors where located in the same wedge as the tracer addition, but this was altered in the model since it turned out that the a sensor located 180° downstream from the tracer addition point (data not included in this work) responded to a pulse addition before the sensor located in the same wedge as the tracer addition point. It was thus shown experimentally that a pulse mixes into the compartment downstream of the pulse addition point, instead of the immediate vicinity of the addition point. This is an important point in further experimental designs. Table D.6 shows the tracer addition compartments.

Table D.5 - Sensor/compartment coupling

Sensor #	Compartment #
1	$C_{1,1,1}$
2	$C_{2,1,1}$
3	$C_{3,1,1}$
4	$C_{5,1,1}$
5	$C_{6,1,1}$

Table D.6 - Dosing/compartment coupling

Dosing point	Compartment #
Top	$C_{1,1,2}$
Bot	$C_{6,1,2}$

Table D.7 displays the complete list of parameters in the hypothesis driven model. Only the feed flow in this model is empirically fitted to experimental data. The rest of the parameters are calculated with the CFD software and from vessel geometry.

Table D.7 - Total number of parameters in the hypothesis driven compartment model.

Parameter name	Description	Unit	Calculation method	Number of parameter values in model
H_i	Vertical division	[m]	Step 2 in methodology	6
R	Radial division	[m]	Step 4 in methodology	1
W_j	Circumferential division	[degree]	Geometrical assumption	4
FV_i	Vertical flow rate	[kg/s]	Step 5 in methodology	6
$FC_{i,j}$	Circumferential flow rate	[kg/s]	Step 5 in methodology	14
FH_i	Horizontal flow rate	[kg/s]	Calculated in table A4	7
$C_{i,j,k}$	Compartment tracer concentration	[kg/m^3]	Ode15s (matlab 2015b)	56
c_{feed}	Feed compartment concentration	[kg/m^3]	Ode15s (matlab 2015b)	1
$V_{i,j,k}$	Compartment volume	[m^3]		56

The final set of mass balance equations is solved in the same manner as the 4+1 compartment model using ode15s function (matlab 2015b).

References

[1] O. Gunyol, R.F. Mudde, Computational Study of Hydrodynamics of a Standard Stirred Tank Reactor and a Large-Scale Multi-Impeller Fermenter, Int. J. Multiscale Comput. Eng. 7 (2009) 559–576. doi:10.1615/IntJMultCompEng.v7.i6.60.

[2] M. Elqotbi, S.D. Vlaev, L. Montastruc, I. Nikov, CFD modelling of two-phase stirred bioreaction systems by segregated solution of the Euler-Euler model, Comput. Chem. Eng. 48 (2013) 113–120. doi:10.1016/j.compchemeng.2012.08.005.

[3] M.O. Albaek, K. V. Gernaey, S.M. Stocks, Gassed and ungassed power draw in a pilot scale 550 litre fermentor retrofitted with up-pumping hydrofoil B2 impellers in media of different

viscosity and with very high power draw, Chem. Eng. Sci. 63 (2008) 5813–5820. doi:10.1016/j.ces.2008.08.024.

[4] a. R. Khopkar, G.R. Kasat, a. B. Pandit, V. V. Ranade, CFD simulation of mixing in tall gas-liquid stirred vessel: Role of local flow patterns, Chem. Eng. Sci. 61 (2006) 2921–2929. doi:10.1016/j.ces.2005.09.023.

[5] B. Junker, W. Maciejak, B. Darnell, M. Lester, M. Pollack, Feasibility of an in situ measurement device for bubble size and distribution, Bioprocess Biosyst. Eng. 30 (2007) 313–326. doi:10.1007/s00449-007-0127-y.

[6] C. Haringa, A.T. Deshmukh, R.F. Mudde, H.J. Noorman, Euler-Lagrange analysis towards representative down-scaling of a 22 m3 aerobic S. cerevisiae fermentation, Chem. Eng. Sci. 170 (2017) 653–669. doi:10.1016/j.ces.2017.01.014.

[7] J. Morchain, J.C. Gabelle, A. Cockx, A coupled population balance model and CFD approach for the simulation of mixing issues in lab-scale and industrial bioreactors, AIChE J. 60 (2014) 27–40. doi:10.1002/aic.14238.

Process and Systems Engineering Centre (PROSYS)
Department of Chemical and Biochemical Engineering
Technical University of Denmark
Søltofts Plads, Building 229
DK - 2800 Kgs. Lyngby
Denmark

Phone: +45 45 25 28 00
Web: www.kt.dtu.dk/forskning/prosys